



ulm university universität  
**uulm**

# Electronic and Structural Properties of $\text{Li}_{(1-x)}\text{FePO}_4$ ( $X = 0, 0.5, 1$ )

Zur Erlangung des Doktorgrades Dr. rer. nat.  
der Fakultät für Naturwissenschaften  
der Universität Ulm

vorgelegt von

**Michael Kiarie Kinyanjui**

aus  
Karuri, Kenya

Ulm 2010

Amtierender Dekan: Prof. Dr. Axel Groß

1. Gutachterin: Prof. Dr. Ute Kaiser
2. Gutachter: Prof. Dr. Werner Tillmetz

Tag der Promotion: 30.5.2010

The work described in this thesis was performed at the Materials science group of Electron Microscopy, University of Ulm and Center for Solar Energy and Hydrogen Research, Ulm. It is part of the research program ReaLiBatt and was made possible by financial support from the (German Federal Ministry of Education and Research) (Bundes Ministerium für Forschung und Bildung, BMBF) and German Research Foundation ( Deutsche Forschungsgemeinschaft, DFG) and industrial partners

## Dedication

*This thesis is dedicated my parents who taught me to  
be ambitious and never to to give up.*





# Abstract

Lithium ion batteries are widely used for energy storage in many electronic devices. It is well known that the ability of a lithium ion battery to store energy is dependent on the properties of the materials which are used to construct the battery (see M. Winter and R.J. Brodd, Chem. Rev. 104, 4245 (2004)). These materials include those used as the anode, cathode, and electrolyte. Lithium iron phosphate ( $\text{LiFePO}_4$ ) is currently applied as a cathode material for lithium ion batteries. However, its electronic properties and the mechanism by which lithium ions are extracted (delithiation) or inserted (lithiation) into the lattice are still not completely understood. In this thesis the electronic and structural properties of  $\text{Li}_{(1-x)}\text{FePO}_4$  ( $\text{LiFePO}_4$   $x = 0$ ,  $\text{FePO}_4$   $x = 1$ ) have been investigated using valence and core loss electron energy loss spectroscopy (EELS) and high resolution transmission electron microscopy (HRTEM).

In the first part of this thesis we present the study of the electronic structure before and after delithiation,  $\text{LiFePO}_4$  and  $\text{FePO}_4$  respectively. This is accomplished using valence EELS (VEELS), core-loss EELS and bandstructure calculations. We show that the changes in the electronic structure between  $\text{FePO}_4$  and  $\text{LiFePO}_4$  are quite significant such that  $\text{FePO}_4$  can be considered to be a charge transfer insulator while the  $\text{LiFePO}_4$  can be considered to be a Mott-Hubbard insulator. In  $\text{LiFePO}_4$  the energy states at the top of the valence band and bottom of the conduction band are dominated by Fe 3d states. These states form the lower Hubbard band (LHB) and the upper Hubbard band (UHB) respectively. Delithiation is characterized by shifting of the iron (Fe) 3d bands to lower energies and increased hybridization between the Fe-3d and oxygen (O) 2p states. As a consequence, in  $\text{FePO}_4$  the valence states are now dominated by O-2p states and the UHB in the conduction band and the LHB in the valence band shifted to lower energies. These changes in the electronic structure are experimentally observed in the VEELS and core-loss EELS of  $\text{LiFePO}_4$  and  $\text{FePO}_4$ . The VEELS spectra of  $\text{FePO}_4$  are characterized by interband transitions found between 0-20 eV which is not observed in  $\text{LiFePO}_4$ . The observed VEELS spectra were fully analyzed using band structure calculations and calculated dielectric functions. It was in particular possible to assign the observed interband transitions as originating from bands situated just below the Fermi level which have mainly O-2p character. From core-loss EELS it is observed that the O-K edge in  $\text{FePO}_4$  shows a pre-edge peak that is

observed above the threshold of the main O-K edge. This pre-edge peak is not observed in the core EELS spectra of  $\text{LiFePO}_4$ . We show that the position of the pre-edge peak is determined by a charge transfer process which shifts the position of the Fe 3d bands with respect to the conduction band. We also show that the intensity of the pre-edge peak is related to the changes in Fe3d-O2p hybridization as a result of lithium ion extraction from the  $\text{LiFePO}_4$  lattice. The shifting of the Fe 3d states to lower energies with delithiation then is then observed in the shift of peak positions (chemical shift) at the  $\text{FeL}_{2,3}$  and P-K edges.

The second part of this thesis is concerned with structural studies on partially delithiated ( $\text{Li}_{(0.5)}\text{FePO}_4$ ). It is already known that the delithiation of  $\text{LiFePO}_4$  is a two phase process consisting of two end members  $\text{LiFePO}_4$  ( $x = 0$ ) and  $\text{FePO}_4$  ( $x = 1$ )(see Padhi *et al*, J. Electrochem. Soc. 144,1188(1997)). Consequently, the partial delithiated state  $\text{Li}_{(0.5)}\text{FePO}_4$  is an equal mixture of both  $\text{FePO}_4$  and  $\text{LiFePO}_4$  phases. As already mentioned the mechanism by which Li ions are extracted or inserted into the lattice is still not clear. Therefore one way to examine the delithiation mechanism is to examine phase distribution and phase interface in  $\text{Li}_{(0.5)}\text{FePO}_4$  grains. In thesis we do this by studying the distribution of delithiated and lithiated phases in  $\text{Li}_{(0.5)}\text{FePO}_4$  using HRTEM analysis. Delithiation of  $\text{LiFePO}_4$  is associated with a decrease in the unit cell volume of 7 % and reduction in the lattice parameters. For example with delithiation the lattice parameter  $b$  is reduced from (0.61 nm) in  $\text{LiFePO}_4$  to (0.57 nm) in  $\text{FePO}_4$ . Examining the lattice parameter distribution in partially delithiated  $\text{LiFePO}_4$  grains we find lattice parameters for  $\text{FePO}_4$  and  $\text{LiFePO}_4$  phases. This shows that at a partially delithiated state both phase do co-exist in the same grain. These results support the one dimensional model (1D) of delithiation which states that extraction of Li ions proceeds through the ion channels parallel to the [010] direction resulting in the formation of lithiated and delithiated domains in the same grain.

# Zusammenfassung

Lithiumionen-Batterien werden als Energiespeicher in vielen Elektrogeräten eingesetzt. Die Speicherfähigkeit der Lithiumionen-Batterien hängt von den Eigenschaften der verwendeten Materialien in der Batterie ab (siehe M. Winter and R.J. Brodd, Chem. Rev. 104, 4245 (2004)). Das betrifft sowohl die Anode, die Kathode als auch die Elektrolyte. Lithiumeisenphosphat ( $\text{LiFePO}_4$ ) dient oft als Material für Kathoden in Lithiumionen-Batterien. Trotzdem sind die elektronischen Eigenschaften und der genaue Mechanismus der Abgabe (Delithiation) und Aufnahme (Lithiation) von Lithiumionen im  $\text{LiFePO}_4$  Gitter noch nicht vollständig bekannt. In der vorliegenden Arbeit wurden die elektronischen und strukturellen Eigenschaften von  $\text{Li}_{(1-x)}\text{FePO}_4$  ( $x = 0, 0,5, 1$ ) mit Hilfe von Valenz- und Core Elektronen-Energie-Verlust-Spektroskopie (EELS) und hochauflösender Transmissions-Elektronenmikroskopie (HRTEM) untersucht.

Im ersten Teil der Arbeit haben wir die elektronische Struktur vor und nach der Delithiation von  $\text{LiFePO}_4$  und  $\text{FePO}_4$  untersucht. Dies wurde mit Hilfe von Valenz EELS (VEELS), Core-Verlust EELS und der Berechnung von Bandstrukturen bewerkstelligt. Die Veränderungen der elektronischen Struktur von  $\text{FePO}_4$  und  $\text{LiFePO}_4$  unterscheiden sich deutlich, so dass  $\text{FePO}_4$  als Ladungs-Transfer-Isolator und  $\text{LiFePO}_4$  als Mott-Hubbard-Isolator betrachtet werden kann. Die Energiezustände von  $\text{LiFePO}_4$  des Valenzbandes und des Leitungsbandes werden durch den Fe-3d Zustand dominiert. Diese Zustände bilden das untere Hubbard Band (LHB) und das obere Hubbard Band (UHB). Die Delithiation wird charakterisiert durch eine Verschiebung der Eisen (Fe) 3d Banden zu niedrigeren Energien und einem Anstieg der Hybridisierung zwischen dem Fe-3d Zustand und den Sauerstoff (O) 2p Zuständen. Dadurch wird der Valenzzustand bei  $\text{FePO}_4$  durch den O-2p Zustand dominiert und UHB in Leitungsband und LHB im Valenzband werden zu niedrigeren Energien verschoben. Diese Veränderungen der elektronischen Struktur spiegeln sich auch in den VEELS Beobachtungen und Core-Verlust EELS Spektren von  $\text{LiFePO}_4$  und  $\text{FePO}_4$  wieder. Die VEELS Spektren von  $\text{FePO}_4$  werden durch Interbandübergänge zwischen 0-20 eV charakterisiert und konnten bei  $\text{LiFePO}_4$  nicht gefunden werden. Die VEELS Spektren wurden vollständig durch die Berechnungen der Bandstruktur und der dielektrischen Funktionen analysiert. Es war teilweise möglich die Interbandübergänge den Bändern knapp unterhalb des Fermi-Niveaus (EF) zuzuordnen. Diese besitzen hauptsächlich O-

---

2p Charakter. In den Core-Verlust Spektren von  $\text{FePO}_4$  beobachtet man einen Peak vor der eigentlichen Schwelle der O-K-Kante (Pre-edge peak). Dieser pre-edge Peak wurde in den EELS Spektren von  $\text{FePO}_4$  beobachtet, nicht jedoch in den Spektren von  $\text{LiFePO}_4$ . Wir konnten zeigen, dass die Position des Pre-edge Peaks durch einen Ladungstransfer bestimmt wird, welcher die Fe-3d Bänder im Verhältnis zum Leitungsband verschiebt. Wir konnten zudem zeigen, dass die Intensität des Pre-edge Peaks in Beziehung mit den Veränderungen in der Fe3d-O2p Hybridisierung stehen, welche durch die Entfernung von Lithiumionen aus dem  $\text{LiFePO}_4$  Gitter verursacht werden. Die Verschiebung der Fe-3d Zustände durch Delithiation zu niedrigeren Energien konnte durch eine Verschiebung der Peakposition (chemische Verschiebung) an den  $\text{FeL}_{2,3}$  and P-K edges festgestellt werden.

Der zweite Teil dieser Arbeit beschäftigt sich mit strukturellen Untersuchungen bei partieller Delithiation von ( $\text{Li}_{0.5}\text{FePO}_4$ ). Im partiellen Delithiationsstatus ist  $\text{Li}_{0.5}\text{FePO}_4$  eine Mischung aus beiden Phasen (siehe Padhi *et al*, J. Electrochem. Soc. 144,1188(1997)). Dadurch ist der partieller Delithiationsstatus eine gleichmäßige Mischung aus der  $\text{FePO}_4$  und der  $\text{LiFePO}_4$  Phase. Wie bereits erwähnt ist der genaue Mechanismus des Ein- und Ausbaus der Lithiumionen in das Gitter noch nicht geklärt. Eine Möglichkeit den Delithiationsmechanismus zu untersuchen ist eine Überprüfung der Phasenverteilung und der Phasengrenzfläche in  $\text{Li}_{0.5}\text{FePO}_4$  Partikeln. In der vorliegenden Arbeit wurde das durch die Untersuchung der Verteilung von Delithiations- und Lithiationsphasen in  $\text{Li}_{0.5}\text{FePO}_4$  mittels HRTEM bewerkstelligt. Die Delithiation ist mit Reduktion der Gitterparameter verbunden. Ein Beispiel dafür ist die Reduktion der Gitterparameter von (0.61 nm) bei  $\text{LiFePO}_4$  auf (0.57 nm) bei  $\text{FePO}_4$  durch Delithiation. Die Untersuchung der Gitterparameter-Verteilung bei partieller Delithiation von  $\text{LiFePO}_4$  Partikeln ergab Gitterparameter sowohl für  $\text{FePO}_4$  als auch  $\text{LiFePO}_4$  Phasen. Es konnte gezeigt werden, dass in  $\text{Li}_{0.5}\text{FePO}_4$  Partikeln die  $\text{LiFePO}_4$  und  $\text{FePO}_4$  Phasen koexistieren. Diese Ergebnisse unterstützen ein eindimensionales Modell (1D) der Delithiation, welches die Extraktion von Lithiumionen durch Ionenkanäle parallel zur [010] Richtung erklärt. Dies führt zu einer Ausbildung von Lithiations- und Delithiationsdomänen im selben Partikel.

# Contents

Dedication	iii
Abstract	v
Zusammenfassung	vii
List of abbreviations	xxiii
List of notations	xxiii
Part I Introduction	1
1 Introduction	3
2 Structural, electronic and electrochemical properties of $\text{Li}_{(1-x)}\text{FePO}_4$	7
2.1 Structure and bonding . . . . .	7
2.2 $\text{LiFePO}_4$ in Li ion batteries . . . . .	12
2.2.1 Electrochemical properties . . . . .	12
2.2.2 The delithiation process in $\text{LiFePO}_4$ . . . . .	13
2.2.3 Electronic and structural properties of $\text{Li}_{(1-x)}\text{FePO}_4$ . . . . .	16
2.3 Thesis objectives . . . . .	17
Part II Experimental and Theoretical Background	19
3 Experimental Methods	21
3.1 Introduction to TEM . . . . .	21
3.1.1 Instrumentation . . . . .	22
3.2 Electron Energy Loss Spectroscopy . . . . .	23
3.2.1 EELS instrumentation . . . . .	23
3.2.2 Inelastic electron scattering . . . . .	23
3.2.3 Dielectric formalism of EELS . . . . .	26
3.3 Characteristics of EELS spectra . . . . .	28
3.3.1 Spectra acquisition and analysis . . . . .	31

---

3.3.2	Spectrum analysis . . . . .	31
3.4	High resolution electron microscopy . . . . .	35
3.4.1	Image formation in HRTEM . . . . .	35
3.4.2	Interaction with the crystal potential . . . . .	37
3.4.3	Interaction with the microscope - Transfer function . . . . .	37
3.4.4	Geometrical phase analysis of HRTEM images . . . . .	38
3.5	X-Ray diffraction methods . . . . .	40
3.6	TEM sample preparation . . . . .	42
<b>4</b>	<b>Theoretical methods</b>	<b>45</b>
4.1	Calculating EELS Spectra . . . . .	45
4.1.1	Density Functional Theory Methods . . . . .	46
4.1.2	Ligand Field Multiplet Method . . . . .	54
4.1.3	Spectroscopic notations . . . . .	56
4.2	Convergence tests . . . . .	56
<b>Part III</b>	<b>Results and Discussion</b>	<b>59</b>
<b>5</b>	<b>Beam effects on LiFePO<sub>4</sub> spectra</b>	<b>61</b>
5.1	Experimental Details . . . . .	61
5.2	Results . . . . .	62
5.2.1	Beam effects on Li-K edge . . . . .	62
5.2.2	Beam effects on O-K edge . . . . .	62
5.2.3	Beam effects on FeL <sub>2,3</sub> edge . . . . .	62
5.3	Discussion . . . . .	66
5.4	Conclusion . . . . .	67
<b>6</b>	<b>Valence-loss Spectra in Li<sub>(1-x)</sub>FePO<sub>4</sub></b>	<b>69</b>
6.1	Experimental and calculation details . . . . .	69
6.2	Results and Discussion . . . . .	70
6.2.1	Valence loss spectra . . . . .	70
6.2.2	Nature of the Observed peaks . . . . .	71
6.2.3	Character and the origin of the observed excitations . . . . .	81
6.2.4	Implications for the delithiation process . . . . .	88
<b>7</b>	<b>Core-loss Spectra in Li<sub>(1-x)</sub>FePO<sub>4</sub></b>	<b>91</b>
7.1	Introduction . . . . .	91
7.2	Experimental and calculation details . . . . .	92
7.3	Results and Discussion . . . . .	93
7.3.1	O-K edge . . . . .	93
7.3.2	FeL <sub>2,3</sub> edge . . . . .	98
7.3.3	Li-K edge . . . . .	106
7.3.4	P-K edge . . . . .	107

---

---

7.4	Conclusion . . . . .	109
<b>8</b>	<b>Structural properties in <math>\text{Li}_{(1-x)}\text{FePO}_4</math></b>	<b>111</b>
8.1	Experimental Details . . . . .	111
8.1.1	Electrochemical Measurements . . . . .	112
8.2	Results and Discussion . . . . .	112
8.2.1	Modelling the $\text{LiFePO}_4$ - $\text{FePO}_4$ interface . . . . .	116
8.2.2	Electron beam effects . . . . .	120
8.3	Conclusion . . . . .	121
<b>Part IV</b>	<b>Final Discussion and Future Outlook</b>	<b>123</b>
<b>9</b>	<b>Final Discussion</b>	<b>125</b>
9.1	Electronic properties of $\text{Li}_{1-x}\text{FePO}_4$ . . . . .	125
9.2	Delithiation mechanism in $\text{LiFePO}_4$ . . . . .	127
9.3	Electron beam effects . . . . .	128
9.4	Future Outlook . . . . .	128
9.4.1	Electron beam induced damages on $\text{LiFePO}_4$ . . . . .	128
9.4.2	Momentum dependent EELS . . . . .	128
<b>10</b>	<b>References</b>	<b>131</b>
	<b>Acknowledgments</b>	<b>143</b>
	<b>List of publications</b>	<b>145</b>
	Journal articles . . . . .	145
	Conference proceedings . . . . .	145
	<b>Curriculum vitae</b>	<b>147</b>





# List of Tables

3.1	Instrumental Parameters for XRD measurements . . . . .	42
6.1	Classification of the peaks observed in the experimental VEELS spectra for $\text{FePO}_4$ (Figure 6.4) . . . . .	81
6.2	Plasmon energies $\hbar\omega_f$ and $\hbar\omega_p$ for different $N_e$ values in $\text{LiFePO}_4$ . . . . .	87
7.1	Parameters used in the calculation of the $\text{FeL}_{2,3}$ edge for $\text{Fe}^{2+}$ and $\text{Fe}^{3+}$ . . . . .	103



# List of Figures

1.1	The discharge process in a Li battery where $\text{Li}^+$ are inserted into the cathode lattice . . . . .	4
2.1	The crystal structure of $\text{LiFePO}_4$ showing the $(\text{LiO}_6)^{11-}$ , $(\text{FeO}_6)^{10-}$ octahedral and $(\text{PO}_4)^{3-}$ tetrahedral units. . . . .	8
2.2	The shape of the 3d orbitals in an octahedral crystal field of ( octahedral symmetry- $\text{O}_h$ ). The two $e_g$ orbitals $d_{x^2-y^2}$ and $d_{z^2}$ point towards the $\text{O}^{2-}$ ions (ligands) while the $t_{2g}$ ( $d_{xy}$ , $d_{xz}$ , $d_{yz}$ ) 3d orbitals point between the ligands. The $t_{2g}$ and $e_g$ are separated by an energy $\Delta$ CF (or $10Dq$ ). The colour scheme shows the sign of the wavefunction where $+$ = red, and $-$ = blue. (After Gross, Ref [14]) . . . . .	9
2.3	Hybridization between the 3d orbitals of a transition metal ion with the P orbitals of the ligand. (a) The overlap and hybridization of the $d_{x^2-y^2}$ und $d_{z^2}$ ( $e_g$ )with the $p_x$ and $p_z$ orbitals of the ligand forming the $\sigma$ bond. (b) Overlap and hybridization of the $d_{xz}$ orbital with the ligand $p_z$ orbital. This forms the $\pi$ type of bond. The colour scheme shows the sign of the wavefunction where $+$ = red, and $-$ = blue. (After Gross, Ref [14]) . . . . .	10
2.4	Schematic density of states for (a) the Mott-Hubbard insulator and (b) the charge-transfer insulator. LHB and UHB indicate the lower Hubbard band and upper Hubbard band, respectively. $E_F$ represents the fermi level . . . . .	11
2.5	The charge-discharge curve for the delithiation of $\text{LiFePO}_4$ . . . . .	13
2.6	Phase diagram of $\text{Li}_{(1-x)}\text{FePO}_4$ . T, H and D represent the Triphylite ( $\text{LiFePO}_4$ ), Heterosite ( $\text{FePO}_4$ ) and disordered phases respectively. (After Dodd Ref [32]) . . . . .	14
2.7	A schematic showing the core-shell model of delithiation . . . . .	15
2.8	A schematic showing the one dimensional model of delithiation . . . . .	15
3.1	Schematic diagram of the EELS spectrometer and the ray diagram for the deflection of electrons in a spectrometer . . . . .	24

3.2	Scattering geometry of an electron energy loss experiment . A primary electron of energy $E_0$ and wave vector $k$ is inelastically scattered losing energy $\Delta E$ and undergoing a momentum transfer $q$ . The scattering angle is $\Theta$ . The convergence semi angle $\alpha$ determines the range of incident wave-vectors and the collection angle $\beta$ determines the range of the collected wavevectors . . . . .	24
3.3	A schematic showing the intraband transitions (blue arrow 1) and inter-band transition (blue-arrow 2) in a metal . . . . .	28
3.4	Energy and position drift of the Zero Loss Peak . . . . .	32
3.5	Schematic illustration of the HRTEM image formation process. The incident electron wave $\Psi_i(r)$ is dynamically scattered in the specimen. The exit-plane wave $\Psi_e(k)$ contains the structural information. The wavefunction at the image plane $\Psi_{image}(r)$ is modified by the instrument properties including the lens aberrations . . . . .	36
3.6	A schematic showing the steps in the geometrical phase analysis of a HRTEM image. . . . .	41
3.7	Bragg-Brentano geometry in the acquisition of X-Ray diffraction spectrum . . . . .	42
3.8	Preparation of single crystal $LiFePO_4$ samples (a) The thin strips of $LiFePO_4$ are mechanical grinded until they are $\approx 10-30\mu$ thin (b) The thin samples are then ion milled until a hole is formed in the centre of the samples. The regions near the hole are thin enough for TEM investigations . . . . .	43
4.1	The all-electron wavefunction and potential (red dotted lines) plotted against distance, $r$ , from the atomic nucleus. The corresponding pseudo wavefunction and potential is plotted (Blue dotted lines). Beyond a given radius $r_c$ the electron and pseudo-wavefunction and potential are the same. . . . .	50
4.2	Division of a unit cell into interstitial and atomic sphere regions in LAPW method . . . . .	51
4.3	Effect of the number of K points on total energy . . . . .	57
4.4	Effect of the plane wave cutoff on the calculated total energy . . . . .	58
5.1	Li-K (and Fe – $M_{2,3}$ ) (55-59 eV) and edge as a function of exposure time taken at (a) 80 kV (b) 300 kV . . . . .	63
5.2	Monitoring electron beam induced changes on the O-K edge for (a) $LiFePO_4$ and (b) $FePO_4$ . Beam induced damage is characterized by a rise of a pre-edge peak on the O-K edge of $LiFePO_4$ . . . . .	64
5.3	(a) Beam induced changes on the $FeL_{2,3}$ edges (b) Ratio of $FeL_3$ peaks plotted with the integrated intensity of the O-K pre-edge as a function of exposure time (in sec.) . . . . .	65

6.1	Valence loss spectrum for $\text{LiFePO}_4$ (black curve), and $\text{FePO}_4$ (red curve). . . . .	71
6.2	Number of electrons, $N_{\text{eff}}(E)$ , involved in inter-band transitions for $\text{LiFePO}_4$ . . . . .	72
6.3	Number of electrons, $N_{\text{eff}}(E)$ , involved in inter-band transitions for $\text{FePO}_4$ . . . . .	73
6.4	An interband transition from the valence band $ v_k\rangle$ to the conduction band $ c_k\rangle$ seperated by an energy $\hbar\omega$ . The interband contribution contribute to the total intensity of the $\epsilon_2$ . . . . .	74
6.5	The anisotropy of the calculated (a) ,(b) $\epsilon_1$ and (b),(c) $\epsilon_2$ for $\text{LiFePO}_4$ and $\text{FePO}_4$ respectively. The curves $\epsilon_{xx}$ , $\epsilon_{yy}$ , and $\epsilon_{zz}$ correspond to the crystallographic directions a,band b respectively . . . . .	75
6.6	Experimental $\text{Im}(1/(\epsilon))$ (black curve), $\epsilon_1$ (red curve), $\epsilon_2$ (blue curve) loss spectrum for $\text{LiFePO}_4$ . . . . .	76
6.7	Calculated $\text{Im}(1/(\epsilon))$ (black curve), $\epsilon_1$ (red curve), $\epsilon_2$ (blue curve) loss spectrum for $\text{LiFePO}_4$ . . . . .	77
6.8	Experimental $\text{Im}(1/(\epsilon))$ (black curve), $\epsilon_1$ (red curve), $\epsilon_2$ (blue curve) loss spectrum for $\text{FePO}_4$ . . . . .	77
6.9	Calculated $\text{Im}(1/(\epsilon))$ (black curve), $\epsilon_1$ (red curve), $\epsilon_2$ (blue curve) loss spectrum for $\text{FePO}_4$ . . . . .	78
6.10	Calculated imaginary part of the optical conductivity ( $\sigma(\omega)$ ) for (a) $\text{LiFePO}_4$ (b) $\text{FePO}_4$ shown for the three cartesian co-ordinates. . .	79
6.11	Calculated and experimental real optical conductivity ( $\sigma(\omega)$ ) for (a) $\text{LiFePO}_4$ (b) $\text{FePO}_4$ . The ( $\sigma(\omega)$ ) was calculated for the three main cartesian co-ordinates ( $\sigma(\omega)_{xx}$ ), ( $\sigma(\omega)_{yy}$ ), ( $\sigma(\omega)_{zz}$ ). The letters $A_1, A_2, A_3, A_4$ mark the energy regions of the observed peak features . . . . .	80
6.12	Partial density of states (pDOS) for Li(black curve), Fe (red curve), O (blue curve) and P (green curve) for (a) $\text{LiFePO}_4$ (b) $\text{FePO}_4$ . . .	82
6.13	Band structure of $\text{LiFePO}_4$ showing (a) Fe 3d character (b) O 2p character of the bands between -9 eV/ 9eV. The radius of the colored circle represents the degree of respective character in a band. . . .	83
6.14	Band structure of $\text{FePO}_4$ showing (a) Fe 3d character (b) O 2p character of the bands between -9 eV/ 9eV. The radius of the colored circle represents the degree of respective character in a band. . . .	84
6.15	Partial $\epsilon_2$ calculated from selected bands in $\text{LiFePO}_4$ . The black curve shows the calculated total $\epsilon_2$ . The coloured curves shows the partial $\epsilon_2$ calculated for transitions involving bands -44.8/-19.7 eV to the conduction band (CB), -19.7/-9.4 eV to CB, -9.4/-6.9 eV to CB, -6.9/-5.1 eV to CB, -5.1/-4.1 eV to CB, -4.1/-3.2 eV to CB, -3.2/-0.2 eV to CB . . . . .	85

6.16	Partial $\epsilon_2$ calculated from selected bands in $\text{FePO}_4$ . The black curve shows the calculated total $\epsilon_2$ . The coloured curves shows the partial $\epsilon_2$ calculated for transitions involving bands -20.5/-17.9 eV to the conduction band, -17.9/-6.8 eV to CB, -6.8/-5.6 eV to CB, -5.6/-4.6 eV to CB, -4.6/-2.5 eV to CB, -2.5/-1.4 eV to CB, -1.4/-0.2 eV to CB	86
6.17	A schematic picture for the changes in the electronic structure with delithiation. (a) $\text{LiFePO}_4$ can be considered to be Mott-Hubbard insulator (b) $\text{FePO}_4$ can be considered to be charge-transfer insulator. The red arrows indicate the possible interband transitions observed in the VEELS spectra of $\text{FePO}_4$	88
7.1	The fine structure of the O-K edge before and after delithiation. The various peaks have been labeled as peaks A, B, C	93
7.2	PDOS for O states shown for (a) $\text{LiFePO}_4$ (b) $\text{FePO}_4$ . The major difference between the PDOS for the two phases is in the energy region 2-6 eV in the areas marked green. $\text{FePO}_4$ the DOS is shifted to lower energies between 2-4 eV while in $\text{LiFePO}_4$ it is shifted to higher energies between 4-6 eV	95
7.3	The inequivalent O sites in $\text{LiFePO}_4$ . (After Ref [11])	96
7.4	Calculated O-K edge for the various inequivalent Oxygens in (a) $\text{LiFePO}_4$ and $\text{FePO}_4$ .	97
7.5	The fine structure of the $\text{FeL}_{2,3}$ edge before and after delithiation.	99
7.6	Fe L3 edge for (a) $\text{Fe}^{2+}$ in $\text{LiFePO}_4$ and (b) $\text{Fe}^{3+}$ in $\text{FePO}_4$	100
7.7	$\text{FeL}_{2,3}$ edge calculated for $\text{Fe}^{2+}$ and $\text{Fe}^{3+}$ calculated for an increasing values of $10Dq$ .	101
7.8	Ground state configurations for (a) $\text{Fe}^{2+}$ in $\text{LiFePO}_4$ and (b) $\text{Fe}^{3+}$ in $\text{FePO}_4$	102
7.9	$\text{FeL}_{2,3}$ edge calculated for $\text{Fe}^{2+}$ and $\text{Fe}^{3+}$ for an varying values of $\Delta$ .	104
7.10	Calculated $\text{Fe}^{2+}$ and $\text{Fe}^{3+}$ spectra. The values of the parameters used in the calculations are listed in Table 8.1	105
7.11	Li-K and Fe $M_{2,3}$ edges for $\text{LiFePO}_4$ and $\text{FePO}_4$	107
7.12	P-K edge for $\text{LiFePO}_4$ and $\text{FePO}_4$ .	108
8.1	The charge-discharge curve for the delithiation of $\text{LiFePO}_4$ . The charge-discharge process is accompanied by phase transformation between the two end-members $\text{LiFePO}_4$ and $\text{FePO}_4$	113
8.2	X-ray diffraction pattern of partially delithiated $\text{Li}_{0.5}\text{FePO}_4$ sample. The results show that at a partially delithiated state two phases $\text{FePO}_4$ and $\text{LiFePO}_4$ co-exist	114
8.3	Microstructure from a partially delithiated sample. The grains are characterized by a defect that run parallel to the elongation axis of the particle. The dotted square shows the region where HRTEM images were obtained	114

---

8.4	(a) HRTEM image from a partially delithiated grains (b)Colour map showing the distribution of the $d_{010}$ lattice parameter in the HRTEM image. The broad white arrow shows the integrated region where the intensity profiles were obtained (c) Intensity profile obtained from the lattice parameter distribution map. . . . .	115
8.5	(a) HRTEM image from a partially delithiated grains (b)Colour map showing the distribution of the $d_{010}$ lattice parameter in the HRTEM image. The broad white arrow shows the integrated region where the intensity profiles were obtained (c) Intensity profile obtained from the lattice parameter distribution map. . . . .	116
8.6	(a) Atomic model of the $\text{LiFePO}_4\text{-FePO}_4$ interface (b)Simulated HRTEM images obtained from the atomic model . . . . .	117
8.7	Simulated HRTEM images for various thicknesses layer thicknesses(a) 2nm (b) 5 nm (c) 10 nm (d) 20 nm . . . . .	118
8.8	An intensity profile of the distribution of of the (011) lattice parameters in figure 8.6. The experimental interplanar distance between the (011) planes is 0.3745 nm for $\text{LiFePO}_4$ and 0.3687 nm for $\text{FePO}_4$ . The profiles are shown for various $\text{LiFePO}_4 - \text{FePO}_4$ model thicknesses 2 nm, 20 nm and 50 nm. . . . .	119
8.9	Streaking in the FFT obtained from calculated HRTEM image (a). an experimental HRTEM image is shown in comparison (b). The dotted red squares show single reflections. . . . .	120
8.10	Amorphization of $\text{Li}_{0.5}\text{FePO}_4$ grain under the electron beam. . . . .	120

---

## Notations for chapter 1.

$\mu$	Chemical potential	4
$G$	Gibb's free energy	4
$F$	Faraday's constant	4
$\mu_a$	chemical potentials of the lithium in cathode	4
$\mu_b$	chemical potentials of the lithium in anode	4

## Notations for chapter 2.

$t_{2g}$	$d_{z^2}$ and $d_{x^2-y^2}$ Fe 3d orbitals in an octahedral crystal field	8
$e_g$	$d_{xy}$ , $d_{xz}$ , and $d_{yz}$ Fe 3d orbitals in an octahedral crystal field	8
$U$	Hubbard parameter	10
$L$	Ligand	11
$\underline{L}$	denotes a core-hole in the ligand	11

## Notations for chapter 3.

$\lambda$	wavelength of the electron	22
$\theta_B$	Bragg angle	22
$e$	electron charge	23
$v$	electron velocity	23
$m$	electron mass	23
$E_0$	energy of incident electrons	23
$k_0$	momentum of the incident electrons	23
$\Delta E$	energy lost by inelastically scattered electrons	23
$q$	momentum transfer	23
$\alpha$	convergence semi angle giving the range of incident wave-vectors	23
$\beta$	collection angle giving the range of electrons collected	23
$\psi_i$	the wavefunction representing the initial state of the electron	24
$\psi_f$	the wavefunction representing the final state of the electron	24
$\hbar\omega$	energy of a photon given by Planck's constant times frequency	25
$\theta_0$	characteristic scattering angle	25
$\epsilon(\omega, q)$	dielectric function	26
$\epsilon_1$	real part of the dielectric function	27
$\epsilon_2$	imaginary part of the dielectric function	27
$E_g$	band gap energy	30
$c_0$	velocity of light	30
$\frac{-1}{\epsilon(\omega, q)}$	energy loss function	35
$\psi_e(\mathbf{r})$	exit wavefunction for electrons exiting a crystal	36
$V(x, y, z)$	crystal potential	37
$V(x, y)$	projected crystal potential	37



---

$T(\mathbf{k}, \delta F)$	contrast transfer function	37
$\delta F$	defocus	38
$C_s$	spherical aberrations	38
$C_s$	chromatic aberrations	38
$g_i$	reciprocal lattice vector	39
$P_{gi}$	phase of a particular reciprocal vector	40
$U(\mathbf{r})$	displacement vector field	39
$\sigma(\omega)$	optical conductivity	40

## Notations for chapter 4.

$H$	Hamiltonian	46
$V_{\text{ext}}$	external potential	46
$V_{e-e}$	electron-electron Coulomb inter-cation	46
$n(\mathbf{r})$	electron density	46
$\rho$	ground state density	46
$F[n(\mathbf{r})]$	density functional	47
$E_{xc}[\rho]$	exchange-correlation (xc) functional	47
$\mu_l(r, E_l)$	radial function	51
$Y_{lm}(r)$	spherical harmonics	51
$H_{\text{ave}}$	Hamiltonian for the kinetic energy and electron nucleus interaction	55
$H_{ls}$	Hamiltonian for the spin-orbit interactions of the electron	55
$H_{ee}$	Hamiltonian for electron-electron interactions	55
$\Delta$	charge transfer energy.	56

## Notations for chapter 6.

$N_{\text{eff}}(E)$	effective number of electrons involved in interband transitions	72
$\hbar\omega_f$	energy of a plasmon in the free electron model	86

## Notations for chapter 7.

$s$	spin quantum number	98
$l$	orbital angular momentum	98
$j$	angular momentum	98
$L$	total orbital angular momentum	98
$S$	total spin	98
$J$	total momentum	98
$10Dq$	energy separating the the $t_{2g}$ and $e_g$ states	99
$U_{dd}$	3d-3d Coulomb repulsion	103
$U_{pd}$	Fe-2p-Fe-3d Coulomb interaction	103
$\kappa$	slater integrals	103

---

## Notations for chapter 7.

$d_{hkl}$       interplanar distance between the (hkl)atomic planes ..... 115

# List of abbreviations

1D	one-dimensional
2D	two-dimensional
3D	three-dimensional
BZ	Brillouin Zone
CCD	Charge Coupled Device
CB	Conduction Band
DOS	Density of States
ELF	Energy Loss Function
EELS	Electron Energy Loss Spectroscopy
ELNES	Extended Energy Loss Fines Structures
eV	Electron Volts
XC	Exchange Correlation
FEG	Field Emission Gun
FFT	Fast Fourier Transform
FLAPW	Full potential Linearized Augmented Plane Wave
GIF	Gatan Image Filter
GPA	Geometrical Phase Analysis
GGA	Generalized Gradient Approximation
HRTEM	High Resolution Electron Microscopy
IBZ	Irreducible Brillouin Zone
JDOS	Joint Density of States
kV	Kilo Volts
LDA	Local Density Approximation
LHB	Lower Hubbard Band
pDOS	Partial Density of States
TEM	Transmission Electron Microscope
UHB	Upper Hubbard Band
VB	Valence Band
VEELS	Valence Electron Energy Loss Spectroscopy
XAS	X-ray Absorption Spectroscopy
XRD	X-ray Diffraction



# Part I

## Introduction



## Introduction

Technological advances in electronics and concerns about the impact of fossil fuels on the environment, have lead to intensive research efforts to try and find cheaper and environmentally friendly sources of energy. This has also included efforts to develop better ways to store energy. One of the areas where a lot of research efforts have concentrated on, is the development of rechargeable, safe and high-energy lithium (Li) ion batteries. Li ion batteries are cheaper and have a higher energy density when compared to other rechargeable battery technologies such as lead acid and nickel metal hydride (Ni-MH) [1, 2]. This has lead to Li ion batteries being applied in most of the consumer electronic products and in many of the hybrid-electric vehicles. The importance of Li ion batteries in technological applications has resulted in intensive research and engineering efforts aimed at producing better batteries. Li-ion batteries are a type of rechargeable batteries in which Li ions move between the anode and cathode. A Li-ion battery can be divided into three main parts: cathode, electrolyte and anode. In the cathode the reduction process occurs while at the anode the oxidation process takes place. The electrolyte acts a separator and it allows the movement of ions but is restricts the movement of electrons. Electrical energy in Li ion batteries is generated by the conversion of chemical energy through reduction-oxidation (redox) reactions at the anode and cathode with the movement of Li ions between the cathode and anode. In the reduction process electrons are accepted from the external circuit while in the oxidation process the electrons are donated into the external circuit. The process of lithium moving into the cathode is referred to as lithiation (or intercalation), and the reverse process, in which lithium moves out of the cathode is referred to as delithiation (or deintercalation). When a cell is discharging,

lithium ions are extracted from the anode and inserted into the cathode. When the cell is charging, the reverse process occurs: lithium is extracted from the cathode and inserted into the anode [1, 3]. A schematic of this process is shown in Figure 1.1.

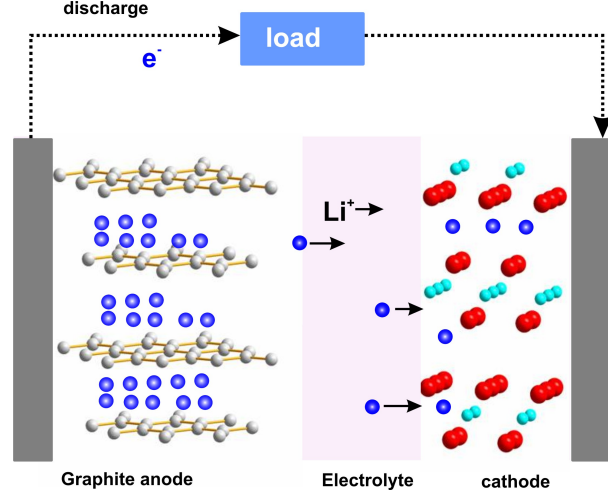


*Figure 1.1: The discharge process in a Li battery where  $\text{Li}^+$  are inserted into the cathode lattice*

The driving force that causes electron to move from the anode to the cathode is called the cell potential or the cell voltage. It represents a potential difference between the materials in the cathode and the anode. The cell voltage is directly related to the thermodynamic changes in energy due to the corresponding chemical reactions. The most important quantity that expresses the changes in the energy in the cell as function of Li concentration changes in the host matrix is the chemical potential  $\mu$  [1]. This is defined as,

$$\mu = \frac{\partial G}{\partial x} \quad (1.1)$$

Where  $G$  is the Gibbs free energy and  $x$  is the number of inserted Li ions. The free energy change can also be expressed as,

$$\Delta G = -nFE \quad (1.2)$$

Where  $n$  is the number of electrons in both electrode-reactions,  $F$  is the Faraday's constant  $E$  is the potential difference between the electrodes. Combining equations (1.2) and (1.3), a relationship between the electrical and chemical energy in the system is obtained,

$$\Delta G = -nFE = \mu_a + \mu_b \quad (1.3)$$

where  $\mu_a$  and  $\mu_b$  are the chemical potentials of the Li ion in the cathode and anode. The cell potential is thus determined by the difference between the chemical potential of the Li in the anode and cathode. The processes mentioned here



are characterized by smaller multiple processes occurring over different time and length scales including, charge-transfer, charge-carrier and mass transport within the bulk, across interfaces as well as structural changes and phase transformations due to changes in the concentration of Li ions [4–7].

Currently most batteries use graphite as the anode. The cathode is generally a layered oxide, such as lithium cobalt oxide, a polyanion such as lithium iron phosphate, or a spinels, such as lithium manganese oxide. The choice of the materials for the anode, cathode, and electrolyte can change dramatically the properties such as voltage, capacity, life-span, and safety of a lithium ion battery [1,2,6–9]. As such, the ability of a Li ion battery system to provide energy is in part dependent on the properties of the materials used for the anode, cathode and the electrolyte. Additionally, the fundamental properties of materials used in Li ion batteries are governed by their electronic and crystal structure. This means that a lot of research efforts have gone into understanding the structure-property relationship of the materials that make up a Li ion battery. As a consequence, the study of electronic and crystal structure of materials used in Li ion batteries is fundamental if better Li ion batteries are to be developed.

Lithium iron phosphate,  $\text{LiFePO}_4$ , is one the materials used as a cathode material in Li ion batteries and is the focus of this thesis.  $\text{LiFePO}_4$  shows good electrochemical properties such as high capacity, thermal and structural stability. However, it is also characterized by low electronic conductivity and in addition the extraction/insertion of Li ions from/to the lattice is not yet understood. This has lead to intensive research efforts aimed at understanding the relationship between electronic and crystal structure of  $\text{LiFePO}_4$  and its electrochemical properties. Such structure-property relationship investigations involve extensive use of either theoretical calculations, experimental investigations or both. TEM techniques including HRTEM, EELS provide a set of powerful techniques with which the atomic and electronic structure of materials can be investigated. Combined with theoretical calculations, TEM techniques are powerful means of providing fundamental understanding of electrochemical properties of  $\text{LiFePO}_4$ . This dissertation combines experimental TEM and theoretical calculations with an aim of understanding electronic properties and structure properties in  $\text{Li}_{(1-x)}\text{FePO}_4$  ( $x=0,..1$ ). The structure of this thesis is organized as follows.

- Chapter 2 gives a brief overview of Li ion battery technology and the application of  $\text{LiFePO}_4$  as a cathode material in Li ion batteries. The chapter reviews the common problems that hinder wider application of  $\text{LiFePO}_4$  in Li ion batteries. The state-of-the-art in  $\text{LiFePO}_4$  research is also introduced. The main objectives in this thesis are also introduced in this chapter.
- Chapter 3 presents the basic theory behind the EELS and HRTEM methods used in this thesis. This includes EELS spectrum acquisition, spectrum analysis and HRTEM analysis of structure. This chapter also briefly introduces the sample preparation methods.

- Chapter 4 introduces the theoretical methods applied in this thesis. In order to interpret the experimental EELS spectra theoretical calculations are necessary. In this thesis Density functional (DFT) and ligand crystal field based methods are used in the calculation of spectra and electronic structure.
- Chapter 5 presents the results on the effects of the electron beam on the obtained EELS results. Using electrons as a probe can cause physical damage, electronic and chemical changes in the sample being investigated. This may modify the obtained results and can lead to errors in the interpretation of experimental results. It is therefore necessary to study the effects of the electron beam on  $\text{LiFePO}_4$ .
- Chapter 6 presents the results, analysis and discussion of VEELS for  $\text{LiFePO}_4$  and  $\text{FePO}_4$ . The chapter also gives the results on electronic structure calculations which are necessary in order to interpret both spectra. The interpretation of the spectra is given in the context of the electronic structure of  $\text{LiFePO}_4$  and the changes associated with the extraction of Li ions from the the lattice.
- Chapter 7 presents the results, analysis and discussion on core-loss studies for  $\text{LiFePO}_4$  and  $\text{FePO}_4$ . Experimental spectra are compared with theoretical core-loss spectra derived from DFT and ligand field calculations. The interpretation of the spectra is given in the context of the electronic structure of  $\text{LiFePO}_4$  and the changes associated with the extraction of Li ions from the the lattice.
- Chapter 8 gives the results on structural investigations on partially delithiated  $\text{Li}_{(0.5)}\text{FePO}_4$ . This is done through the use HRTEM analysis. The interpretation of the spectra is given in the context of the Li delithiation mechanism in  $\text{LiFePO}_4$ .
- Chapter 9 provides a detailed summary of all the results obtained in this thesis. In particular this chapter attempts to present an overview of what the various results mean for delithiation process.

# Structural, electronic and electrochemical properties of $\text{Li}_{(1-x)}\text{FePO}_4$

In this chapter we set the framework of this thesis by introducing the electronic, structural and electrochemical properties of  $\text{LiFePO}_4$ . We begin by discussing the structural and bonding properties of  $\text{Li}_{(1-x)}\text{FePO}_4$  in Sec.2.1. In this chapter and in the thesis the stoichiometry  $\text{Li}_{(1-x)}\text{FePO}_4$  stands for the phase formed after delithiation and not solid solutions. These include lithiated phase  $\text{LiFePO}_4$  ( $x=0$ ), partially delithiated phase  $\text{Li}_{(0.5)}\text{FePO}_4$  ( $x=0.5$ ), and fully delithiated  $\text{FePO}_4$  ( $x=1$ ). Applications of  $\text{LiFePO}_4$  in Li ion batteries are then introduced in Sec. 2.2. In this section the state-of-the art in  $\text{LiFePO}_4$  research is also introduced. In particular the emphasis has been put on the electronic and structural investigations of  $\text{LiFePO}_4$  before and after delithiation. The main objectives in this thesis are given at the end of this chapter in Sec.2.3

## 2.1 Structure and bonding

$\text{LiFePO}_4$  crystallizes as the olivine type,  $\text{MNXO}_4$ , where M and N are cations with different sizes. In  $\text{LiFePO}_4$  the cations are Li and Fe respectively.  $\text{LiFePO}_4$  is indexed to the orthorhombic space group Pnma, the lattice parameters are  $a = 10.334 \text{ \AA}$ ,  $b = 6.008 \text{ \AA}$ ,  $c = 4.693 \text{ \AA}$ . Figure 2.1 shows a linked polyhedra model of  $\text{LiFePO}_4$ , the Iron ( $\text{Fe}^{2+}$ ) ions are in a corner sharing  $\text{MO}_6$  octahedra which is perpendicular to the a axis. The lithium ions ( $\text{Li}^+$ ) are in edge-sharing  $(\text{LiO}_6)^{11-}$

octahedra along the **b** axis. The P ion form a tetrahedral group PO<sub>4</sub> which connects various planes [10–12]. The oxygen (O<sup>2-</sup>) forms a tetrahedra around phosphorous atoms and octahedral around iron (Fe<sup>2+</sup>) and lithium (Li<sup>+</sup>) atoms.

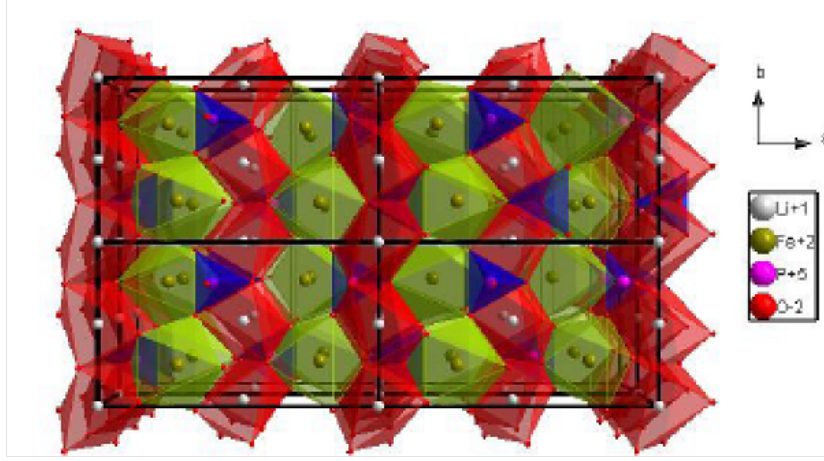


*Figure 2.1: The crystal structure of LiFePO<sub>4</sub> showing the (LiO<sub>6</sub>)<sup>11-</sup>, (FeO<sub>6</sub>)<sup>10-</sup> octahedral and (PO<sub>4</sub>)<sup>3-</sup> tetrahedral units.*

In the (FeO<sub>6</sub>)<sup>10-</sup> and (LiO<sub>6</sub>)<sup>11-</sup> the cations are each surrounded by six anions, Oxygen atoms. This means that properties of material are influenced by strong crystal field effects. Two of the 3d orbitals, 3d<sub>x<sup>2</sup>-y<sup>2</sup></sub> and 3d<sub>z<sup>2</sup></sub> on the Fe<sup>2+</sup> ion point directly toward the six O<sup>2-</sup> ions, the other three orbitals 3d<sub>xy</sub>, 3d<sub>xz</sub>, and 3d<sub>yz</sub> lie between the O<sup>2-</sup> ions [13,14]. Due to the repulsion between electrons on the O<sup>2-</sup> ions and electrons in the 3d orbitals on the Fe<sup>2+</sup> ion the normally degenerate energy levels of the Fe iron 3d levels are split by the surrounding ligand field, also known as the crystal field. This is shown in Figure 2.3

The energy of the two orbitals d<sub>x<sup>2</sup>-y<sup>2</sup></sub> and d<sub>z<sup>2</sup></sub> facing the O<sup>2-</sup> ligands increases than the energy of the other three 3d<sub>xy</sub>, 3d<sub>xz</sub>, and 3d<sub>yz</sub>, which face in-between the oxygen ligands. The d<sub>xy</sub>, d<sub>xz</sub>, and d<sub>yz</sub> orbitals are known as the t<sub>2g</sub> orbitals. The 3d<sub>x<sup>2</sup>-y<sup>2</sup></sub> and d<sub>z<sup>2</sup></sub> orbitals, on the other hand, are called the e<sub>g</sub> orbitals. For a transition metal in octahedral symmetry, the d<sub>z<sup>2</sup></sub> and d<sub>x<sup>2</sup>-y<sup>2</sup></sub> atomic orbitals directly overlap with the p<sub>x</sub>, p<sub>y</sub>, and p<sub>z</sub> orbitals of the oxygen along the octahedral directions. The d<sub>xy</sub>, d<sub>xz</sub>, and d<sub>yz</sub> orbitals point away from the oxygen and have no σ overlap with its p orbitals and form a set of nonbonding t<sub>2g</sub> bands. This is shown in Figure 2.3.

In addition to the t<sub>2g</sub> and e<sub>g</sub> bands, there are also t<sub>1u</sub> and a<sub>1g</sub> bands which are formed from the overlap between oxygen-p and metal-p, and metal-s orbitals, respectively. The crystal structure of the delithiated phase, FePO<sub>4</sub>, is similar to that of LiFePO<sub>4</sub> with a orthorhombic unit cell and space group Pnma. The lattice parameters of FePO<sub>4</sub> are a= 9.760 Å, b= 5.752 Å, b= 4.756 Å. Similar to LiFePO<sub>4</sub>, the Fe ion is located at the middle of an FeO<sub>6</sub> octahedron, but one which is more distorted than in LiFePO<sub>4</sub> [12,15]. In LiFePO<sub>4</sub>, the Fe<sup>2+</sup> ion is in

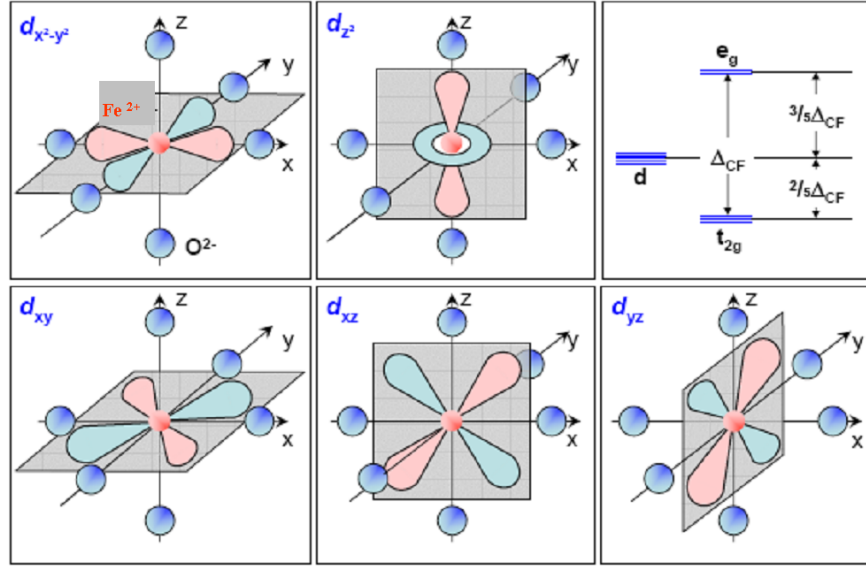


**Figure 2.2:** The shape of the 3d orbitals in an octahedral crystal field of (octahedral symmetry- $O_h$ ). The two  $e_g$  orbitals  $d_{x^2-y^2}$  and  $d_{z^2}$  point towards the  $O^{2-}$  ions (ligands) while the  $t_{2g}$  ( $d_{xy}$ ,  $d_{xz}$ ,  $d_{yz}$ ) 3d orbitals point between the ligands. The  $t_{2g}$  and  $e_g$  are separated by an energy  $\Delta_{CF}$  (or  $10Dq$ ). The colour scheme shows the sign of the wavefunction where  $+$  = red, and  $-$  = blue. (After Gross, Ref [14])

a high spin state with an electronic configuration of  $t_{2g}(\uparrow)^3 e_g(\uparrow)^2 t_{2g}(\downarrow)^1$  state. This configuration shows that three electrons occupy the spin up  $t_{2g}$  levels, two electrons occupy the spin up  $e_g$  levels and one electron occupies the spin-down  $t_{2g}$  level. Similarly the  $Fe^{3+}$  ion in  $FePO_4$  is also in a high spin state with the configuration  $t_{2g}(\uparrow)^3 e_g(\uparrow)^2$  three electrons occupy localized  $t_{2g}$  levels, and two electrons in the  $e_g$  level. In  $LiFePO_4$  the highest occupied orbital is the  $t(\downarrow)_{2g}^1$  while in  $FePO_4$  it is the  $e(\uparrow)_{2g}^2$ .

$LiFePO_4$  and  $FePO_4$  belong to a class of intriguing materials known as transition metal compounds. These compounds formed when a d-block (transition) metal are covalently or ionically bonded to one or more ligands. These compounds show a lot of interesting properties such as ferromagnetism, ferrimagnetism, anti-ferromagnetism, insulation, conductivity, superconductivity, ferroelectricity, piezzo-electricity and many other interesting properties. Transition metal compounds also show a huge variety in electron conductivity ranging from extreme insulating compounds such as  $MnO$  with a conductivity of  $\sigma \approx 10^{-15} \Omega^{-1} \text{cm}^{-1}$  to metallic conducting  $ReO$ , whose conductivity  $\sigma \approx 10^5 \Omega^{-1} \text{cm}^{-1}$  is nearly equal to that of copper [13]. In many of these compounds including  $LiFePO_4$  the valence 3d orbitals are partially filled and these compounds are thus predicted by the Bloch's band theory to be metallic. In the band structure scheme materials can be classified as metallic, semi-conducting or insulating depending on whether the valence band is completely or partially filled and the size of the energy gap between

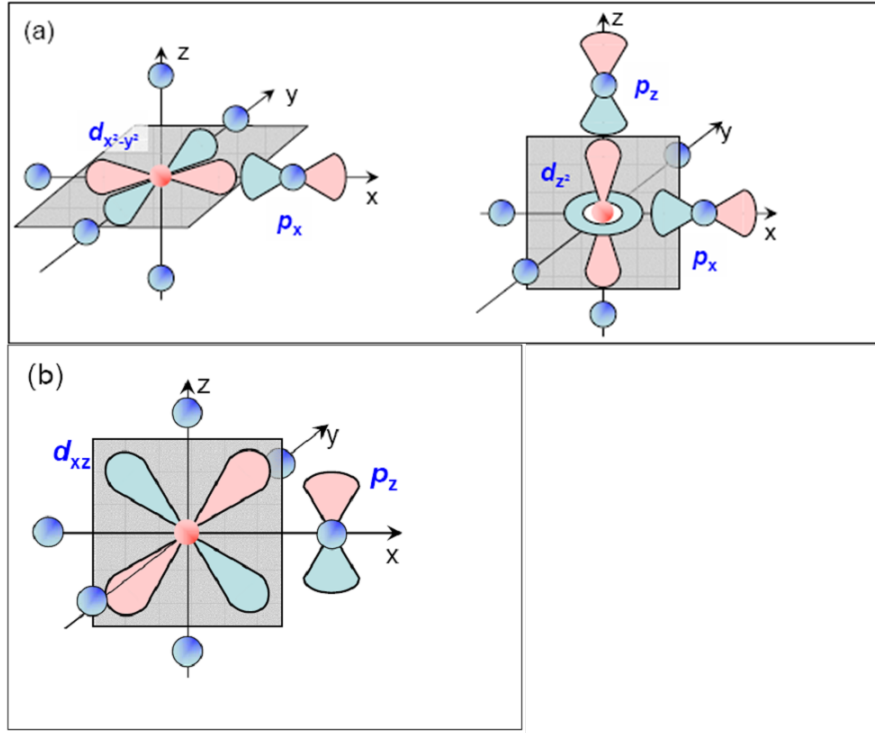


*Figure 2.3: Hybridization between the 3d orbitals of a transition metal ion with the P orbitals of the ligand. (a) The overlap and hybridization of the  $d_{x^2-y^2}$  and  $d_{z^2}$  ( $e_g$ ) with the  $p_x$  and  $p_z$  orbitals of the ligand forming the  $\sigma$  bond. (b) Overlap and hybridization of the  $d_{xz}$  orbital with the ligand  $p_z$  orbital. This forms the  $\pi$  type of bond. The colour scheme shows the sign of the wavefunction where  $+$  = red, and  $-$  = blue. (After Gross, Ref [14])*

the valence and conduction band [16, 17]. However, many transition metal compounds have been experimentally shown to be insulators despite having partially filled 3d valence orbitals. In a series of ground breaking papers [18, 19] the origin of the insulating behaviour of those oxides was explained to be arising from strong Coulomb interactions between the delocalized 3d electrons. In order to move electrons from one ion to another this coulomb repulsion had to be overcome, thus opening a gap between valence and conduction bands. These kind of insulators are then known as Mott-insulators. In Mott-insulators moving a d electron from one ion to another one must overcome the strong on site Coulomb repulsion. The energy that must be overcome before such a transfer can take place is represented by the Hubbard parameter,  $U$ , [20].

$$U = (E_0(d^{n-1}) - E_0(d^n) + E_0(d^{n+1}) - E_0(d^n)) \quad (2.1)$$

$d^n$ , shows that there are  $n$  electrons in the d shell of the transition metal ion. A metal ion with an added electron is denoted by  $d^{n+1}$  and a metal ion with a hole is denoted by  $d^{n-1}$ . Further it was shown that the ligand that binds the transition metal ion, in most cases the oxygen ligand modifies the electronic properties of

the compound giving rise to a another class of insulators known as charge-transfer insulators [21]. In the charge-transfer insulators, moving an electron from the ligand to the transition metal ion one must overcome the charge transfer energy. The charge transfer energy is given by

$$\Delta = E_0(d^{n+1}\underline{L}) - E_0(d^n) \quad (2.2)$$

The schematic picture showing the density of states in these two insulator types is shown in Figure . Due to the strong electron correlation, the d band is split to the two components; the occupied band termed the lower Hubbard band (LHB) and the unoccupied band termed the upper Hubbard band (UHB).

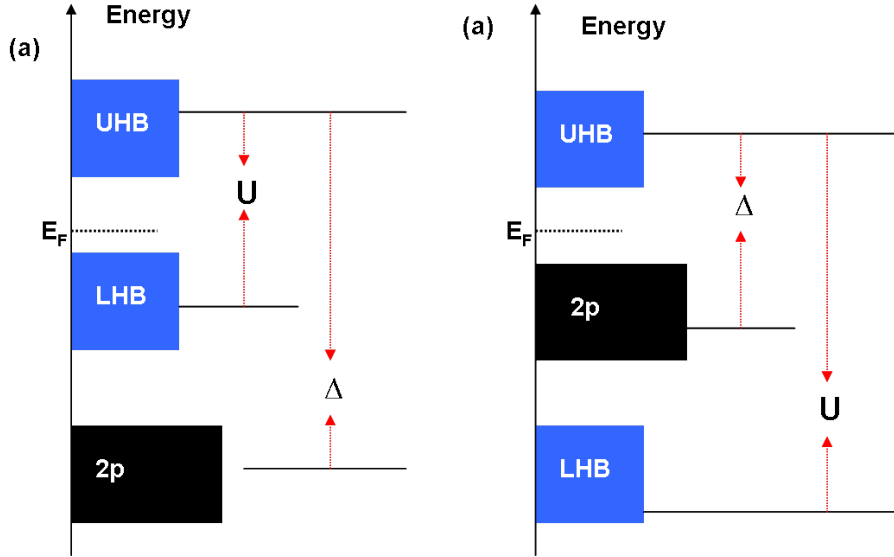


Figure 2.4: Schematic density of states for (a) the Mott-Hubbard insulator and (b) the charge-transfer insulator. LHB and UHB indicate the lower Hubbard band and upper Hubbard band, respectively.  $E_F$  represents the fermi level

In LiFePO<sub>4</sub> and FePO<sub>4</sub> the six oxygen (O<sup>2-</sup>) ions are denoted by  $L$  for ligand. In the case when one of the O-2p electrons are removed this is denoted by  $\underline{L}$ . Such interactions are not taken into consideration in Bloch's band theory and such the band theory was not sufficient to explain the insulating or conduction properties of LiFePO<sub>4</sub>. The electronic structure, charge transfer, charge carriers and charge compensation in transition metal compounds is a vast field and very complex and a lot of active research is being done in this area. A more detailed review on the physics of transition metal compounds can be found in literature [19–21].



## 2.2 LiFePO<sub>4</sub> in Li ion batteries

### 2.2.1 Electrochemical properties

LiFePO<sub>4</sub>, was first reported as a cathode material by Padhi *et al* [10]. This came as a result of attempts to find cheaper and less toxic materials to replace the currently applied Cobalt oxides, LiCoO<sub>2</sub>. LiCoO<sub>2</sub> has a high theoretical capacity but it delivers only half of the theoretically possible capacity since LiCoO<sub>2</sub> cannot be delithiated beyond Li<sub>0.5</sub>CoO<sub>2</sub> due to safety concerns [22]. In addition Cobalt is an expensive material and also toxic. This significantly increases the costs involved during the production of Li ion batteries. The search for replacement cathode materials has mainly concentrated on transition metal compounds including LiMn<sub>2</sub>O<sub>4</sub> and LiNiO<sub>2</sub> and the LiXPO<sub>4</sub> phospho-olivines (x= Fe, Ni, Co, Mn, Va). However, the replacement candidates also have structural, electrochemical or electronic problems that have to be overcome before they can be used in Li ion batteries. LiNiO<sub>2</sub> shows good capacity but is thermally unstable and therefore unsafe for Li ion battery applications. In the case of manganese spinel oxides, LiMn<sub>2</sub>O<sub>4</sub>, structural instabilities and capacity losses are observed on cycling and battery parameters degrade at high temperatures [9]. In the phospho-olivines, most research has concentrated on the LiFePO<sub>4</sub>. LiFePO<sub>4</sub> has a high theoretical voltage of 3.5 V vs Li<sup>+</sup>/Li for the Fe<sup>3+</sup>/Fe<sup>2+</sup> couple, and large theoretical capacity to store charge per unit mass, 170 mA h g<sup>-1</sup> [8, 10, 23]. LiFePO<sub>4</sub> also shows structural and temperature stability during cycling operations, which is in contrast to LiNiO<sub>2</sub> cathodes and LiMn<sub>2</sub>O<sub>4</sub> which show severe temperature and structural instability respectively. These properties make LiFePO<sub>4</sub> based-cells attractive candidates for high power energy applications such as hybrid electric vehicles.

Despite having good electrochemical and structural characteristics, LiFePO<sub>4</sub> cathodes are shown to suffer from poor rate capability [10, 24–26]. Good rate capability in a cathode means fast-charging and high-current discharge, properties which are essential if Li ion battery is to find wider applications especially in hybrid electric car applications. It has been argued that the low rate capability arises from poor electron conductivity within the LiFePO<sub>4</sub> lattice combined with poor Li ion transport across the LiFePO<sub>4</sub>- FePO<sub>4</sub> interface [10, 27]. This has resulted in the development of several approaches attempting to overcome this problem. These approaches included synthesis, processing and theoretical approaches. Synthesis and processing approaches include coating of LiFePO<sub>4</sub> with conductive carbon phases [24–26], post-processing of LiFePO<sub>4</sub> particle to induce formation of conductive metallic phases on the surface of LiFePO<sub>4</sub> particle [28] and the use of different synthesis methods to try and influence particle morphology and subsequently improve Li-ion diffusion path [29–31]. An important part of LiFePO<sub>4</sub> research has also involved extensive theoretical and experimental investigations on the structural properties of LiFePO<sub>4</sub> together with electron and Li transport in LiFePO<sub>4</sub> during charge and discharge. It is particularly important



to understand the process of Li ion insertion and extraction in LiFePO<sub>4</sub> if this material is to be optimized for Li battery applications.

### 2.2.2 The delithiation process in LiFePO<sub>4</sub>

The process of lithiation and delithiation in LiFePO<sub>4</sub> is subject to considerable research since it is still poorly understood. Figure 2.5 shows the changes in potential delivered by LiFePO<sub>4</sub> versus the change Li ion extraction. The discharge profile for LiFePO<sub>4</sub> shows a flat curve which means that it is able to provide a constant voltage when discharged at certain discharge rate.

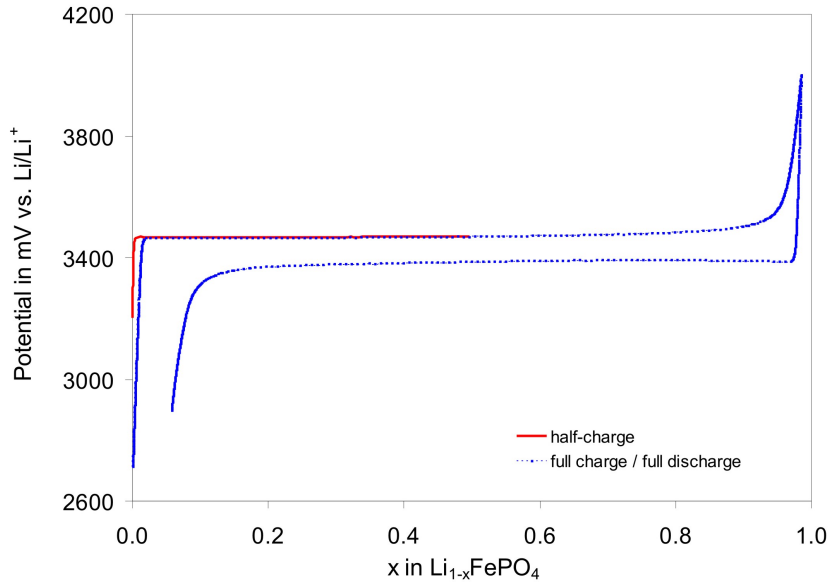
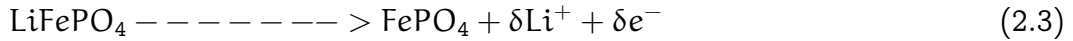


Figure 2.5: The charge-discharge curve for the delithiation of LiFePO<sub>4</sub>

The lithiation and delithiation process in LiFePO<sub>4</sub> is explained by a two-phase mechanism characterized by two end members at  $X = 0$  and  $X = 1$ , LiFePO<sub>4</sub> and FePO<sub>4</sub> respectively. The delithiation process is then represented by the equation,



These two end phases are both orthorhombic and have the same space group, Pnma, with FePO<sub>4</sub> being known as the de-lithiated phase, i.e Li ions have been extracted from the LiFePO<sub>4</sub> lattice [10, 32, 33].

Figure 2.6 shows the phase diagram for LiFePO<sub>4</sub> (T, for triphylite) and FePO<sub>4</sub> (H, for heterosite) and disordered phases (D for disordered) [32, 34]. Figure 2.6 shows that at room temperature the delithiation/lithiation process is mainly a two phase-process. It is characterized by two end members LiFePO<sub>4</sub> and FePO<sub>4</sub> and at a partial delithiated states by a biphasic mixture of both phases. At 200°

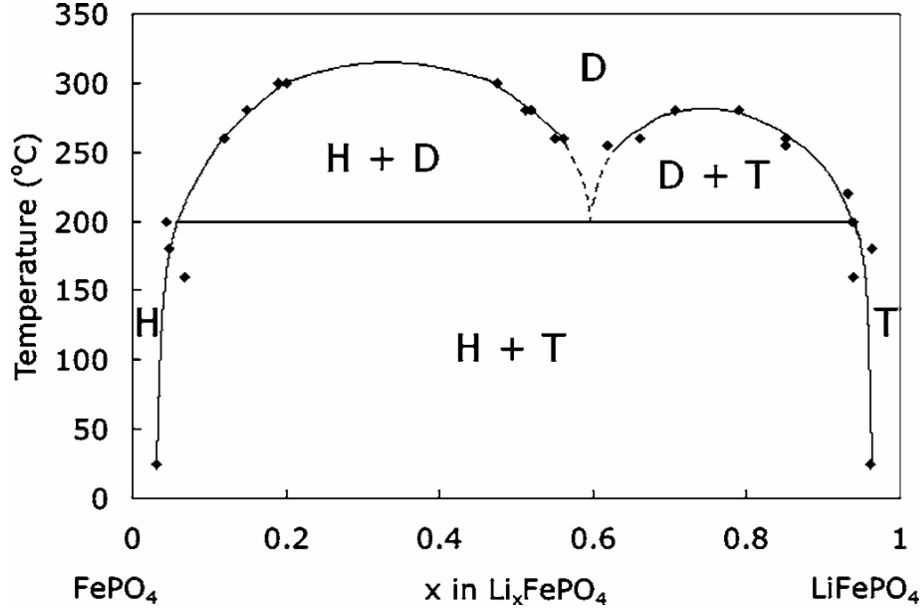


Figure 2.6: Phase diagram of  $\text{Li}_{(1-x)}\text{FePO}_4$ . T, H and D represent the Triphylite ( $\text{LiFePO}_4$ ), Heterosite ( $\text{FePO}_4$ ) and disordered phases respectively. (After Dodd Ref [32])

C mixtures of both phases are observed. Above 300 ° C the disordered phase is dominant. Zhou *et al* [35] then showed that in  $\text{LiFePO}_4 - \text{FePO}_4$  phase reaction is driven by electronic interactions rather than ionic interactions. Lithium ion transport across the  $\text{LiFePO}_4 - \text{FePO}_4$  phase interface during delithiation has been described as an important factor in determining transport properties in  $\text{LiFePO}_4$  [36]. It is therefore crucial to understand the structural characteristics of the lithiation-delithiation process.

Experimentally the structure of partially delithiated  $\text{Li}_{(1-x)}\text{FePO}_4$  grains has been done using electron, x-ray and neutron scattering techniques [12, 15, 32, 37] and HRTEM [36, 38–40]. X-ray and neutron scattering techniques provide invaluable information regarding the structural change during delithiation however, they only provide a volume-averaged picture of the crystal and they are not sensitive to localized structural phenomenon such as nature of phase interfaces, atomic arrangements and defects. HRTEM on the other hand is able to provide atomic and localized information regarding structure in partially delithiated  $\text{Li}_{(1-x)}\text{FePO}_4$  grains. A few important models on the delithiation process in  $\text{Li}_{(1-x)}\text{FePO}_4$  have been developed, some of which are based on results obtained from electron microscopy results.

- Originally a shrinking core model was proposed as the mechanism by which the phase transformation occurs [10, 41]. According to this model the delithiation process starts from the surface of the grain and proceeding inwards. The delithiated phase therefore  $\text{FePO}_4$  phase at the grain surface and grows inwards from surface of the grain while the lithiated parent  $\text{LiFePO}_4$  core

shrinks. At a partially delithiated state the grain should exhibit a core-shell structure with the delithiated phase forming the shell around an undelithiated core. A schematic of the core-shell delithiation model is shown in Figure 2.7.

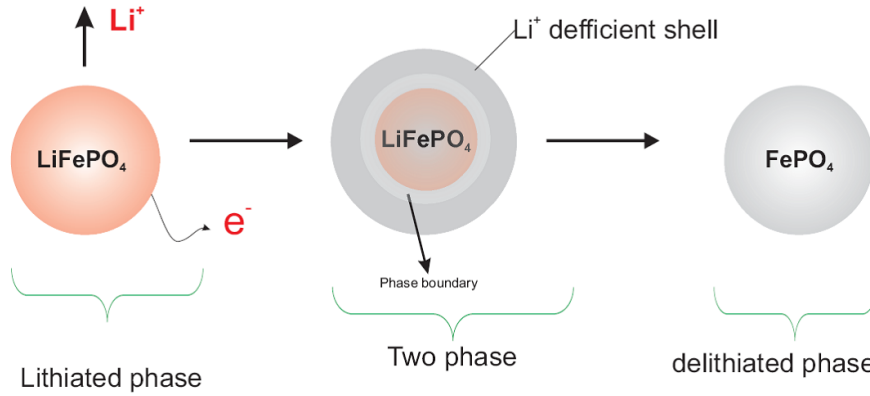


Figure 2.7: A schematic showing the core-shell model of delithiation

- The second model is based on a one-dimensional (1D) nature of Li ion transport. In this model Li ion transport is a one dimensional process that occurs along energetically preferable diffusion channels along the [010] direction. The ensuing structure of partially delithiated grains is thus determined by the one-dimensional nature of the Li ion transport leading to a interface perpendicular to the direction of Li ion transport [38]. A schematic of the 1D delithiation model is shown in Figure 2.8
- The third model is known as the domino cascade delithiation model. This model proposes that the delithiation is so fast that the grain is completely delithiated before the delithiated phase can nucleate. As such at a partially

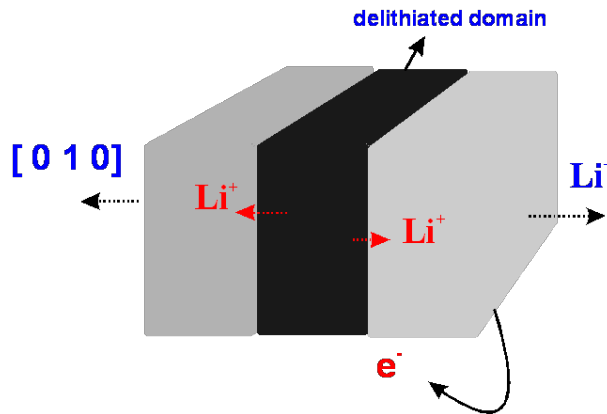


Figure 2.8: A schematic showing the one dimensional model of delithiation

delithiated state, Li<sub>(1-x)</sub>FePO<sub>4</sub> ( $x = 0.5$ ) grains exist as separate LiFePO<sub>4</sub> and fully delithiated grains FePO<sub>4</sub> and not two delithiation states in one grain [36].

In both core-shell and the one-dimensional delithiation models, partially delithiated grains exhibit both undelithiated and delithiated phases in the same grain and the delithiation process is controlled by the Li ion transport across the phase interface. According to domino-cascade model partially delithiated grains should therefore be single phase. It is then possible to cross-check these models by studying the structure and phase distribution of partially delithiated samples. According to the phase diagram 2.6 and the discharge curve 2.5, partially delithiated samples should be an equal mixture of the lithiated phase LiFePO<sub>4</sub> and the delithiated phase FePO<sub>4</sub>. Examining partially delithiated grains should show both phases if the core shell and one-dimensional model are correct or single phases if the domino cascade model is correct.

### 2.2.3 Electronic and structural properties of Li<sub>(1-x)</sub>FePO<sub>4</sub>

#### Electronic calculations

Theoretical and experimental efforts have also been dedicated at understanding and the electronic properties of LiFePO<sub>4</sub>. The first electronic structure calculations carried out on LiFePO<sub>4</sub> showed the material to be semi-metallic [42–44]. This proved to be contrary to what experiments were showing, that LiFePO<sub>4</sub> was insulating. This was because the first electronic structure calculations did not consider the electronic correlations in LiFePO<sub>4</sub> were ignored. However when electronic correlation effects were taken into account LiFePO<sub>4</sub> was then shown to be an insulator [45]. It has then been argued that LiFePO<sub>4</sub> could belong to a class of materials known as small polaron conductors. Polarons are quasi-particles formed whenever holes and electrons are trapped by the ionic cores in the lattice. When charge carriers are placed into a lattice they interact with the surrounding ions, positive cores are attracted to a negatively charged carrier while negative cores are attracted to the positive charged carriers. This interaction leads to distortion of the lattice in the vicinity of the charge carrier and thus trapping it [46, 47]. It was then argued that attempts to introduce extra carriers through doping would not help improve electronic transport in LiFePO<sub>4</sub> very much [45].

#### Spectroscopy on Li<sub>(1-x)</sub>FePO<sub>4</sub>

Experimentally, changes in the electronic structure of Li<sub>(1-x)</sub>FePO<sub>4</sub> have been studied using spectroscopic methods which include EELS [48–51], Raman spectroscopy [52], X-ray absorption spectroscopy [37], Resonant inelastic x-ray scattering (RIXS) [53], Mossbauer spectroscopy [15] and NMR [54]. A lot of spectroscopic investigations have been dedicated to understand the process of charge-

compensation during delithiation/lithiation. When Li ions are extracted from the lattice, charge imbalance is created within the lattice which must be compensated by creating vacancies (ionic compensation), or by electrons (electronic compensation) in order to preserve charge neutrality. The charge-compensation process is one of the driving forces behind the movement of charge within the lattice. A simplified picture of charge compensation in LiFePO<sub>4</sub> holds that removing Li atoms from the lattice results in the Fe ion being oxidized from Fe<sup>2+</sup> to Fe<sup>3+</sup>. Using spectroscopy Miao *et al* [48] and Augusztson *et al* [37] showed that this is not the case in LiFePO<sub>4</sub>. They showed that the oxygen ligand plays an important role in charge transfer and charge compensation. Thus the exchange of charge carriers (electrons and holes) takes place between various transition metal ions and/or ligands and this process can be monitored experimentally using spectroscopy. However the extent of oxygen participation in the charge-compensation process remains unsettled.

Most of the EELS studies on Li<sub>(1-x)</sub>FePO<sub>4</sub> which are mentioned above concentrated on investigating the core-shell excitations. At the beginning of this thesis there was no work investigating VEELS EELS spectra in LiFePO<sub>4</sub> and FePO<sub>4</sub>. This is mainly due to the fact that the interpretation of valence-conduction band spectra is quite difficult. Recently Sigle *et al* [49] and Moreau *et al* [50] reported results on the low-loss spectra in LiFePO<sub>4</sub>. However, these studies did not go into details into the nature and origin of the observed interband transitions and plasmon excitations in the VEELS spectra. For core losses Miao *et al* [48] examined the core-loss EELS spectra of Li<sub>(1-x)</sub>FePO<sub>4</sub> especially the FeL<sub>(2,3)</sub> and the O-K edges. However, due to poor energy resolution of their spectrometer the fine structure of the ionization edges were not examined in details. This thesis presents for the first time a detailed analysis of the excitations in the VEELS spectra of LiFePO<sub>4</sub> and FePO<sub>4</sub> including band structure and spectra calculations. In the core-loss spectra the work presented in this thesis also examines for the first time the effects of Fe-O hybridization on the core-loss EELS spectra Li<sub>(1-x)</sub>FePO<sub>4</sub>. Particularly the effects of Fe 3d-O 2p hybridization of the FeL<sub>2,3</sub> edge and O-K EELS spectra. The approach presented in this thesis provides a more comprehensive spectroscopic method which aids the understanding of the electronic structure in LiFePO<sub>4</sub> and the changes with extraction of Li ions.

## 2.3 Thesis objectives

The issues examined in this thesis include

1. The electronic structure of Li<sub>(1-x)</sub>FePO<sub>4</sub> and associated electronic changes with the extraction of Li ions. In order to achieve this, the following was done
  - An EELS study of both the valence region and the core loss spectra in

LiFePO<sub>4</sub> and FePO<sub>4</sub> was undertaken. This gives the experimental data on the changes in the electronic structure with delithiation.

- Calculation of the electronic band-structure of LiFePO<sub>4</sub> and FePO<sub>4</sub>
  - Calculation of valence, core spectra of LiFePO<sub>4</sub> and FePO<sub>4</sub> using both DFT and atomic multiplet calculations.
2. Investigation into the delithiation process in LiFePO<sub>4</sub>. This was done by atomic scale mapping of phase distribution in partially delithiated Li<sub>0.5</sub>FePO<sub>4</sub> grains using HRTEM analysis.
  3. Effects of the TEM electron beam on the electronic and crystal structure of LiFePO<sub>4</sub>

The results obtained are interpreted in the context of electronic and crystal structure changes during the extraction and insertion of Li ions from LiFePO<sub>4</sub> lattice.

# Part II

## Experimental and Theoretical Background





## Experimental Methods

In this chapter we introduce the experimental used in this work. A major part of this chapter is dedicated at introducing the theory and instrumentation of TEM techniques which have been extensively used in this workd. A general introduction to the TEM is given in Sec. 3.1. EELS methods have been applied mainly to study the electronic structure of  $\text{Li}_{(1-x)}\text{FePO}_4$  before and after delithiation. The details on the theory, experimental and analysis behind the EELS techniques are given in more details in Sec. 3.2 and Sec. 3.3 respectively. The structural properties of  $\text{Li}_{(1-x)}\text{FePO}_4$  are investigated using HRTEM and XRD methods which are discussed in more details in Sec.3.4 and Sec. 3.5. All experimental techniques used in thesis also involve extensive sample preparation techniques and this is given in Sec. 3.6.

### 3.1 Introduction to TEM

The basic theory operation of a TEM is similar to the optical microscope. The crucial difference is that a TEM uses electrons instead of light and electromagnetic lenses for focussing. The electron beam used in a TEM is emitted either through a thermionic process or field emission process. In the thermionic process the electrons are emitted from a  $\text{LaB}_6$  or Tungsten crystal through a heating process. Electrons are emitted from the cathode by heating it to high temperature giving electrons enough energy to escape the atomic energy barriers. In the field emission process the electrons are produced from a single crystal , for example Tungsten through the quantum mechanical tunneling process. In a field emission gun (FEG), an externally applied field lowers the energy barrier of the electrons

in the crystal which allows the electrons to tunnel through the narrowed potential barrier [55–57]. The electrons emitted from the filament are accelerated by a high voltage and focused onto the specimen by a set of condensor lenses. As a direct result of the quantum mechanical formulation, electrons can be considered to have wavelike properties characterized both by a phase and an amplitude. The amplitude and phase of the electrons are modified by interacting with the coulomb potential of electrons in the specimen in a process referred to as scattering. Electrons can undergo either inelastic scattering, where the electron loses some of its kinetic energy to the specimen electrons or elastic scattering (also known as Bragg scattering) where the electron undergoes scattering without losing its kinetic energy. Elastically scattered electrons from the sample are focussed onto the back focal plane of the objective lens where they form a diffraction pattern [57, 58]. The diffraction pattern is a result of the constructive or destructive interference of the beams which have been elastically scattered in the sample. The diffraction pattern consists of series of spots or discs where the distance between the spots is related to the distance between atomic planes in the specimen. The diffraction pattern is related to the structure of the crystal through the Bragg law

$$n\lambda = 2d\sin\theta_B \quad (3.1)$$

where  $\lambda$  is the wavelength of the incident electrons,  $d$  the distance between atomic planes,  $\theta_B$  is the angle of incidence and  $n$  is an integer describing the order. Constructive interference occurs when the Bragg condition is fulfilled giving rise to the spots or discs observed in a diffraction pattern. The diffraction pattern or the TEM image is then produced on a viewing screen after the diffracted electrons travel through a series of lenses known as the intermediate, projector and magnification lenses. TEM techniques such as Selected area electron diffraction (SAED), HRTEM and analytical techniques such as Z-contrast microscopy, Electron EELS and Energy dispersive X-ray spectroscopy (EDX) are as a consequence of electron scattering. HRTEM, SAED take advantage of elastic scattering to provide information about the crystal structure of the material under study. EELS, Z-contrast electron microscopy and EDX on the other hand use the inelastically scattered electrons to obtain information regarding the chemical and electronic information about the specimen. The theory behind two of these techniques, HRTEM and EELS, which are extensively used in this thesis will be explained in greater details in the following sections.

### 3.1.1 Instrumentation

In this thesis, a Titan 80-300 transmission electron microscope was used both for HRTEM and EELS studies. The microscope was operated at an acceleration voltages of 300 kV for HRTEM imaging and 50 kV and 80 kV for EELS. To record EELS data a GATAN GIF Tridiem spectrometer was used. The energy resolutions obtained for EELS spectra were 0.5 eV for 80 kV and 0.75 eV for 300

kV. The microscope is also equipped with a Cs corrector to correct for spherical aberrations of the objective lens which gives a point-point resolution in HRTEM imaging of 0.08 nm.

## 3.2 Electron Energy Loss Spectroscopy

### 3.2.1 EELS instrumentation

The EELS spectrometer is based on the magnetic prism where the electrons follow a circular path of radius  $R$  and are deflected through an angle. According to Egerton [59] the sideways force on an electron is given by

$$F = Bev = \frac{mv^2}{R} \quad (3.2)$$

where  $e$ ,  $v$ , and  $m$  are the electron speed, charge and relativistic mass respectively. The band radius depends on the velocity and consequently on the energy of the electron

$$R = \left(\frac{m}{e}\right)Bv \quad (3.3)$$

The electron beam emerges from the magnet having been deflected through an angle of  $\phi$ . The angular deflection of an electron depends on its velocity within the field. Electrons which have lost energy in the specimen have a lower value of  $v$  and a smaller  $R$ , so they leave the magnet at larger deflection angle. [59,60]. Figure 3.1 shows the ray diagram of electrons in an EELS spectrometer. Electrons with greater energy loss are deflected further than those suffering zero loss. Electrons of lower energy will follow a path of smaller radius, being focused at a lower point than those with higher energies, thus defining the energy scale. The magnetic prism resembles the bending and dispersion of white light in a glass prism with a difference that the magnetic prism also has a focussing action. If the electron beam originates from a single point, electrons of a given energy are focussed to a single point in the image plane.

### 3.2.2 Inelastic electron scattering

Figure shows the scattering geometry for an electron with an incident energy  $E_0$  and momentum  $k_0$ . While passing through the sample the electron is scattered through an angle  $\theta$  and loses energy  $\Delta E$  or momentum transfer  $q$ . The momentum transfer,  $q$  can be decomposed into components perpendicular  $q_{\perp}$  and parallel  $q_{\parallel}$  to the incident direction. The momentum transfer,  $q$ , is a function of the scattering angle,  $\theta$ , [61–63]. In the experiment the range of incident wavevectors are defined by the convergence semi angle  $\alpha$ . After scattering the range of collected wavevectors will depend on the collection semi-angle  $\beta$

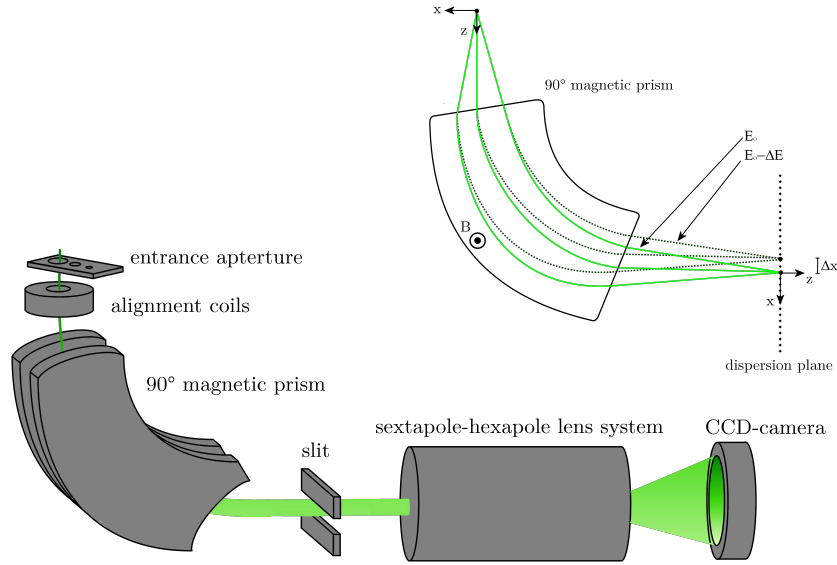


Figure 3.1: Schematic diagram of the EELS spectrometer and the ray diagram for the deflection of electrons in a spectrometer

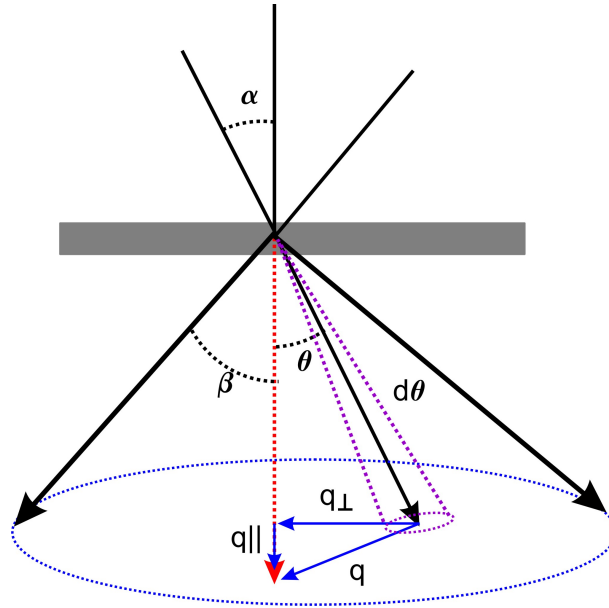


Figure 3.2: Scattering geometry of an electron energy loss experiment . A primary electron of energy  $E_0$  and wave vector  $k$  is inelastically scattered losing energy  $\Delta E$  and undergoing a momentum transfer  $q$ . The scattering angle is  $\Theta$ . The convergence semi angle  $\alpha$  determines the range of incident wave-vectors and the collection angle  $\beta$  determines the range of the collected wavevectors

To describe inelastic scattering of electrons the behaviour of each electron can be specified in terms of transition from an initial state of wavefunction  $\psi_i$  to a final state  $\psi_f$  using first Born approximation, the probability that an electron moving

in a solid with an initial kinetic energy  $E_0$  will be inelastically scattered through a small angle  $\theta$ , losing energy  $\Delta E = \hbar\omega$  and transferring momentum  $\mathbf{p} = \hbar\mathbf{k}$  is given by [60, 64–66]

$$\frac{d\sigma}{d\Omega} = \left(\frac{m_0}{2\pi\hbar^2}\right)^2 \frac{\kappa_f}{\kappa_0} \left| \int V(\mathbf{r}) \psi_0 \psi_i^* \exp(i\mathbf{q}\cdot\mathbf{r}) d\tau \right|^2 \quad (3.4)$$

where  $K_0$  and  $K_f$  are the initial and final wavevectors for the electrons after scattering.  $\hbar\mathbf{q} = \hbar(K_0 - K_f)$  is the momentum transfer. The potential

$$V(\mathbf{r}) = \frac{Ze^2}{4\pi\epsilon_0 r} - \frac{1}{4\pi\epsilon_0} \sum_{j=1}^Z \frac{e^2}{|\mathbf{r} - \mathbf{r}_j|} \quad (3.5)$$

represents the Coulomb attraction by the nucleus charge  $Ze$ , and the repulsion between the electrons in the atom. The nuclear contribution is zero due to the orthogonality between the initial and the final states. Combining equations (3.1) and (3.2) the differential cross section is given in the form

$$\frac{d\sigma}{d\Omega} = \left(\frac{4\gamma^2}{a_0 q^4}\right) \frac{k_1}{k_0} |\epsilon_n(\mathbf{q})|^2 \quad (3.6)$$

The first term represents Rutherford single particle scattering and the second term is called the *dynamical structure factor* which is the absolute value of a transition matrix element

$$\epsilon_n = \int \psi_f^* \sum_j (\exp(i\mathbf{q}\cdot\mathbf{r})) \psi_0 d\tau = \langle \psi_f | \exp(i\mathbf{q}\cdot\mathbf{r}) | \psi_0 \rangle \quad (3.7)$$

The differential cross section can be expressed in terms of the generalized oscillator strength (GOS)

$$f_n(\mathbf{q}) = \frac{E_n}{R} \frac{|\epsilon_n(\mathbf{q})|^2}{(q a_0^2)} \quad (3.8)$$

$R$  is the rydberg energy = 13.6 eV and  $E_n$  is the energy of the transition. The angular and energy dependence of scattering are then specified using a double-differential cross section. The cross section represents the probability of a scattering event and it is a function of electron beam energy and scattering angle it represents the fraction of electrons of primary energy  $E_0$  and momentum  $k_0$  which have been scattered into a solid angle  $d\Theta$  and lost energy  $\Delta E$

$$\frac{d^2\sigma}{d\Omega dE} = \frac{4\gamma^2 R k_1}{E q^2 k_0} \frac{df}{dE}(\mathbf{q}, E) \quad (3.9)$$

The scattering vector  $\mathbf{q}$  is related to the scattering angle  $\Theta$  in the approximation  $\Theta \ll 1$  mrad and  $\Delta E \ll E_0$ . The characteristic angle  $\theta_0$  defines the minimum transfer of momentum for an energy loss  $E$

$$\mathbf{q}^2 = k^2(\theta^2 + \theta_E^2) \quad (3.10)$$

$$\theta_E = \frac{\Delta E}{2E_0} = \frac{\Delta E}{\gamma m_0 v^2} = \frac{\Delta E}{(E_0 + m_0 c^2)(v/c)^2} \quad (3.11)$$

The angular and energy dependence of inelastic scattering is then expressed as

$$\frac{d^2\sigma}{d\Omega dE} = \frac{4\gamma^2 R}{E k_0^2} \left( \frac{1}{\theta^2 + \theta_E^2} \right) \frac{df}{dE} = \frac{8a_0^2 R^2}{E m_0 v^2} \left( \frac{1}{\theta^2 + \theta_E^2} \right) \frac{df}{dE}(q, E) \quad (3.12)$$

where

$$\frac{df}{dE}(q, E) \propto |\langle \psi_f | \exp(i\mathbf{q} \cdot \mathbf{r}) | \psi_i \rangle| \quad (3.13)$$

Core loss excitations in the EELS spectrum arises due to the transition between an initial electronic state  $|\psi_i\rangle$  to an unoccupied electronic state  $\langle \psi_f|$ . The probability for this process is proportional to the density of the unoccupied states. The differential cross section can then be expressed as a transition matrix element  $\langle \psi_f | \exp(i\mathbf{q} \cdot \mathbf{r}) | \psi_i \rangle$  multiplied by a density of states term  $\sum_{i,j} \delta(E + E_i - E_f)$  [67]

$$\frac{d^2\sigma}{d\Omega dE} \propto |\langle \psi_f | \exp(i\mathbf{q} \cdot \mathbf{r}) | \psi_i \rangle|^2 \delta(E + E_i - E_f) \quad (3.14)$$

where  $\psi_i$  and  $\psi_f$  are the initial and the final state of the atomic wave-functions, respectively, and  $E_i$  and  $E_f$  are the corresponding energies of these states(eigen values). For small scattering angles where the momentum transfer  $q \ll 1/r_c$ , with  $r_c$  being the radius of the core wave-function, and demanding orthogonality between the initial  $|\psi_i\rangle$  and final states  $\langle \psi_f|$ , the operator  $\exp(i\mathbf{q} \cdot \mathbf{r})$  can be expanded as

$$\exp(i\mathbf{q} \cdot \mathbf{r}) = 1 + \mathbf{q} \cdot \mathbf{r} - i(\mathbf{q} \cdot \mathbf{r})^2 + \dots, \quad (3.15)$$

This is known as the dipole approximation. For small scattering angles  $\theta$  the observed core transitions satisfy obey the dipole selection rule

$$\Delta l = \pm 1 \quad (3.16)$$

where the change of angular momentum  $\Delta l$  between the initial and final states and  $l = 0, 1, 2, 3$  for  $s, p, d, f$  orbitals respectively.

### 3.2.3 Dielectric formalism of EELS

An alternative way of describing the EELS spectrum is by the use of the dielectric function  $\epsilon(\omega, q)$ . The incident electron polarizes the material thus creating an electric field that acts back on the electron. As the fast electron loses energy in transmission through the specimen its interaction with the specimen, which is represented by the intensity of the measured loss spectrum  $I(E)$ , can be related to the energy loss probability. For interaction with weakly bound valence electrons

including plasmon excitations and inter-band transitions the dynamic structure factor can be expressed in terms of electron momentum dependent electron energy loss function of the dielectric theory. [65, 66, 68]

$$\frac{d^2\sigma}{d\Omega dE} \propto \frac{1}{\theta^2 + \theta_E^2} \text{Im} \frac{-1}{\epsilon(\mathbf{q}, \omega)} \quad (3.17)$$

where  $\epsilon(\mathbf{q}, \omega)$  is the dielectric function. Where the dielectric function is made up of the real and imaginary parts  $\epsilon_1$  and  $\epsilon_2$

$$\epsilon(\mathbf{q}, \omega) = \epsilon_1(\mathbf{q}, \omega) + i\epsilon_2(\mathbf{q}, \omega) \quad (3.18)$$

The real  $\epsilon_1$  and imaginary parts  $\epsilon_2$  of the dielectric function can be obtained by a Kramers-Kronig analysis. The real part of the dielectric function  $\epsilon_1$  measures the polarizability of the material while the imaginary part  $\epsilon_2$  is a description of the absorption process. The imaginary part of the dielectric function is proportional to the joint density of states (JDOS). [68–70]

$$\epsilon_2 E \propto \text{JDOS} \cdot \sum_i |\langle \Psi_f | \exp(i\mathbf{q} \cdot \mathbf{r}) | \Psi_i \rangle| \quad (3.19)$$

The dielectric function may also be expressed in terms of the optical conductivity  $\sigma(\omega)$

$$\epsilon(\omega) = 1 + \frac{4\pi i \sigma(\omega)}{\omega} \quad (3.20)$$

where

$$\sigma(\omega) = \sigma_1(\omega) + i\sigma_2(\omega) \quad (3.21)$$

$\sigma_1(\omega)$  and  $\sigma_2(\omega)$  are the real and imaginary parts of the optical conductivity. The peaks in the optical conductivity spectra are determined by the dipole allowed transitions between the occupied states to the unoccupied states. For isotropic crystals e.g cubic crystal systems the energy loss function does not vary along the various crystal directions. The anisotropy of the dielectric function for anisotropic solids such as monoclinic, tetragonal or orthorhombic crystal systems may be accommodated by allowing the dielectric function to vary with the direction of  $\mathbf{E}$ . For such anisotropic crystals the dielectric function,  $\epsilon_{ij}$ , is a tensor and has a different value with respect to crystallographic orientation. For an orthorhombic system the dielectric tensor is defined in terms of major symmetry directions which are perpendicular to the crystallographic directions.

$$\epsilon_{ij} = \begin{pmatrix} \epsilon_{xx} & 0 & 0 \\ 0 & \epsilon_{yy} & 0 \\ 0 & 0 & \epsilon_{zz} \end{pmatrix} \quad (3.22)$$

The double differential cross section for an anisotropic crystal then becomes

$$\frac{d^2\sigma}{d\Omega dE} \propto \text{Im} \frac{-1}{\epsilon_{xx} + \epsilon_{yy} + \epsilon_{zz}} \quad (3.23)$$

### 3.3 Characteristics of EELS spectra

The EELS spectrum contains information about the elementary excitations in the solid including relativistic losses, phonons, excitons, plasmons, interband, intraband transitions and ionization edges. The spectrum can be divided into two energy regions, the low energy loss regions with energy losses typically  $\Delta E < 50\text{eV}$  and a high energy loss region  $\Delta E > 50\text{eV}$ . The low-loss region is characterized by excitations involving valence electrons while the high-energy region is characterized by excitations involving core-shell electrons.

#### Valence EELS

Spectroscopy of the low loss region is also referred to as VEELS. The VEELS spectra is characterized by peak features involving a number of electronic transitions or excitations [60, 70, 71]

1. Losses due to transitions taking place between the bands can be due to intra-band or interband transitions. Figure 3.3 shows a schematic representation of intra-band and interband transitions in a metal. The intra-band transition (marked by blue arrow 1 in Fig. 3.3) corresponds to the excitation of an electron from below the Fermi level ( $E_F$ ) to another state above the  $E_F$  within the same band. Intra-band transitions are mainly observed in metals and can be neglected in insulating materials. [70, 72]. Inter-band transitions (marked by

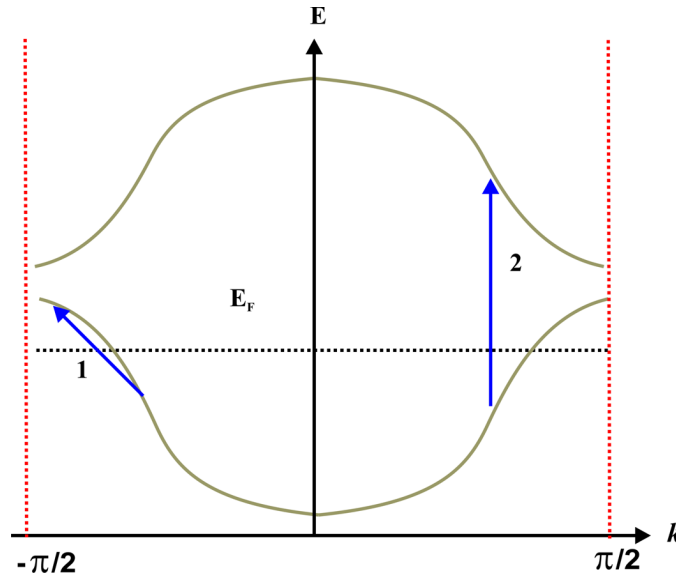


Figure 3.3: A schematic showing the intraband transitions (blue arrow 1) and inter-band transition (blue-arrow 2) in a metal

blue arrow 2 in Fig. 3.3) involve transitions from the valence bands below the  $E_F$  to conduction band above the  $E_F$ . Interband transitions are divided into



direct interband transitions and indirect interband transitions. Direct inter-band transitions involve only excitations as a result of the momentum transfer between the incident electron and the electron in the materials. The indirect interband transitions on the other involve momentum transfer from the incident electron and phonon scattering. Indirect interband transitions are also generally weaker than direct transitions.

2. Losses due to the collective excitation of the valence electrons also known as plasmon losses. Plasmon excitation occurs due to the fact that conduction electrons in metals and valence electrons in insulators and semi-conductors are weakly bound to the atom. These electrons are however coupled to each other by electrostatic forces and their electronic states are delocalized in form of energy bands. In the case of a fast-moving electron through the solid the atomic electrons are displaced by the Coulomb potential repulsion forming a region of positive potential behind the electron resulting in regions of positive and negative space charge behind the electron. The backward pull of the positive region on the electron causes the electron to lose energy. This process can be viewed as creation of pseudo-particles known as plasmons each carrying a quantum of energy equal to  $E_p = (\hbar/2\pi)\omega_p$  [59]. Plasmonic losses include the surface and volume plasmons. In a sample of finite thickness, excitation of surface modes, also known as surface plasmons may take place. The differential cross section for surface plasmon excitation is given by [73]

$$\frac{d^2\sigma}{d\Omega dE} \propto \frac{k_x}{q^4} \text{Im} \frac{(\epsilon - \epsilon_0)^2}{\epsilon_0 \epsilon (1 + \epsilon)} \quad (3.24)$$

where  $k_x = k_0 \theta$  is the wave vector parallel to the surface,  $\epsilon$  is the material dielectric function and  $\epsilon_0$  is the permittivity. For the condition  $\epsilon_0 = 1$  which is the vacuum the free electron value of the surface plasmon is given by  $\hbar\omega_p / ((2)^{1/2})$ . The contributions from surface losses are more relevant to the thin samples typically  $t < 20$  nm [59].

The position of the volume plasmon peak can be approximated in the free electron model using the Drude [72, 74, 75] formula or the Horie formula for insulators [56, 69]. The Drude formula is given by

$$\hbar\omega_f = \hbar \left( \frac{ne^2}{\epsilon_0 m} \right)^{\frac{1}{2}} \quad (3.25)$$

Where  $\hbar$  is the planck's constant,  $n$  is the density of the valence electrons,  $\epsilon_0$  is the permittivity of the vacuum and  $m$  is the mass of an electron. Eq. is mainly used for free electrons especially in metals, for semi-conductors and solids where the valence electrons are more bound the plasmon peak is given by the Horie formula

$$E_p = \hbar\omega_p = [(\hbar\omega_f)^2 + E_g^2]^{0.5} \quad (3.26)$$

where  $E_g$  is the band gap. The changes in plasmon energy with momentum transfer is known as the plasmon dispersion and is given by [73].

$$E_p(q) = E_p(0) + \frac{\hbar}{m} \alpha q^2 \quad (3.27)$$

where the  $\alpha$  is the dispersion factor.

3. Relativistic losses can occur when the velocity of the electron in the sample is higher than the velocity of light in vacuum. Relativistic losses especially semiconductors and insulators can lead to signal between the band-gap and inter-band region in EELS spectrum [71,76,77]. The conditions for Cerenkov losses are fulfilled in  $v > \frac{c_0}{n}$ . Where  $c_0$  is the velocity of light,  $v$  velocity of the electron and  $n$  is the refractive index of the material. One of the ways to reduce the effects of Cerenkov losses is to reduce the acceleration voltage in the microscope. Relativistic velocity of electron  $v$  is given by [57]

$$v = \frac{h}{\sqrt{2m_0 E (1 + \frac{e}{2m_0 e^2} E)}} \quad (3.28)$$

where  $h$  is the planck's constant,  $e$  is the electron charge and  $E$  is the acceleration voltage. The Cerenkov modes have a dispersion given by  $\omega = cq/n$

### Core-loss EELS spectra

Core loss spectra involves electronic transition from the core-shell to the conduction band. These transitions then appear as peaks in the spectra which are known as the ionization edges. The position of the ionization edges is specific to each element and is used often used as a means of identifying elements. Other than the position of the ionization edge the fine structure of the peak is also very sensitive to the local bonding environment. The fine structure of the ionization edges is known as energy loss near edge structures (ELNES) and is used to study bonding and local atomic structure. The ionization threshold energies observed in this thesis for various core-edges represent the energy difference between the core initial state and the lowest final state of an excited core-electron. In many case for a particular atomic specis, the peak position energy can change due to changes due to changes in the oxidation states of the atoms. This is known as a *peak shift* or a *chemical shift*. The core-level binding energy is defined by Martneson et al as the total energy difference between an ionized ( $N - 1$  electron) final state system and the initial ( $N$  electron) system [78]. The chemical shift between two systems A and B, is then expressed as

$$\Delta E = E_{ion,A}(N-1) - E_{ground,A}(N) - (E_{ion,B}(N-1) - E_{ground,B}(N-1)) \quad (3.29)$$

The shift is thus determined by two total energy differences, one relating to the initial states and one relating to the final states.

### 3.3.1 Spectra acquisition and analysis

#### Spectra acquisition

Errors and uncertainties in the analysis of the EELS spectrum arise mainly due to the instability of the primary electrons used in the TEM instruments. Under ideal conditions, the beam current should not vary during the experiment. However, in actual experiments the stability of the electron gun and the accelerating voltage is usually varying. An important parameter in EELS is the width of the zero-loss peak, which defines the resolving power of the utilized spectrometer also known as the energy resolution. The energy resolution limits the details which are can be resolved in an energy loss spectrum. This is usually determined from the Full Width at Half Maximum (FWHM) of the zero-loss peak. Figure 3.4(a) shows the variation in the energy resolution of the zero-loss peak with time. One can see that the energy resolution is particularly stable at approximately 0.55 eV( $\pm 0.03$ ). Instabilities in the high tension (accelerating voltage) of the microscope also lead to energy drifts where the position of the peaks changes with time. It is necessary to study the extent of the energy drift in the case where chemical shifts of the ionization edges are to be observed. This is shown in Figure 3.4(b). A continuous energy drift of  $\pm 0.1$  eV/min is observed. This means the inaccuracy of the peak positions is increases by a value of  $\pm 0.1$  eV per minute of acquisition time. Analysis of chemical shifts is liable to uncertainties arising from the measurement of absolute positions of EELS core-loss edges in a TEM due to instability of the energy of the incident electrons. These instability originates from a continuous drift and random ripple of the high tension and are sometimes unavoidable. In our case the energy drift was kept at a minimum as shown here.

### 3.3.2 Spectrum analysis

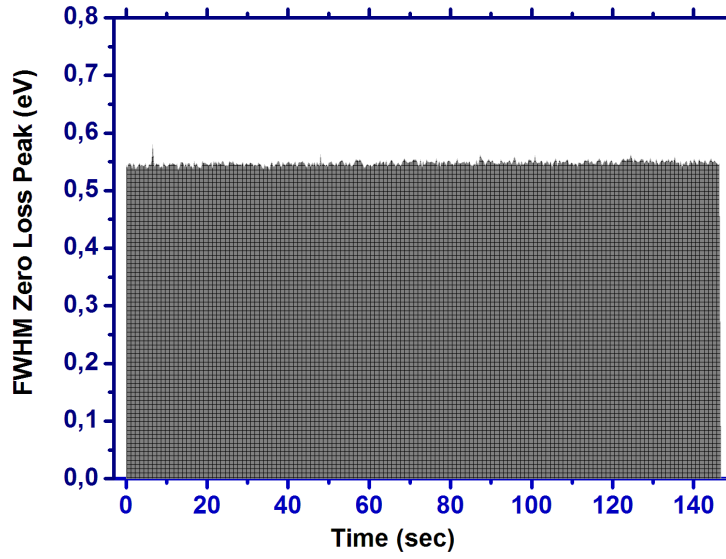
In order to extract either qualitative or quantitative data, the acquired EELS spectrum needs to be processed. The effects of multiple-scattering and the background need to be deconvoluted before conclusions can be derived from the spectra [60,79].

#### Subtracting the Background

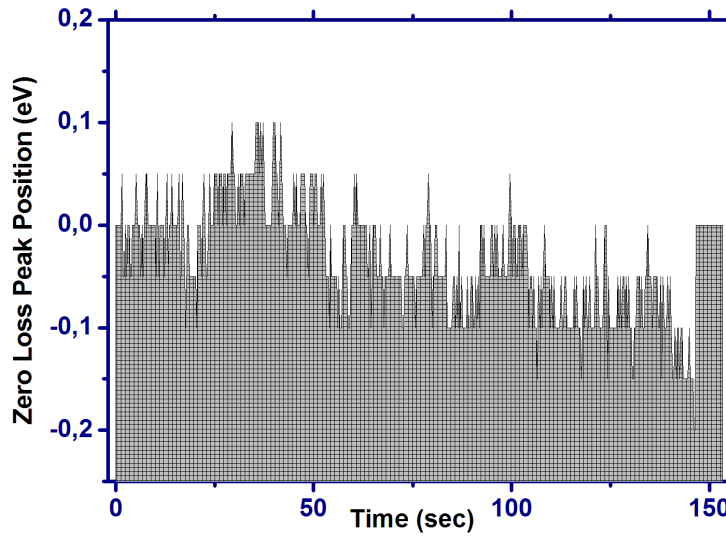
All core-loss edges lie on a monotonically decreasing background. This background originates from excitations of electrons with lower binding energy and the tails of plasmons and other core-loss edges. For better quantification of the elemental composition of the sample, but also for a clearer identification of onset energies, it is preferable to remove these contributions. The most common way is to fit the background with a power-law function [60]

$$B(E) = A \cdot E^{-d} \quad (3.30)$$

and subtract it from the experimental spectrum. The coefficient  $A$  can vary strongly, depending i.e. on beam current or exposure time. The exponent  $d$



(a) Variations in the Energy resolution of the Zero Loss peak. The variation are derived from the FWHM of the zero loss peak.



(b) Energy drift of the electron beam along the elapsed time.

*Figure 3.4: Energy and position drift of the Zero Loss Peak*

increases with increasing energy loss, but decreases with increasing sample thickness\* and collection angle. Its value usually lies between 2-6 [60]. These dependencies require the background to be fitted at each core-loss edge separately. The

---

\*Because of increasing multiple scattering contribution.

parameters are determined by fitting to a small region preceding the edge onset, with the assumption that the background intensity has the same energy dependence over the entire core-loss edge energy range. Within this region the spectrum is converted to a  $\log(E)$ ,  $\log(I)$  scale and the parameters are fitted to a straight line using least-square fitting. For good results it is beneficial to make the fitting region as wide as possible and as close as possible to the edge onset. Main downside to this method is the fact, that there is very little physical justification for the power-law dependence of the background [80]. For elemental composition analysis, where absolute intensities are of importance, the background removal is the most limiting factor of the accuracy. For determining onset energy, the removal should not impose any problems, if done carefully.

### Removal of Multiple inelastic Scattering

The theoretical descriptions of spectra in the previous section only covers scattering from single atoms and single scattering. The intensity distribution recorded in a real energy-loss spectrum is, however, the result of single and multiple scattering. This means, that double or triple plasmon excitations and even inner-shell ionizations are likely to happen. Multiple scattering makes the interpretation of spectra difficult. For example, multiple plasmon peaks can overlap with low-energy core edges obscuring the features in the spectrum. Removal of multiple scattering effects from the energy-loss spectrum is possible and two methods, based on Fourier transformation, exist. They are known as *Fourier-Log* and *Fourier-Ratio deconvolution*.

Fourier-log method is used to remove multiple scattering effects in the low loss electron spectrum. In Fourier-log deconvolution it is assumed that that inelastic scattering events are independent and that the probability  $P_n$  of  $n$  such scattering events follows a Poisson distribution. The probability is defined as the ratio of the intensity  $I_n$  of  $n$ -fold scattering integrated over a specific energy range, divided by the total integrated intensity  $I_t$  and given by [79]

$$P_n = \frac{I_n}{I_t} = \frac{1}{n!} \left( \frac{t}{\lambda} \right)^n e^{-t/\lambda} \quad (3.31)$$

where  $t$  is the sample thickness and  $\lambda$  the mean free path of all inelastic scattering events in the energy range of  $I_n$ . The single scattering distribution  $S(E)$  is related to by

$$\int S(E) dE = I_{n=1} = I_t P_{n=1} \quad (3.32)$$

This distribution does not account for the finite energy resolution  $\Delta E$  of the instrumentation. The actual recorded single scattering distribution  $J^1(E)$  is a convolution of the  $S(E)$  with an instrument response function  $R(E) = Z(E)/I_0$

$$J^1(E) = \int_{-\infty}^{\infty} R(E - E') S(E') dE' = R(E) \otimes S(E) \quad (3.33)$$

where  $Z(E)$  represents the zero-loss peak of the energy-loss spectrum.  $R(E)$  is a function with unit area and a FWHM equal to  $\Delta E$ . The recorded double scattering distribution  $D(E)$  is

$$J^2(E) = R(E) \otimes D(E) = R(E) \otimes S(E) \otimes S(E) \cdot \frac{1}{2!I_0} \quad (3.34)$$

In this context, the intensity distribution  $J(E)$  of the recorded energy-loss spectrum can be expressed as superposition of single and multiple scattering distributions

$$\begin{aligned} J(E) &= Z(E) + J^1(E) + J^2(E) + J^3(E) + \dots \\ &= R(E) \otimes (I_0\delta(E) + S(E) + D(E) + \dots) \end{aligned} \quad (3.35)$$

By taking Fourier-transforms the convolution becomes a product and the equation can be rearranged to give the Fourier-transform of the single scattering distribution

$$\text{FT}[S(E)] = I_0 \ln \frac{\text{FT}[J(E)]}{\text{FT}[Z(E)]} \quad (3.36)$$

An inverse Fourier-transform then leads to the single scattering distribution. The problem with equation is the so-called noise amplification. At high frequencies  $\text{FT}[J(E)]$  is usually dominated by noise and division by  $\text{FT}[Z(E)]$  increases this high-frequency noise content. This limits the method to the deconvolution of single scattering distribution, broadened by instrumentation. Some variations to this methods have been developed in order to reduce this noise-amplification, i.e.: multiplication with a reconvolution function or replacing the zero-loss peak with a delta function. The performance of *Fourier-Log deconvolution*, as well as that of *Fourier-Ratio deconvolution*, strongly depends on the implementation on a computer. For example, the use of discrete Fourier-transformations can cause artifacts.

The *Fourier-log* method needs spectra that include a zero-loss peak and therefore mostly applied to so-called low-loss spectra. It can be used to remove plural scattering from core-loss edges, but for this spectra with a very high energy range have to recorded. Core edges in such low dispersion spectra suffer from strong noise, which makes *Fourier-Ratio deconvolution* a more feasible choice. Fourier-ratio method is used to remove multiple scattering effects in the core-losses. This method treats a recorded core-loss spectrum as a convolution of the low-loss spectrum and the ideal single scattering core-loss spectrum.

$$\text{FT}[S_{\text{core-loss}}(E)] = I_0 \text{FT} \left[ \frac{\text{FT}[J_{\text{core-loss}}(E)]}{\text{FT}[J_{\text{low-loss}}(E)]} \right] \quad (3.37)$$

*Fourier-Ratio deconvolution* is limited by the same effects as the *Fourier-Log deconvolution*. Because of the enormous differences of the intensities in a low- and core-loss spectrum, the two needed spectra have to be recorded at very different exposure times.

### Kramers-Kronig Analysis

Having corrected the acquired EELS spectra for multiple scattering as outlined in the previous section, a single scattering spectrum,  $S(E)$ , is obtained. Kramers-Kronig analysis (KKA) analysis of the  $S(E)$  is then done to derive the dielectric function and other optical parameters. [60, 66, 81].

$$\text{Re}\left(\frac{-1}{\epsilon(\omega)}\right) = 1 - \frac{2}{\pi} P \int_0^\infty \text{Im}\left(\frac{-1}{\epsilon(\omega')}\right) \frac{\omega' d\omega'}{\omega'^2 - \omega^2} \quad (3.38)$$

where  $P$  is the cauchy value of the integral. To apply this equation it necessary to know the absolute value of the energy loss function. In experiments the energy loss spectra are measured in an arbitrary scale and it is therefore necessary to introduce an independent, known parameter for the material at some energy in order to normalize the results at all other energies. For this purpose, the value of  $\text{Re}(\frac{1}{\epsilon}(\omega))$  at zero frequency is most convenient parameter. For insulators the  $\text{Re}(\frac{1}{\epsilon}(0))$  is the refractive index  $n$  [81, 82].

## 3.4 High resolution electron microscopy

Contrary to EELS, HRTEM makes use of the elastically diffracted electrons to give information mainly about the atomic and crystal structure of the sample under study. During HRTEM image formation at least one diffracted beam has to diffract constructively with a transmitted beam. However a direct interpretation of the obtained experimental HRTEM images is usually hard. This is mainly due to two reasons

- Strong interactions between the electrons of the incoming electron wave with the Coulomb potentials of the atoms often leads to multiple scattering.
- Aberrations in the microscope, the most important of which are the spherical and chromatic aberrations. The spherical aberration blurs the image since rays that travel far from the optic axis are focused more strongly than those close to the axis. The chromatic aberration again blurs the image because electrons with slightly different wavelengths (energy) are focused more or less strongly [56]. These aberrations are characterized by two coefficients, the spherical aberration coefficient  $C_s$  and the chromatic aberration coefficient,  $C_c$ .

As such HRTEM image simulations are often necessary in order to interpret experimental HRTEM images.

### 3.4.1 Image formation in HRTEM

The image formation process in HRTEM is shown schematically in Figure 3.5.

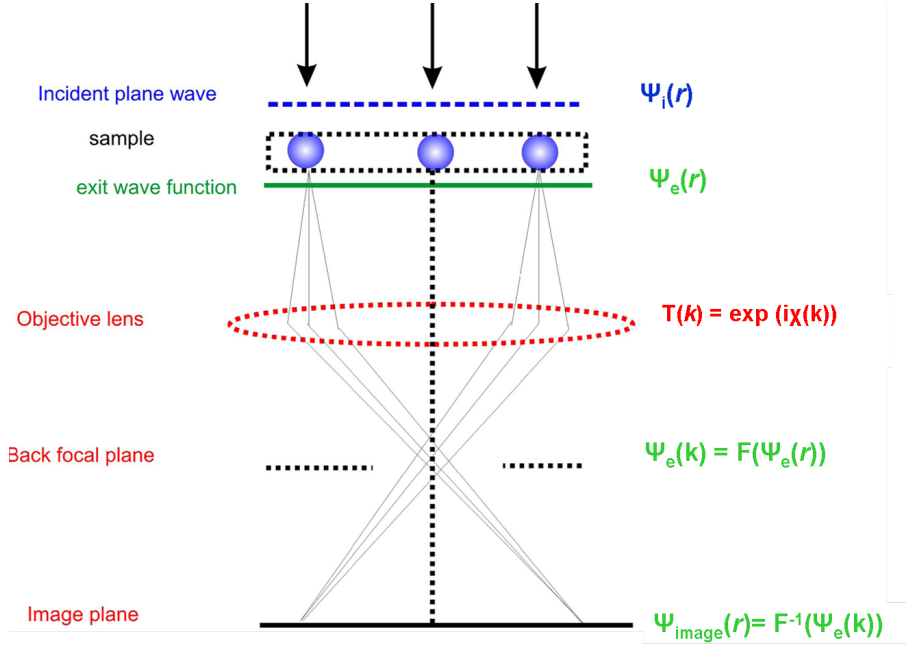


**Figure 3.5:** Schematic illustration of the HRTEM image formation process. The incident electron wave  $\Psi_i(r)$  is dynamically scattered in the specimen. The exit-plane wave  $\Psi_e(k)$  contains the structural information. The wavefunction at the image plane  $\Psi_{image}(r)$  is modified by the instrument properties including the lens aberrations

The incident electrons are described by a plane wave

$$\Psi_i(\mathbf{r}) = \Psi_0 \exp(2\pi i(\mathbf{k} \cdot \mathbf{r})) \quad (3.39)$$

On reaching the specimen the electron beam is either inelastically or elastically scattered due to interaction with the electrostatic crystal potential. The wave exiting the specimen is known as the exit wave represented by

$$\psi_e(\mathbf{r}) = \psi_i(x, y)Q(x, y) \quad (3.40)$$

Where  $Q(x, y)$  is a function representing the interaction parameter with the atomic potential of the material. The exit wave function  $\psi_e(\mathbf{r})$  undergoes a Fourier transformation by travelling through the objective lens and a diffraction pattern is formed at the back focal plane of the objective lens. The intensity at the image plane is given by the modulus of the wavefunction at the image plane  $\Psi_e(\mathbf{R})$ . The process of image formation can therefore be described mainly by two interactions.

- Interaction of the incident plane wave with the crystal potential of the sample
- Interaction between the exit wave function with the microscope. Especially the effects of the objective lens characteristics on the exit wave function.



### 3.4.2 Interaction with the crystal potential

The interaction between the incident plane wave and the crystal was represented by a function  $Q(x, y)$ . This function is given by [58]

$$Q(x, y) = A(x, y) \exp(i\phi(x, y)) \quad (3.41)$$

Where  $A(x, y)$  is the aperture function and  $\phi(x, y)$  is the phase which depends on the thickness of the sample. The phase change depends on the crystal potential  $V(x, y, z)$  that the electron sees as it travels through the crystal. Assuming a thin specimen the projected potential is then given by

$$V_t(x, y) = \int_0^t V(x, y, z) \quad (3.42)$$

The interaction between the incident wave and the crystal is then given by

$$Q(x, y) = \exp[-i\sigma V_t(x, y) - \mu(x, y)] \quad (3.43)$$

Where  $\mu$  is an interaction constant and  $\mu(x, y)$  is the absorption. Thus the overall effect of the specimen on the electron beam is represented by a phase shift  $\mu$  proportional to the projection of the potential distribution of the specimen on to a two-dimensional plane. This is known as the phase-object- approximation. For the case where  $V_t(x, y) \ll 1$  expanding  $Q(x, y)$  and neglecting absorption and the higher terms gives

$$Q(x, y) = 1 + i\sigma V_t(x, y) \quad (3.44)$$

This approximation is known as the weak-phase-approximation(WPOA). The WPOA states that for very thin specimens the amplitude of the transmitted wave function is linearly related to the projected potential of the specimen.

### 3.4.3 Interaction with the microscope - Transfer function

The electron microscope is not a perfect imaging device. On passing through the objective lens, the electron wave undergoes a phase shift and an amplitude reduction [83]. In addition the electron beam is also modified by the instrumental and electronic instabilities. The most important interaction is the interaction of the electron beam with the objective lens. This interaction is represented by a transfer function given as

$$T(k, \delta F) = \exp(i\chi(k)) \quad (3.45)$$

The function  $T(k, \delta F)$  is also known as the contrast transfer function (CTF) where  $\delta F$  is the defocus and  $\chi(k)$  is the phase change. The phase change is given by

$$\chi(k) = \pi \delta f \lambda |k|^2 + \frac{1}{2} \pi C_s \lambda^3 |k|^4 \quad (3.46)$$

where  $\delta F$  is the defocus,  $\lambda$  is the wavelength,  $C_s$  is the spherical aberration coefficient. The CTF determines how much of the spatial frequencies  $k$  are transmitted and ultimately the resolution of atomic spacing on the image. The resolution of the electron microscope corresponds to the highest spatial frequency that is transferred into the image intensity spectrum with the same sign as all lower contributing frequencies [84]. Sherzer found an optimum defocus condition to give maximum resolution [85]

$$D_s = 0.67 C_s^{(1/4)} \lambda^{(3/4)} \quad (3.47)$$

There are two resolution limits which can be used to describe an electron microscope. The first is known as the point-resolution of the instrument. This is determined by the first zero crossing of the contrast transfer function at the Scherzer focus. The point resolution is mainly limited by the spherical aberrations of the microscope. As given in Eq (3.45), the point resolution can be improved by reducing the value of the  $C_s$  or reducing the wavelength  $\lambda$ . In a TEM decreasing wavelength means increasing the accelerating voltage of the microscope. Increasing the accelerating voltage means increasing the kinetic energy of the incident electrons which leads to a large increase on the damage done to the sample by the electron beam. In the last ten years it has become possible to correct for the spherical aberrations in the TEM. Recent breakthroughs have led to the development of lenses which cancel the effects of the spherical aberrations [86]. This is done by using non-spherical lenses to generate a negative  $C_s$  value that cancel the positive  $C_s$  value of the objective lens. Using this correction, the resolution of an aberration corrected microscope is increased to sub-angstrom values. The typical resolutions of  $C_s$  corrected microscopes is in the range of 0.05-0.08 nm.

The second resolution specification for an instrument is known as the information-resolution limit. It is determined by electronic and instrument instabilities. The information limit is the highest spatial frequency that can be transferred by a microscope. For a thin specimen, this limit is mainly determined by the envelope of chromatic aberration  $C_c$  (temporal incoherence) and beam convergence (spatial incoherence) [83, 87]. The effective transfer function  $T_{eff}$  is then given by [58]

$$T_{eff}(k) = T(k) E_s E_c E_d E_D E_v \quad (3.48)$$

Where  $E_s$  is the envelope function due to angular spread of the electron source,  $E_c$  is the envelope function due to chromatic aberrations,  $E_d$  is the envelope function due to specimen drift,  $E_a$  is the envelope function due to the detector and  $E_v$  is the envelope function due to vibrations. New generation of microscopes will seek to correct for some of these aberrations in order to improve the information limit obtainable in a microscope.

### 3.4.4 Geometrical phase analysis of HRTEM images

As shown in the previous section under ideal conditions HRTEM represents a two-dimensional (2D) projection of the crystal structure. The atomic planes in

the real crystal are observed as a 2D projection HRTEM image. The spatial frequencies in the HRTEM image correspond to the inter-planar distances in the real crystal. Structural changes in a lattice structure will lead to changes in the HRTEM image and this can be analyzed by studying the spatial variations. This section gives a short introduction to the analysis of HRTEM images using the Geometrical Phase (GPA) method. Working in the reciprocal space the GPA method maps lattice structural variations as 2-Dimensional strain maps that show how the lattice spacings are changing within a structure [88–90]. A HRTEM image can be expressed as a fourier sum of reciprocal lattice vectors  $g$ .

$$I(\mathbf{r}) = \sum_g \exp(2\pi i \mathbf{g} \cdot \mathbf{r}) \quad (3.49)$$

Where  $I_g$  represents the fourier components, and  $\mathbf{r}$  the position. Allowing the fourier components to represent the local intensity and periodicity,

$$I_g = A_g \exp(iP_g) \quad (3.50)$$

$A_g$  is the amplitude of a set of lattice fringes and  $P_g$  is the phase which represents the position of the lattice fringes. For a set of lattice reciprocal vectors  $g_1, g_2$ , lattice displacements within the crystal can be represented using the displacement vector field  $\mathbf{u}(\mathbf{r})$ , which is then related to the phase of the lattice periodicities through

$$P_{g_1(\mathbf{r})} = -2\pi g_1 \mathbf{u}(\mathbf{r}) \quad (3.51)$$

$$P_{g_2(\mathbf{r})} = -2\pi g_2 \mathbf{u}(\mathbf{r}) \quad (3.52)$$

decomposing the reciprocal lattice vectors  $g_1, g_2$  and the displacement vector field  $\mathbf{u}(\mathbf{r})$  into their vectorial components the phase can be expressed as

$$P_{g_1(\mathbf{r})} = 2\pi(g_{1x}u_x(\mathbf{r}) + g_{1y}u_y(\mathbf{r})) \quad (3.53)$$

$$P_{g_2(\mathbf{r})} = 2\pi(g_{2x}u_x(\mathbf{r}) + g_{2y}u_y(\mathbf{r})) \quad (3.54)$$

or in matrix form:

$$\begin{pmatrix} P_{g_1(\mathbf{r})} \\ P_{g_2(\mathbf{r})} \end{pmatrix} = 2\pi \begin{pmatrix} g_{1x} & g_{1y} \\ g_{2x} & g_{2y} \end{pmatrix} \begin{pmatrix} u_x \\ u_y \end{pmatrix} \quad (3.55)$$

The local lattice displacements are then calculated by taking the inverse of the matrix

$$\begin{pmatrix} u_x \\ u_y \end{pmatrix} = -\frac{1}{2\pi} \begin{pmatrix} g_{1x} & g_{1y} \\ g_{2x} & g_{2y} \end{pmatrix} \begin{pmatrix} P_{g_1(\mathbf{r})} \\ P_{g_2(\mathbf{r})} \end{pmatrix} \quad (3.56)$$

The strain maps showing are then calculated from the derivative of the displacement field.

$$\epsilon = \begin{pmatrix} \frac{\partial u_x}{\partial x} & \frac{\partial u_x}{\partial y} \\ \frac{\partial u_y}{\partial x} & \frac{\partial u_y}{\partial y} \end{pmatrix} = \begin{pmatrix} \epsilon_{xx} & \epsilon_{xy} \\ \epsilon_{yx} & \epsilon_{yy} \end{pmatrix} \quad (3.57)$$

In the elastic tensor the  $\epsilon_{xx}$ ,  $\epsilon_{yy}$  are strains representing the variations in the lattice parameters in the x and y direction respectively and  $\epsilon_{xy}$ , represents the shear strain. Using the elastic tensor the volumetric changes can be expressed as the trace of the elastic tensor, i.e the sum of the diagonal elements of the crystal.

$$\Delta V = \epsilon_{xx} + \epsilon_{yy} + \epsilon_{zz} \quad (3.58)$$

Since a HRTEM image is two dimensional, the strain maps can only show the in-plane lattice variations in structure that is lattice variations in the x direction  $\epsilon_{xx}$  and y direction  $\epsilon_{yy}$  and the rotation of the lattice,  $\epsilon_{yx}$ . Central to this technique is the choice of a lattice to be used as a reference for the strain calculations. This involves selecting a group of reflections from the Fast Fourier transform (FFT) of a HRTEM and using Gaussian masks to isolate the reflections and reduce the influence from other reflections. A Schematic diagram of the digital procedure for retrieving the phase and lattice information from HRTEM lattice is show in Figure 3.6. The first step involves the calculation of the FFT spectrum for a HRTEM image which gives a pattern of reflections  $g_i$  representing the HRTEM lattice fringes. Each lattice fringe in turn represents a Bragg plane in the crystal and is characterized by an amplitude  $A$  representing the intensity, and the phase  $P$  giving information about the position of the lattice fringes. In a crystal structure without any structural changes, the phase corresponding to any reciprocal lattice vector  $g$  will be a constant  $P_{gi}$ . Structural changes within the crystal will cause variation in the lattice distances and consequently introducing a phase shift. The gradient of the lattice displacement field  $u(r)$  then gives the variations in lattice spacing along the x and y directions. The accuracy of this technique has been estimated to be in the picometer range [91] and a spatial resolution of 0.03nm. To improve the accuracy of this technique samples with large amorphous layers have to be avoided. The accuracy of this technique is also affected by the distortions and aberration arising from the objective lens. This present work was conducted on a spherical aberration corrected Titan 80-300 kV microscope and therefore the inaccuracies arising from the aberrations have been minimized.

### 3.5 X-Ray diffraction methods

In this thesis powder XRD techniques were applied mainly as a means of phase analysis. XRD is a bulk analytical technique which provides crystal-averaged information about a material's structure. Together with the TEM techniques a general and locally sensitive information can be obtained. The theory behind diffraction

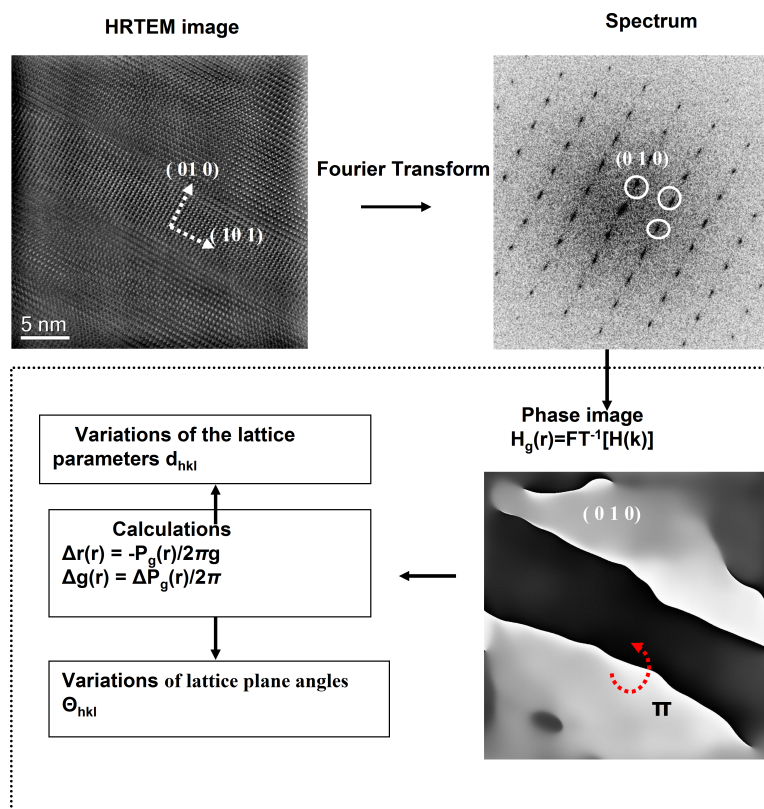


Figure 3.6: A schematic showing the steps in the geometrical phase analysis of a HRTEM image.

pattern formation in XRD is the same as for electron diffraction. The diffraction pattern is displayed as pattern of intensities versus Bragg-angles, Bragg-angles indicate the planes in which Bragg diffraction condition occurs. The measurement geometry used is known as the Bragg-Brentano geometry as shown in Figure 3.7 which features a specimen moving in a circle from  $\theta$  to  $2\theta$  in relation to a detector. An advantage of the geometry consists in the ease of its practical realisation when the diffraction pattern is registered sequentially from one angle to another. In the Bragg-Brentano geometry the X-ray source and the detector are always situated on the same circle. The sample surface is tangential to the centre of the circle and touches the geometrical diffractometer axis. At the same time the flat sample surface is always tangential to the focusing circle which contains the X-ray source and the receiving slits of the detector. For XRD  $\text{Li}_{(1-x)}\text{FePO}_4$  powder samples were spread over the sample holder and pressed in order to give an approximately flat surface. They were then examined using a Siemens D5000 x-ray equipment equipped with a graphite monochromator. The parameters used in XRD are given in Table 3.1. Phase analysis and Rietveld refinements were done using General Structure Analysis System (GSAS) [92]

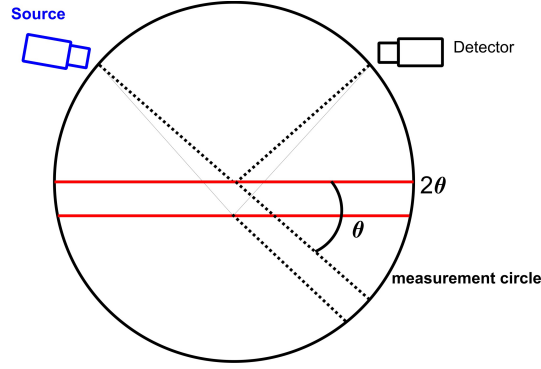


Figure 3.7: Bragg-Brentano geometry in the acquisition of X-Ray diffraction spectrum

Instrument	Siemens D5000
Radiation	CuK $\alpha$
Primary radius	217mm
Receiving slit width	0.6 mm
Primary soller	2.3°
Secondary soller	2.3°
$\lambda$ Discrimination	Graphite monochromator
Scan range	15° to 75°
Step	0.04°
Time (seconds)	5

Table 3.1: Instrumental Parameters for XRD measurements

### 3.6 TEM sample preparation

In this thesis both powder samples and single crystal samples were investigated. It is necessary to prepare samples before a sample can be investigated in the TEM. This is because TEM samples are required to be very thin and free of contamination. Powder samples for the TEM were suspended in ethanol and then spread over a 3 mm carbon grid for TEM investigations. For very big particles, the particles were first ground with a mortar and pestle then subjected to an ultrasonic bath for about 15 minutes and then spread over a carbon grid. Preparation of single crystal samples was done according to the scheme shown in Figure 3.8. In a first step, LiFePO<sub>4</sub> crystals are cut into small strips of 2mm width. Afterwards, these strips were glued together. For this process a highly dispersed epoxy-glue is used in order to form a thin gap of glue. The strips were then mechanically grinded to be plan-parallel and polished to a thickness of approximately 100  $\mu\text{m}$

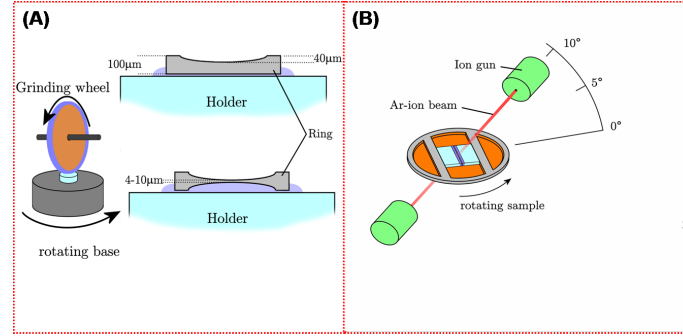


**Figure 3.8:** Preparation of single crystal  $\text{LiFePO}_4$  samples (a) The thin strips of  $\text{LiFePO}_4$  are mechanical grinded until they are  $\approx 10\text{-}30\mu$  thin (b) The thin samples are then ion milled until a hole is formed in the centre of the samples. The regions near the hole are thin enough for TEM investigations

to 130  $\mu$ . Afterwards the specimens were dimpled from both sides to a thickness of approximately 35  $\mu\text{m}$ . Finally, ion-thinning of the specimens was performed from both sides using high-energy  $\text{Ar}^+$  ions until a hole in the specimen could be observed by simultaneous observation using light microscopy as shown in figure. Ion-thinning was performed with ion-beam energies of 3.4 keV under illumination angles of  $6^\circ$  with respect to the specimen surface. At the edges of the formed hole, the specimen is normally thin enough for TEM investigations.





## Theoretical methods

Bandstructure calculations and theoretical spectra have been extensively used to interpret and understand the obtained experimental data. This is particularly the case for EELS spectra where theoretical spectra have been calculated using DFT or crystal field-ligand field methods. These theoretical techniques are introduced in greater details in Sec.4.1. It is also necessary to test parameters used in theoretical models in order to obtain physically meaningful results. The most important parameters used in the DFT spectra calculations are given in Sec.4.2.

### 4.1 Calculating EELS Spectra

As indicated in Sec. 3.2 EELS techniques probe both the joint density of states (JDOS) and partial density of states(PDOS)(or angular momentum projected density of unoccupied states ). The density of occupied and unoccupied states can be calculated using density functional theory and the transition matrix also calculated in order to calculate spectra. In core loss EELS it is assumed that a single electron is excited from a core state to an empty state. In this single-particle excitation model it is assumed that all other electrons do not influence the excitation process and as such the double differential equation is simplified to a density of unoccupied states, multiplied by a transition matrix element. This single-particle picture fails however to describe spectra and properties of transition metal compounds. This is because the electronic correlations which are ignored in the single particle picture play a very important role in determining the electronic structure of transition metal compounds. Therefore the theoretical description of experimental spectra for transition metal compounds also requires a knowledge of the

electron-electron interactions and the effects of the core-holes on the spectra. Single particle DOS methods therefore are able to describe the spectra where electron-electron correlation do not play a big role such as the K-edges. The K-edge arises from  $1s \rightarrow 2p$  transitions. However, the single particle DOS approaches fail to describe the  $L_{2,3}$  edge spectra of 3d transition metals and their compounds. Atomic multiplet calculations can be done in order to calculate the  $L_{2,3}$  spectra. The multiplet theory treats spin-orbit, Coulomb, and exchange interactions which is essential in describing spectra in correlated materials.

There are therefore two different approaches used in this thesis in order to calculate theoretical spectra.

- The single-particle excitation model for the Fe and O K-edges ( $1s \rightarrow 2p$ ) excitation. This is done through density functional methods
- The charge transfer multiplet model for the metal  $L_{2,3}$  ( $2p \rightarrow 3d$ ) and  $M_{2,3}$  ( $1s \rightarrow 2p$ ) edges.

#### 4.1.1 Density Functional Theory Methods

The behaviour of a system of  $N$  electrons can be predicted by solving the Schrödinger equation for the system

$$H\Psi = E\Psi \quad (4.1)$$

$\Psi$  is the many-body wavefunction of the electrons co-ordinates  $\{r_i : i = 1, N\}$  and the Hamiltonian,  $H$  is given by:

$$H = -\frac{\hbar}{2m} \sum_i \Delta_{r_i}^2 + V_{\text{ext}}(r_i) + V_{e-e}(r_i) \quad (4.2)$$

$V_{\text{ext}}$  is the external potential which describes the Coulomb interaction between the electrons and a given configuration of the nuclei. The term  $V_{e-e}$  gives the electron-electron Coulomb interaction and introduces the coupling between the electronic states and makes it difficult to solve the many wavefunction problem. This electron-electron coupling is also known as correlation, as the electron moves the other electrons feel its Coulomb potential, experience a force and move in response. The motion of the electrons is hence said to be correlated. This makes the solution of a many body problem very difficult. Hohenberg, Kohn and Sham made a contribution towards the solution of this problems [93, 94]. Hohenberg and Kohn introduced the concept of the electronic density  $n(\mathbf{r})$  as a basic variable and showed that the total ground state energy could be written as a functional for the ground-state electronic density. The density functional method states that the total energy of a non polarized system of interacting electrons in an external potential is given as a functional of the ground state electronic density,  $\rho$

$$E[\rho(\mathbf{r})] = F[\rho(\mathbf{r})] + \int V_{\text{ext}}(\mathbf{r})\rho(\mathbf{r})d^3\mathbf{r} \quad (4.3)$$

However the exact nature of this functional is not known. Hohenberg and Sham described the true ground state density as the one that minimizes  $E[\rho]$  and  $F[n(\mathbf{r})]$  is a functional of the ground state density whose value was undetermined. For DFT to be useful the value of the density functional  $F[n(\mathbf{r})]$  had to be determined. Following the work of Kohn and Sham, electron density is expressed in terms of a set of orthonormal function one for each of the  $N$  electrons in the system

$$\rho(\mathbf{r}) = \sum_i^N |\phi_i(\mathbf{r})|^2 \quad (4.4)$$

The functional  $F[n(\mathbf{r})]$  is rewritten as a Hartree total energy plus another but unknown functional called the exchange-correlation (xc) functional,  $E_{xc}[\rho]$

$$E[\rho] = T_s[\rho] + E_{ei}[\rho] + E_H[\rho] + E_{ii}[\rho] + E_{xc}[\rho] \quad (4.5)$$

where  $T_s[\rho]$  denotes the single particle kinetic energy,

$$T_s = \sum_i \frac{\hbar}{2m} \int \phi_i^* \Delta^2 \phi_i d^3\mathbf{r} \quad (4.6)$$

$E_{ei}[\rho]$  is the Coulomb interaction energy between the nuclei and the electrons,  $E_{ii}[\rho]$  arises from the interaction of the nuclei with each other and  $E_H[\rho]$  is Hartree component of the electron-electron energy.

$$E_H[\rho] = \frac{e^2}{2} \int \frac{\rho(\vec{r})\rho(\vec{r}')}{|\mathbf{r} - \mathbf{r}'|} d^3(\vec{r})d^3(\vec{r}') \quad (4.7)$$

$E_{xc}$  describes the rest of the contributions to the total energy and is known as the exchange-correlation energy. Local density approximation (LDA) and generalized gradient approximations (GGA) are two common approximation for the exchange-correlation energy. In the LDA approximation the  $E_{xc}$  is given as

$$E_{xc}[\rho] = \int \epsilon_{xc}(\rho)\rho(\mathbf{r})d^3(\mathbf{r}) \quad (4.8)$$

In LDA the functional depends on only on the density at the co-ordinate being evaluated. The Local spin density approximations (LSDA) includes the electronic spins

$$E_{xc}[\rho\uparrow\rho\downarrow] = \int \epsilon_{xc}(\rho\uparrow\rho\downarrow)\rho(\mathbf{r})d^3(\mathbf{r}) \quad (4.9)$$

The GGA approximation takes into account the local density as well as the spatial variation (gradient) of the density

$$E_{xc}[\rho\uparrow\rho\downarrow] = \int \epsilon_{xc}(\rho\uparrow\rho\downarrow\nabla\uparrow\nabla\downarrow)\rho(\mathbf{r})d^3(\mathbf{r}) \quad (4.10)$$

This leads to a set of equations known as Kohn-Sham equations which resemble non-interacting single particle Schrödinger equations [94]

$$(T + V_{ei}(\mathbf{r}) + V_H(\mathbf{r}) + V_{xc}(\mathbf{r}))\phi_i = \epsilon_i\phi_i \quad (4.11)$$

With the density given by a sum over all occupied orbitals

$$\rho(\mathbf{r}) = \sum_{occ} \Phi_i^*(\mathbf{r})\Phi_i(\mathbf{r}) \quad (4.12)$$

The  $\phi_i$  are the single particle orbitals,  $\epsilon_i$  are the corresponding eigenvalues,  $T$  is the kinetic energy operator,  $V_{ei}$  is the exchange correlation potential due to the nuclei,  $V_H$  is the Hartree potential  $\rho(\mathbf{r})$  where,

$$V_H = \frac{\partial E_h}{\partial \rho(\mathbf{r})} \quad (4.13)$$

and  $V_{xc}$  is the exchange correlation potential

$$V_{xc} = \frac{\partial E_{xc}}{\partial \rho(\mathbf{r})} \quad (4.14)$$

The potentials  $V_H$  and  $V_{xc}$  depend on charge density  $\rho(\mathbf{r})$  which in turn depends on Kohn-Sham eigenstates, therefore the Kohn-Sham equations must be solved self-consistently, which means that the potential and charge density must be consistent. A density must be found that yields an effective potential that when inserted into the Schrödinger like equations yields orbitals that reproduce it. The many-body problem thus becomes a case of solving single particle like equations self-consistently.

By solving the Kohn-Sham equations one seeks to compute properties of solids from the first principles. This requires that one find the required wavefunctions. As these are generally not known it is therefore usual to express the wave-functions in terms of a set of known functions known as the basis. A set of single electron wavefunction can then be written as

$$\psi_i(\mathbf{r}) = \sum_{j=1}^{\infty} c_j\psi_j(\mathbf{r}) \quad (4.15)$$

In practise the sum in Equation 4.15 is taken over a finite set of functions. Any set of functions could be in principle used as the basis functions. The basis functions

should ideally have limiting behaviour as real wave function. Computation of the wavefunction in solids is simplified through the use of the crystalline symmetry. An ideal crystal is invariant under symmetry operation, therefore after a symmetry operation a point at  $\mathbf{r}$  is identical to point at  $\mathbf{R}$ . The Bloch's theorem provides a simplification for solids because properties such as potential and charge density have the periodicity of the lattice. According to Bloch's theorem the wave-function can be constructed using plane waves  $e^{i\mathbf{k}\cdot\mathbf{r}}$  with the wave-vector  $\mathbf{k}$  and a periodic function  $U(\mathbf{r})$

$$\psi(\mathbf{r})_{n\mathbf{k}} = e^{i\mathbf{k}\cdot\mathbf{r}} u_{n\mathbf{k}}(\mathbf{r}) \quad (4.16)$$

Where  $\psi(\mathbf{r})_{n\mathbf{k}}$  is the wavefunction, the subscript  $n$  is the band index and  $\mathbf{k}$  is a wavevector that is confined to the first Brillouin zone (BZ) of the reciprocal lattice.  $u_{n\mathbf{k}}(\mathbf{r})$  has the same periodicity as the direct lattice, it can therefore be expressed in terms of a plane-wave basis set with wavevectors,  $\mathbf{G}$ , that are reciprocal lattice vectors of the crystal,

$$u_{n\mathbf{k}}(\mathbf{r}) = \sum_{\mathbf{G}} C_{\mathbf{G}} \exp(i\mathbf{G}\cdot\mathbf{r}) \quad (4.17)$$

Where  $\mathbf{G}$  is the reciprocal lattice vector given by  $\mathbf{G}\cdot\mathbf{R} = 2\pi$  and  $C_{\mathbf{G}}$  are the coefficients of expansion. Substituting  $u_{n\mathbf{k}}(\mathbf{r})$  to equation Equation 4.16 the eigenvalues for the Kohn-Sham equations can be calculated. The problem of is therefore reduced to a finite number of bands and K-points. A general solution of the Kohn-Sham equation can be obtained by using plane waves as the basis set. In order to solve this problem the Kohn-Sham orbitals  $\psi_i$  have to be represented by a linear combination of a finite number of basis set [95,96]. The difficulty arise on how to accurately to describe the potential and the core and valence electronic states in the crystal. Core states are highly localized have large energies and they require high energies. Valence states have small energies are significantly delocalized and can be represented by plane waves. To solve this problems several methods have been developed two of the most common ones include Pseudo-potential plane wave method and the linearized augmented plane waves (LAPW).

### Pseudo-potential method

The pseudo-potential method makes the approximation that the core electrons are tightly bound to nuclei, and only the valence electrons are involved in bonding, conductivity or chemical reactions. The wavefunctions of the core electrons are rapidly varying with many nodes due to the strong potential and orthogonality condition between different states and require a large number of waves and huge computation resources to model accurately. In the frozen core approximation the core states are incorporated into a bulk nuclear potential, or pseudo-potential, and the valence electrons are then modelled using Bloch waves. The pseudopotential acts on a set of pseudo wavefunctions rather than the true valence wavefunctions.

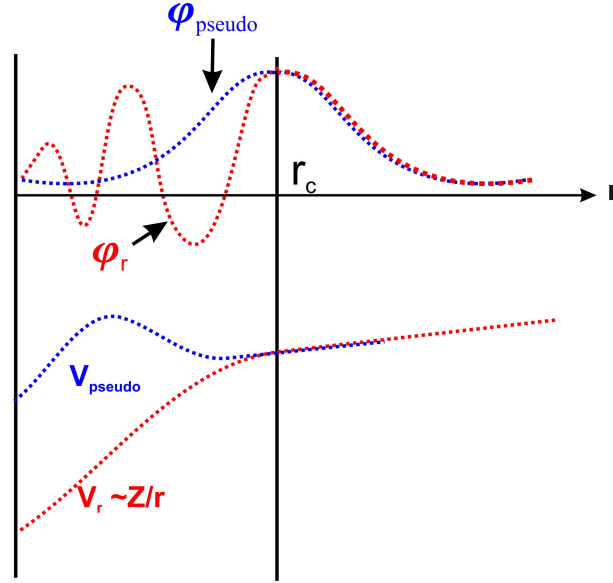


*Figure 4.1: The all-electron wavefunction and potential (red dotted lines) plotted against distance,  $r$ , from the atomic nucleus. The corresponding pseudo wavefunction and potential is plotted (Blue dotted lines). Beyond a given radius  $r_c$  the electron and pseudo-wavefunction and potential are the same.*

Between the nucleus and a certain cut-off radius  $r_c$  the all-electron wavefunction can be replaced with a smoothed pseudo-wavefunction without nodes; beyond this radius the pseudo-wavefunction must be identical to the all-electron wavefunction. Figure 4.1 illustrates schematically the all-electron wave function  $\psi_v$  and potential  $V_r$  and the pseudowavefunction  $\psi_{\text{pseudo}}$  and potential  $V_{\text{pseudo}}$  [95, 96]

### Full potential linearized augmented plane waves (FLAPW)

In the FLAPW method, near the atomic nucleus, the atomic potential and wavefunctions are similar to those of an atom- they are strongly varying but nearly spherical [95, 97–99]. Between the atoms both the potential and the wavefunction are smoother. The space is therefore divided into regions and different expansions are used in these regions. Radial solutions of the Schrödinger equation are used inside the overlapping-atom centered sphere and the planewaves in the interstitial regions. Electrons far away from the nuclei behave like free electrons and can thus be described using plane waves, the electrons near the nuclei are tightly bound and have an atomic like character and are described using atomic functions. FLAPW methods utilize what is known as the muffin-tin concept [100]. Figure 4.2 shows the division of a unit cell into interstitial and muffin-tin regions in the FLAPW method

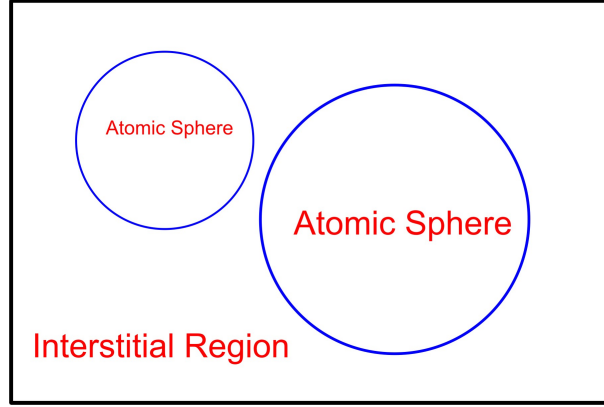


Figure 4.2: Division of a unit cell into interstitial and atomic sphere regions in LAPW method

Within the interstitial region the wavefunction is expanded using bloch waves

$$\psi_{kn} = \frac{1}{\sqrt{\omega}} e^{i\mathbf{k} \cdot \mathbf{r}} \quad (4.18)$$

To correctly describe the wavefunction near the nucleus the plane wave set is augmented, meaning the wavefunction is expanded as a radial function  $\mu_l(r, E_l)$ , multiplied with spherical harmonics,  $Y_{lm}(r)$ .  $\mu_l(r, E_l)$  is obtained from the solution of the schrödinger equation for spherical potential for an energy  $E_l$

$$\left\{ -\frac{d^2}{dr^2} + \frac{l(l+1)}{r^2} V(r) - E \right\} r\mu_l \quad (4.19)$$

A problem arises in this method in that the basis functions depend on the energy and if the functions within the atomic sphere change rapidly with energy it can give rise to uncorrect results. To overcome this problem the intrinsic energy dependence of the basis functions is linearized by expanding the functions, to the first order with respect to the deviation from an a chosen reference energy [99]. In LAPW the radial functions are linearized through a first order Taylor expansion of the radial function  $\mu_l(r, E_l)$

$$\mu_l(r, E_l) \simeq \mu_l(r, E_l) + \dot{\mu}_l(r, E_l) \quad (4.20)$$

The wavefunction within the atomic sphere is thus reduced to

$$\phi_{\text{sphere}} = \sum_{lm} \left[ A_{lm} \mu_l(r, E_l) + B_{lm} \dot{\mu}_l(r, E_l) \right] Y_{lm}(\hat{r}) \quad (4.21)$$

The results presented in this thesis have been calculated using the Full Potential LAPW method as implemented in the WIEN2K code [101]

## Electronic Density of States

The electronic density of states (DOS) is one of the quantities used to describe the electronic state of materials and can be described as  $\rho(E)dE = \text{number of electron states with energies, } E, \text{ in interval } (E, E + dE)$ . In plane waves DFT the electronic density can be described in functions of the form  $\exp(i\mathbf{k} \cdot \mathbf{r})$ . Electrons associated with the functions of this form have energy  $E = \frac{(\hbar\mathbf{k})^2}{2m}$ . After a DFT calculation is done the electronic DOS is obtained by intergrating the resulting electronic density in K space [102].

The DOS can also be represented as partial density of states (PDOS) also known local density of states (LDOS). This is the number of electronic states at a specified energy weighted by the fraction of the total electron density for those states that appears in a specified volume around a nuclei. For example the total DOS of  $\text{LiFePO}_4$  can also be represented in terms of s,p, d PDOS for the Li, Fe, O and P atoms.

## Calculating VEELS spectrum from DFT

As was shown in section 3.1.2, the intensity of an EELS edge can be written as the product of the density of states and an atomic transition matrix.

$$I(E, \mathbf{q}) \propto |\langle f | \mathbf{q} \cdot \mathbf{r} | i \rangle|^2 \rho(E) \quad (4.22)$$

where the  $|i\rangle$  and  $|f\rangle$  are the initial and final states respectively. The quantity  $\rho(E)$  is the density of the unoccupied states and  $\mathbf{q}$  is the momentum transfer. This method is based on the single particle approximation, which assumes that final states are not modified significantly by d electron exchange and core hole effects. Therefore this method gives As indicated in section (3.1.2), the low loss energy spectrum can be described using the loss function which is proportional to the dielectric function of the solid electrons [66,103].

$$I_{\text{EELS}} \propto \text{Im}[\epsilon(\omega, \mathbf{q})]^{-1} = \frac{\epsilon_2}{(\epsilon_2^2 + \epsilon_1^2)} \quad (4.23)$$

Where  $\epsilon(\omega, \mathbf{q})$  is the dielectric function given by,

$$\epsilon(\omega) = \epsilon_1(\omega) + i\epsilon_2(\omega) \quad (4.24)$$

where  $\epsilon_1(\omega)$  and  $\epsilon_2(\omega)$  are real and imaginary parts of the dielectric function respectively. The imaginary part of the dielectric tensor is directly related to the electronic band structure of a solid and can be computed by solving the Kohn-Sham equations. The dielectric function  $\epsilon$  can be calculated from band-structure calculations once energies  $E_{kn}$  and the wave functions  $|nk\rangle$  for the  $n$  bands have been obtained from Kohn-Sham equations. The imaginary part of the dielectric functions  $\epsilon_2$  can be calculated by summing transitions from occupied to unoccupied states over the brillouin zone and weighted with the appropriate matrix



element for the probability of the transition. The imaginary part of the dielectric function is obtained from

$$\text{Im}\epsilon_{ij} = \frac{4\pi^2 e^2}{m^2 (\omega - \frac{\omega - \Delta_c}{\hbar})^2 V} \sum_{v,c,k} \langle v_k | p_j | c_k \rangle \langle c_k | p_i | v_k \rangle \times \delta(E_{c_k} + \Delta_c - E_{v_k} - \hbar\omega) \quad (4.25)$$

where  $|c_k\rangle$  and  $|v_k\rangle$  are approximated by the Kohn-Sham orbitals with the wave vector  $k$  for conduction and valence bands respectively.  $E_{c_k}$  and  $E_{v_k}$  are the corresponding band energies, and  $p_i$  the cartesian component of the momentum operator.  $m$  is the mass for a free electron,  $e$  is the electron charge  $\omega$  is the frequency, and  $V$  stands for the volume of the unit cell. [104]

The real part of the dielectric function is then calculated from  $\epsilon_2$  by KKA [105]

$$\epsilon_1(\omega) - 1 = \frac{2}{\pi} \int_0^\infty d\omega' \epsilon_2(\omega') \left[ \frac{\omega'}{\omega^2 - \omega'^2} \right] \quad (4.26)$$

Calculated and experimental VEELS may show differences in intensity and peak features effects as the limited resolution of the spectrometer or the finite lifetime of excited states. To facilitate the comparison between theory and experiment, the theoretical spectra must therefore be convoluted by a broadening function.

- **Lifetime of the excited electronic states broadening effects** The features of the ionization edges are often smeared out because of the lifetime broadening of the core-hole. There are two major core-hole decay processes: fluorescence and Auger. In fluorescence, another electron of the atom fills the core hole. This process can only occur if the energy of the electron is higher than the core hole. The energy difference between these two states is released as electromagnetic radiation. The second process is Auger decay. When an electron from the 2p shell drops to fill a vacancy formed by 1s shell ionization, the resulting x-ray photon 1s may excite a third electron, for example, another 2p electron. Such a process can be denoted as a 1s2p2p Auger process. Lifetime broadening of the Auger type electron interaction processes can distort the measured spectra. The effect is a smearing out of the finer details in an EELS spectrum. [106]
- **Instrumental broadening effects** Instrumental broadening is a function of the spectrometer employed for the measurement. It is often treated together by gaussian broadening function. [60]
- **Local Field effects** Local field effects arise since when in the calculation only the diagonal elements of the dielectric matrix are calculated. However the off-diagonal matrix elements also contribute significantly to the calculated spectra. Non inclusion of local field effects produces disagreement between the intensities of the calculated and the theoretical low loss spectra. [107,108]

## Calculating Core-Loss Spectra from DFT

Ideally the EELS spectrum can be described by the excitation of a single electron from a ground state to an excited state. For the calculation of core spectra, the two main tasks are then evaluation of the density of unoccupied electronic states term and the weighting transition matrix elements. [96,109,110]. Using the band-structure method, the core-loss spectra can be represented by the double differential scattering cross section given in equation (3.11). The double differential cross-section for inelastic electron scattering is related to the Dynamic Form Factor (DFF).

$$\text{DFF} = \sum_{ij} |\langle \Psi_i | e^{i\mathbf{q} \cdot \mathbf{r}} | \Psi_f \rangle|^2 \delta(E + E_i - E_f) \quad (4.27)$$

Where the summation is over all occupied initial  $\langle \Psi_i |$  and final states  $\langle \Psi_f |$  the initial state is represented by an atomic core state and the final state by a Bloch wave which can be projected onto a basis set of atomic orbitals. Herbert et al [110] give the formula for calculating the DFF for a polycrystalline sample within the FLAPW code as

$$\text{DFF}(\mathbf{q}, E) = 0l \sum_{\lambda=0}^{\infty} \sum_{l'=|l-\lambda|}^{l+\lambda} \chi_{l'}^t(\epsilon') \times (2\lambda+1) \times \begin{pmatrix} l & \lambda & l' \\ 0 & 0 & 0 \end{pmatrix}^2 < j\lambda(q) >_{n\epsilon' l l'}^2 \quad (4.28)$$

$\lambda$  is the transfer of angular momentum in the interaction,  $l$  the initial and  $l'$  is the final angular momenta.  $0l = 2(2l+1)$  is the statistical occupation number of the initial state.  $\chi_{l'}^t(\epsilon')$  is the partial DOS for angular momentum  $l'$  at atom  $t$  and for the energy  $\epsilon'$  above Fermi level;  $< j\lambda(q) >_{n\epsilon' l l'}^2$  is the matrix element of the spherical Bessel function of order  $\lambda$  between the radial parts of the initial and final states.

### 4.1.2 Ligand Field Multiplet Method

The total Hamiltonian used in ligand field method is

$$H = H_{\text{atom}} + H_{\text{crystal}} + H_{\text{CI}} \quad (4.29)$$

$H_{\text{atom}}$  describes hamiltonian for an isolated atom,  $H_{\text{crystal}}$  describe the state of atom surrounded by ligands in a crystal while  $H_{\text{CI}}$  describes the effects of the interaction of the ligand with the atom.

#### Atomic Multiplet

To describe spectra in strongly correlated materials a good point is the analysis of isolated atoms using the the atomic multiplet theory. In this case, for an N-

electron atom the atomic Hamiltonian is given by

$$H = H_{ave} + H_{ls} + H_{ee} \quad (4.30)$$

where

$$\begin{aligned} H_{ave} &= \sum_N \frac{p_i^2}{2m} + \sum_N \frac{-Ze^2}{r_{ij}} \\ H_{ls} &= \sum_N \xi(r_i) l_i \cdot S_i \\ H_{ee} &= \sum_{pairs} \frac{e^2}{r_{ij}} \end{aligned} \quad (4.31)$$

$$H = \sum_N \frac{p_i^2}{2m} + \sum_N \frac{-Ze^2}{r_{ij}} + \sum_{pairs} \frac{e^2}{r_{ij}} + \sum_N \xi(r_i) l_i \cdot S_i \quad (4.32)$$

$H_{ave}$  is the average energy and contains the kinetic term and the interaction of the electron with the nucleus  $H_{ls}$  represents the spin-orbit coupling of the electrons, the electron-electron interaction is given by  $H_{ee}$ . The kinetic energy and the interaction with the nucleus for all electrons in a certain atomic configuration can be assumed to be the same. This means that leaves the the electron-electron repulsion and the spin-orbit coupling as the most important interactions to be considered. [111]

### Matrix Elements

To determine the energies of the different terms, we have to calculate the matrix elements of these states by considering the energies of the different terms which is determined by calculating the matrix elements of these states with the electron-electron interaction  $H_{ee}$  and the spin-orbit coupling  $H_{ls}$ . The general formulation of the matrix elements of the effective electron-electron interaction is given by:

$$\langle {}^{2S+1}L_J | \frac{e^2}{r_{ij}} | {}^{2S+1}L_J \rangle = \sum_f f_k F^k + \sum_k g_k G^k \quad (4.33)$$

$F^i(fi)$  and  $G^i(gi)$  are the Slater-Condon parameters for, the radial (angular) part of the direct Coulomb repulsion and the Coulomb exchange interaction respectively. [100]

### Crystal Field

The atomic multiplet theory considers an isolated atom, however most spectra is not acquired from isolated atoms but in crystal structures. Therefore the effects of the local environment have to be added in order to describe the effects of local symmetry. In our case the Fe atom is taken to be in an octahedral environment with six O atoms. This has already been explained in Chapter 2. In this case the ligand field splitting parameter,  $10Dq$  is the dominant factor that influences the spectra shape. According to Hund's rules, for a  $10Dq$ , the electron will occupy a

state with its spin parallel to other electrons giving rise to a high-spin state. In large 10Dq the electron occupies a state with the spin direction opposite to the other electrons giving rise to a low spin state. The spin state drastically changes the features in the EELS spectra as will be shown in latter chapters.

### Charge Transfer Effects

The description of hybridization, and orbital mixing between the transition metal ion and the ligand is included into the ligand multiplet theory through the configuration interaction  $H_{CI}$ . In which the electronic configurations of the ground state is a mixture of several configurations arising due to transfer of charge between the ligand and the metal ion. As shown in Equation(2.7), the average energy of each configuration is determined by the charge-transfer energy  $\Delta$ , which is the energy required to transfer an electron from the ligand ion to the transition metal ion. For example for a transition metal with  $d^n$  state the configurations available include  $|d^n\rangle, |d^{n+1}\underline{L}\rangle, |d^{n+2}\underline{L}^2\rangle, \dots$  where  $\underline{L}$  represents a core-hole in ligands valence band. The effect of charge transfer is to form a ground state that is a combination of all possible configurations. In most cases two configurations will be enough to explain the spectral shapes.

#### 4.1.3 Spectroscopic notations

The energy state of an electron is given using the  $n, l, s, j$  quantum numbers [112]. Where,  $n, l, s$  and  $j$  are the principal quantum number, orbital quantum number, electron spin and total angular momentum number respectively. For each  $n$ ,  $l$  has the values 0, 1, 2, 3, ... ( $n - 1$ ) which are levels are denoted as s, p, d, f, ..., respectively. The total angular momentum number is given as  $j = l \pm s$  ( $s = 1/2$ ). The electron spin can have the values of  $s = \pm 1/2$ . The energy state of an atoms is given by quantum numbers  $L, J, S$  representing the total orbital momentum, spin and angular momentum respectively. A particular atomic configuration is indicated with using the term symbol  $^{2S+1}L_J$ . For example 1s electron have at total orbital moment  $L = 0$ , a spin moment  $S = 1/2$ , and a total angular moment  $J = 1/2$ . This is written with a term symbol as  $^2S_{1/2}$ . A 2p electron has two possible symmetries depending on the spin-orbit coupling,  $^2P_{1/2}$  and  $^2P_{3/2}$ . These two configurations give rise to the multiplet structure observed in the  $L_2$  and the  $L_3$  edge in transition metals [111, 113].

## 4.2 Convergence tests

Before electronic calculations can be done it is important to test the various parameters in order to get physically meaningful results and to save computational time. The main parameters include:

**Number of K points** This is the number of irreducible k-points needed to describe the energy bands within the Irreducible Brillouin zone (IBZ). The dependence of energy to the number of points is shown in Figure 4.3. It can be seen that good energy convergence is achieved by using at least 50 K-points. In this thesis the number of k-points in the IBZ was 74 and 64 for  $\text{LiFePO}_4$  and  $\text{FePO}_4$  respectively.

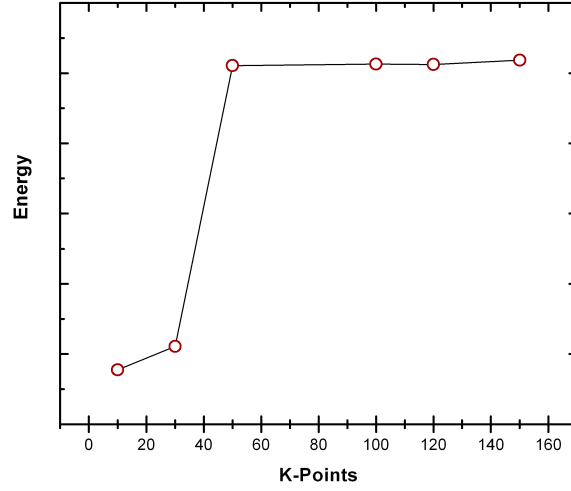
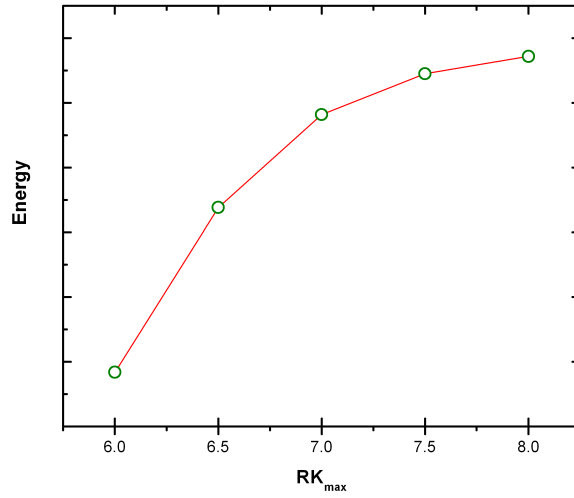


Figure 4.3: Effect of the number of K points on total energy

**Plane wave cutoff** In FLAPW method the space is divided into muffin tin and interstitial regions (see Chapter 3). Different functions are then used to describe the atomic wavefunction and potential in these regions. In the interstitial region the wavefunctions are expanded as plane waves (see Equation 3.43). Ideally the wavefunction and potential should be expanded to infinity but this is not possible due to limited computational resources and therefore the potential and wavefunction have to be expanded to some cut-off energy and still have physically meaningful results. In Wien2k the plane wave cutoff is represented by the value  $RK_{\text{max}}$  which is the product of the plane wave cut-off and the smallest atomic sphere radii (muffin tin radius). Figure 4.4 shows the calculated total energy versus the value of  $RK_{\text{max}}$ .

It can be seen that good energy convergence is achieved by using at least using a  $RK_{\text{max}}$  value of 7-8.

**Angular momentum** Inside the muffin tin the potential is expanded as a linear combination of spherical waves (see Equations 3.44-3.46). It is important to find the maximum number of angular momenta,  $l_{\text{max}}$  for the wave functions inside the spheres. In this thesis the valence wave functions inside the



*Figure 4.4: Effect of the plane wave cutoff on the calculated total energy*

spheres are expanded up to,  $L_{\max} = 10$ , while the charge density was Fourier expanded up to  $G_{\max} = 14$ .

**Convergence criteria** Calculations are considered well converged when the difference in the energy of consecutive cycles is better than  $0.0001 \text{ Ry}$  ( $1.36e^{-3} \text{ eV}$ ).

# Part III

## Results and Discussion





## Beam effects on $\text{LiFePO}_4$ spectra

The high energy electrons used in EELS and HRTEM investigations can cause physical damage, electronic and chemical changes in the sample being investigated. This may lead to the modification of the obtained results and in some cases lead to the mis-interpretation of the obtained results [59]. This chapter deals with the effects of the electron beam induced changes on the obtained EELS spectra of  $\text{LiFePO}_4$ . By monitoring the changes in the peak fine structure and peak positions as a function of beam exposure time, it is possible to investigate the extent into which the electron beam introduces stoichiometric, electronic and physical changes into the sample. This is based on the fact that the peaks in EELS spectra are related to the electronic and crystal structure of the material under study. The experimental details, results and discussion are given in Sec. 5.1, Sec. 5.2, Sec. 5.3 respectively. In particular we investigate variation of experimental parameters in order to avoid beam induced damage.

### 5.1 Experimental Details

Sample damage was investigated using EELS acquired at two different incident beam energies, 80 kV and 300 kV respectively. The effect of the electron beam was investigated by exposing the sample to the electron beam for a period time and acquiring the EELS spectra every 30 seconds on a particular region on a grain. The electron current and dose were kept constant.

## 5.2 Results

### 5.2.1 Beam effects on Li-K edge

Figure 5.1(a) and ?? show the Li-K edge and Fe – M<sub>2,3</sub> edge (55-57 eV) absorption edges as a function of exposure time and accelerating voltage. As shown in Figure 5.1(a) , at low incident beam energies of 80kV, the Li-K edge and FeM<sub>2,3</sub> edges show very little changes in intensity and only slight changes in the fine structure. In contrast the Li-K edge and FeM<sub>2,3</sub> edges show a drastic change in intensity and fine structure when the incident beam energy is increased to 300 kV as shown in ?? . Since the intensity of the core-loss EELS is proportional to the number of the corresponding atoms in the exposed area, a decrease in intensity at the Li-K and FeM<sub>2,3</sub> edge points towards the displacement of Li atoms from crystal at high incident beam energies.

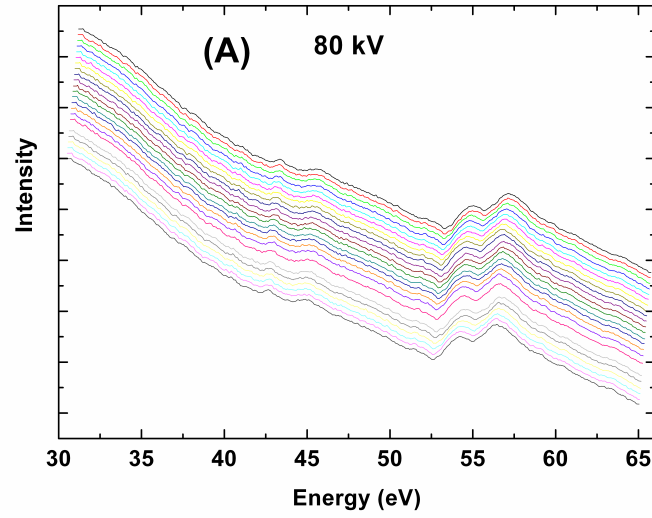
Due to the overlap of the of Li K edge and FeM<sub>2,3</sub> it is hard to accurately analyze the changes in the fine structure and hence the O-K and FeL<sub>2,3</sub> edges are used to study the effects of the electron beam on the sample in more details.

### 5.2.2 Beam effects on O-K edge

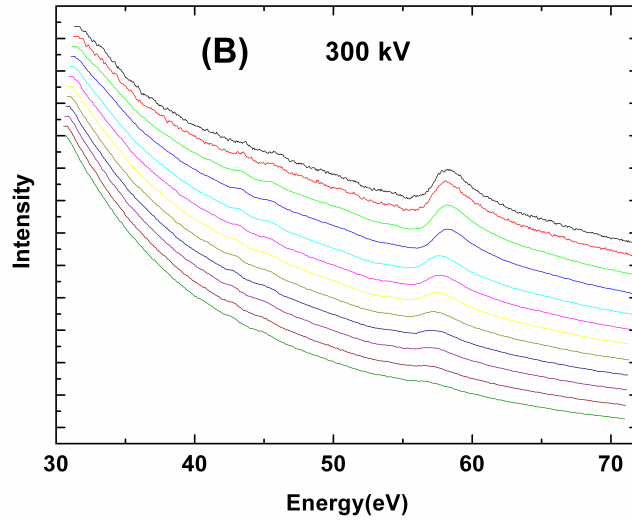
Figure 5.2(a) and 5.2(b) show the O-K edge as a function of the exposure to the electron beam for LiFePO<sub>4</sub> and FePO<sub>4</sub>. The O-K edge shows significant changes with increased exposure to the electron beam, particularly the growth of the pre-edge peak. The O-K spectrum for LiFePO<sub>4</sub> in Figure 5.2(a) shows a growing pre-edge peak at about 529 eV and a broader peak centered at around 536 eV. The O-K edge pre-peak also exists in the spectrum of FePO<sub>4</sub> as shown in 5.2(b), however increased exposure time increases the intensity of the pre-edge peak. Increased exposure to the electron beam leads to the development of a pre-edge peak at the O-K edge which is similar to the one observed after delithiation of LiFePO<sub>4</sub> but with several key differences. Firstly, the intensity of the pre-edge peak grows with increased exposure to the electron beam. Secondly, the position of the pre-peak shifts to lower energies with increased exposure time.

### 5.2.3 Beam effects on FeL<sub>2,3</sub> edge

A series of FeL<sub>2,3</sub> spectra were also acquired from the same region. Figure 5.3(a) shows a series of FeL<sub>2,3</sub> spectra as a function of irradiation time. The L<sub>3</sub> peak is much more intense than the L<sub>2</sub> peak and the changes in the fine structure are thus more easily observed at the FeL<sub>3</sub> edge. At the beginning of exposure experiment the L<sub>3</sub> edge for undelithiated sample is characterized by a main peak, at 708 eV and a shoulder at  $\approx$  710 eV respectively. With increasing exposure time the intensity of the shoulder grows in relation to the main peak. After some time the L<sub>3</sub> edge is then characterized by two peaks of approximately equal intensity.



(a) 80kV



(b) 300kV

*Figure 5.1: Li-K and Fe –  $M_{2,3}$  edge as a function of exposure time taken at (a) 80 kV (b) 300 kV. The intensity at the Li-K edge decreases rapidly with exposure times at 300 kV. At 80 kV very little change is observed at the Li-K edge*

The splitting of the  $L_3$  edge has been attributed to the ratio between  $\text{Fe}^{2+}$  and  $\text{Fe}^{3+}$  in the region under study [114]. Before exposure to the electron beam, the area under investigation consists of  $\text{Fe}^{2+}$ , increased exposure to the electron beam

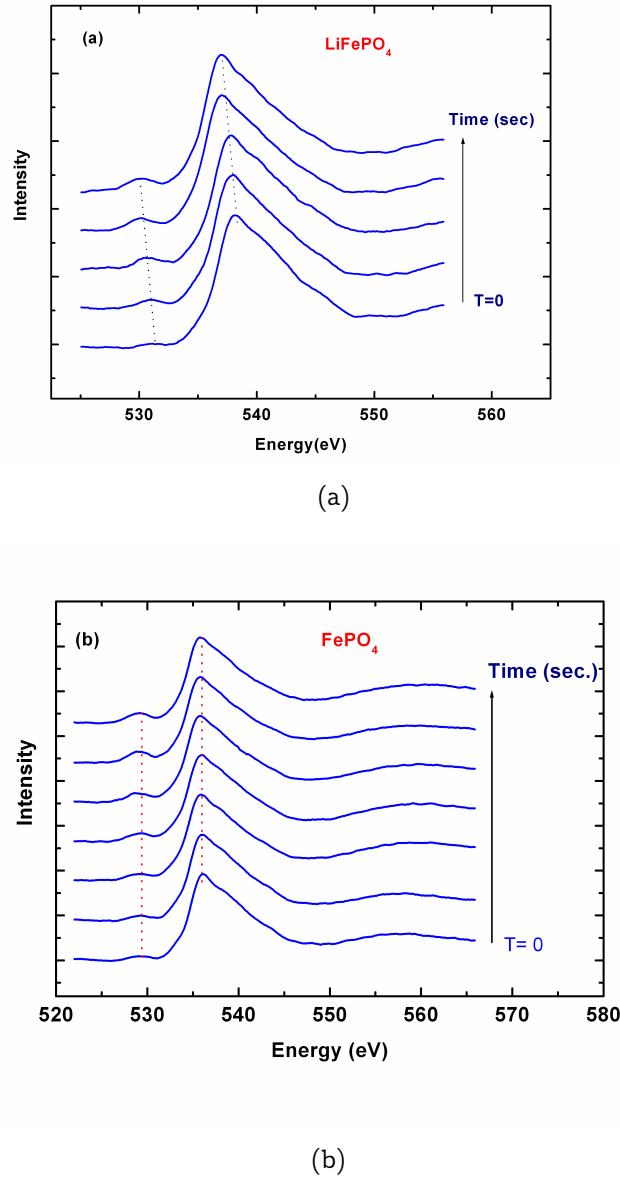
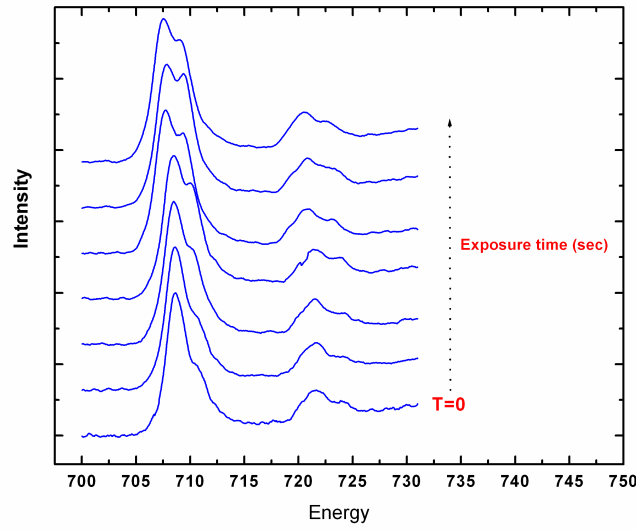


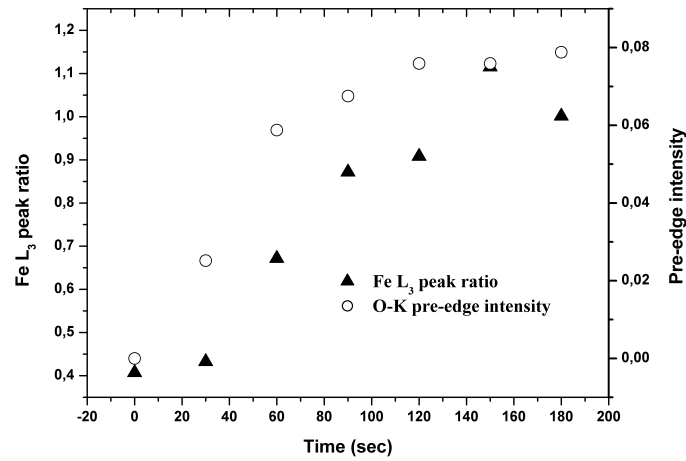
*Figure 5.2: Monitoring electron beam induced changes on the O-K edge for (a)  $\text{LiFePO}_4$  and (b)  $\text{FePO}_4$ . Beam induced damage is characterized by a rise of a pre-edge peak on the O-K edge of  $\text{LiFePO}_4$*

. The dotted lines are guide for the eye showing the increase in the intensity and the shift of the pre-edge peak

leads to a beam-induced oxidation of  $\text{Fe}^{2+}$  and this change in the oxidation state is then reflected by the growing intensity of the second peak at  $\approx 710$  eV. Figure 5.3(b) shows a plot of the integrated intensities of the shoulder peak at the  $\text{FeL}_3$  edge plotted against intensity of the O-K pre-edge peak. This plot shows that the



(a)



(b)

*Figure 5.3: .*

(a) Beam induced changes on the FeL<sub>2,3</sub> edges (b) Ratio of FeL<sub>3</sub> peaks plotted with the integrated intensity of the O-K pre-edge as a function of exposure time (in sec.). The peak ratios have been obtained by taking the integrated intensity of the peaks at the FeL<sub>3</sub> edge ( $\approx 709$  eV)

increase in the pre-edge intensity corresponds to the oxidation of the Fe atoms from Fe<sup>2+</sup> to Fe<sup>3+</sup>.

### 5.3 Discussion

The process of radiation damage from high energy electrons is a very complex process being a combination of several processes including, breaking of bonds and atomic displacement (ionization damage), surface and bulk sputtering (knock-on damage), beam heating, vacancy, defect and atomic diffusion, and electrostatic charging [59,115,116]. These processes depend on the incident beam energy, the electron dose, and the bonding properties of the material under irradiation. While radiation damage most likely involves a combination of all these processes, ionization damage seems to be playing the dominant role in the experiments conducted at 80 kV. This conclusion is based on the fact that no reduction in the intensity of the absorption edges was observed for the various edges. Knock-on damage results in rapid mass-loss of various elements and which in turn leads to a decrease in the intensity of the respective absorption edges. This is explained by the fact that the intensity a given EELS signal is proportional to the number of atoms in the area under illumination [60,117]. In contrast the experiments conducted at 300 kV lead to drastic reduction of intensity at Li-K edge and it can be deduced that the beam damage is of the knock-on type which leads to the mass-loss of the Li atoms. Knock-on displacement is characterized by the threshold displacement energy,  $E_d$ , which is the energy that must be transferred to an atom to remove it from its site. As shown in Figure 5.2(a) increased exposure of the sample to the electron beam gives rise to the pre-edge feature on the O-K edge whose intensity increases with exposure time. This pre-edge peak is as a result of chemical and structural rearrangement arising as a result of radiation damage from the high energy electrons. The pre-edge peak in O 1s spectra has been frequently observed many transition metal compounds particularly superconductors showing a wide range of Oxygen stoichiometry [118–123]. In these compounds it was observed that the intensity of the pre-edge peak was very sensitive to the changes in the stoichiometry of the oxygen in these compounds [124–126]. It was also shown that the changes at the FeL<sub>2,3</sub> edge were mirrored by the growth of the pre-edge intensity. Changes in the oxidation state were observed at the FeL<sub>2,3</sub> edge with increased exposure which means the valence electron density around the Fe ion decreases when the Fe<sup>2+</sup> ion is oxidized to Fe<sup>3+</sup>. Due to hybridization of the Fe-O bond a change in the valency of the Fe ion will affect the O 2p states as well. A possible mechanism that could give rise to the pre-edge peak would be production of the O<sub>2</sub> molecules from the sample. This proceeds through the auger-electron cascade mechanism [127]. In electron energy loss spectroscopy, an incident electron can lose energy by exciting an electron from the core state of an atom to the valence band. The relaxation of the ensuing excited state can then proceed through the emission of a photon or by emission of a secondary electron into the vacuum (auger-emission). This process results in the formation of two core holes in the valence band, one to fill the core hole left due to the excited electron and the second due to the emit-

ted auger electron. To preserve charge neutrality two electrons can be extracted from the  $O^{2-}$  which is reduced and released into the vacuum as  $O_2$ . The end result of this process is the formation of atomic vacancies, changes in the oxidation states and electric-field driven ionic diffusion [116]. It is worth mentioning that this process is a surface-driven effect and can be influenced by contamination on the sample surface and that other bulk based mechanism cannot be discounted. As such the mechanism of radiation damage in  $LiFePO_4$  and other Lithium compounds needs further investigations. The fact that the pre-edge peak is observed both in radiation damaged and delithiated sample does not necessarily mean that process of radiation damage and delithiation are similar. But the results suggest that both processes result in the formation of unoccupied states in O-2p state of the conduction band which then modulate the fine structure of the O 1s edge. A further interesting application is that the electron beam-induced changes can also be useful tool to study the local electronic and atomic structures.

## 5.4 Conclusion

The effects of the electron beam on the obtained EELS spectra of  $LiFePO_4$  have been examined. It was seen that at high acceleration voltages of 300 kV the intensity of the EELS spectra at Li-K edge decreased rapidly with exposure time. This decrease in intensity is interpreted to be due to preferential loss of Li from the  $LiFePO_4$  lattice. In this case loss of Li atoms from the lattice. Beam damage at 80 kV is characterized by changes in fine structure of the ionization edges. Contrary to the damage at 300 kV there is no decrease in intensity of the ionization edges. This means at low voltages the mass loss of atoms from the lattice is minimal. At this low voltage sample damage is induced by changes in oxidation states of the various ions present in the sample. This was observed by the changes in the fine structure of  $FeL_{2,3}$  edge and the pre-edge peak in the O-K edge. Reduction of sample damage by the electron beam was accomplished by reducing the energy of the incident electrons, reducing the electron dose on the sample and reducing the time the sample is exposed to the electron beam.





## Valence-loss Spectra in $\text{Li}_{(1-x)}\text{FePO}_4$

In this chapter, we focus on VEELS spectra before delithiation ( $\text{LiFePO}_4$ ) and after delithiation ( $\text{FePO}_4$ ). As previously mentioned in Chap.3, VEELS spectra is mainly characterized by excitations which rise from the valence band to the conduction band. These include plasmon, inter-band (and intraband transitions in metals), or relativistic losses. As such VEELS gives a good description of the electronic band structure in the valence region. However interpretation of VEELS spectra is difficult due to the large number of excitations and phenomena that characterize it. This is one of the reasons why VEELS is not so widely used as core-loss EELS. In order to interpret VEELS theoretical calculations are often necessary. Experimental and theoretical details are given in Sec.6.1. The results obtained are discussed in terms of the nature, character and origin of the observed VEELS excitations which are given in more details in Sec. 6.2. The chapter concludes by outlining what VEELS spectra ( and the associated calculations) reveal about the electronic structure changes with delithiation.

### 6.1 Experimental and calculation details

VEELS spectra were acquired from single crystal  $\text{LiFePO}_4$  and powder samples for  $\text{LiFePO}_4$  and  $\text{FePO}_4$ . The single-scattering spectrum,  $S(E)$ , was extracted from the VEELS spectra by deconvolution of the VEELS spectra with the ZLP obtained from the vacuum, and correction for multiple scattering using the Fourier-log deconvolution methods described in Chapter 3. The real part  $\epsilon_1$  and the imaginary part  $\epsilon_2$  of the dielectric function were then derived using the KKA analysis of the single scattering spectrum as described in Chapter 3.

The electronic and spectral properties of the  $\text{LiFePO}_4$  and its delithiated state  $\text{FePO}_4$  are calculated by solving the Kohn-Sham (KS) equations [94] within the FLAPW approximation as implemented in WIEN2k code [101]. The lattice parameters used in calculations were for  $\text{LiFePO}_4$   $a = 10.332 \text{ \AA}$ ,  $b = 6.010 \text{ \AA}$ ,  $c = 4.692 \text{ \AA}$  [11] and for  $\text{FePO}_4$   $a = 9.9284 \text{ \AA}$  and  $b = 6.010 \text{ \AA}$ ,  $c = 4.692 \text{ \AA}$  [15]. The refractive index for  $\text{LiFePO}_4$  and  $\text{FePO}_4$  were taken from obtained from literature and ranges between 1.67 and 1.7 [128]. Both lithiated and delithiated crystals have an orthorhombic unit cell and are indexed to space group Pnma. The muffin tin radii of 1.36 a.u, 1.46 a.u, 1.97 a.u and 2.09 a.u, for O, P, Li and Fe atoms were used. The main parameters used in the calculations were introduced in Chapter 4. In order to treat the effects of local Coulomb interactions in the 3d electrons of Fe, the GGA+U method was used. The values of the Coulomb (U) and exchange (J) parameters were set to  $U = 4 \text{ eV}$  and  $J = 0.0 \text{ eV}$  for both sets of calculations respectively. In the calculations of the VEELS spectra and the optical constants, the Optic package of the Wien2k code was used [101, 104]. Dense k-point meshes of 286 and 195 k-points in the IBZ were used for  $\text{LiFePO}_4$  and  $\text{FePO}_4$  super-cells respectively. The lifetime broadening was simulated by convoluting the spectra with a Lorentzian function. The experimental resolution was simulated by broadening the final spectra with a Gaussian function whose FWHM is set to 0.02 eV.  $\text{LiFePO}_4$  and  $\text{FePO}_4$  have an orthorhombic crystal structure, the dielectric function is therefore anisotropic. Consequently, the diagonal components of the dielectric tensor  $\epsilon_{xx}$ ,  $\epsilon_{yy}$ ,  $\epsilon_{zz}$  corresponding to the crystallographic axes  $a$ ,  $b$  and  $c$ , respectively were calculated.

## 6.2 Results and Discussion

### 6.2.1 Valence loss spectra

Figure 6.1 shows the experimental  $\text{LiFePO}_4$ , and  $\text{FePO}_4$  VEELS spectrum for the energy region 0-40 eV. The VEELS spectrum of  $\text{FePO}_4$  (drawn with the red curve) shows a strong peak in the energy range 4-8 eV observed after the spectrum onset.

This is labeled as peak (i). In the spectrum of  $\text{LiFePO}_4$ , (drawn with the black curve), this peak is much less intense and is replaced by a small shoulder at this energy range. The  $\text{FePO}_4$  spectrum further shows two broad peaks in the energy region 12-20 eV labeled (ii) and (iii). These peak features are also much less intense in the  $\text{LiFePO}_4$  spectrum. A common feature in both spectra is a prominent peak at about  $\approx 23 \text{ eV}$  which is labeled as peak (iv). The peak feature labeled (v) is also present in both phases and is observed at higher energies. Comparing the  $\text{LiFePO}_4$  and  $\text{FePO}_4$  spectra shows that the most important difference between both sets of spectra is in the energy region 4-20 eV where the  $\text{FePO}_4$  spectra shows several peaks that are either not observed or are less intense in  $\text{LiFePO}_4$  spectra. In order to interpret the differences in  $\text{LiFePO}_4$  and  $\text{FePO}_4$  spectra, several factors have to

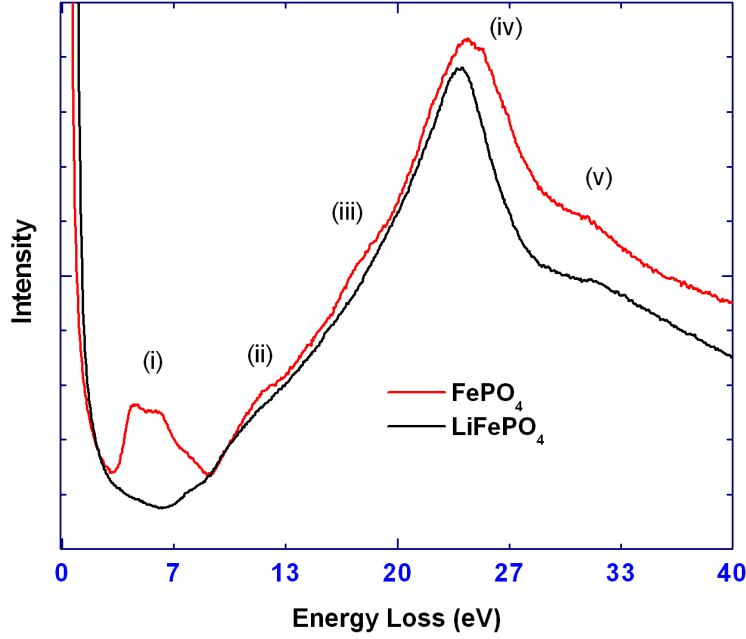


Figure 6.1: Valence loss spectrum for  $\text{LiFePO}_4$  (black curve), and  $\text{FePO}_4$  (red curve).

be taken into account including

1. What is the nature of the peaks ? i.e Are the observed peaks due to Cerenkov losses, volume/surface plasmons, inter-band or intra-band transitions ?
2. What is the character of the observed excitations ?
3. What do these excitations say about the electronic structure in  $\text{Li}_{(1-x)}\text{FePO}_4$  and changes with extraction of li ions?

### 6.2.2 Nature of the Observed peaks

Based on the question asked above, the first task is to distinguish what kind of excitation give rise to the observed peaks. Intra-band excitations are ignored in this case since both phases are insulators [70,72]. Considering the analysis given in Chapter 3, Cerenkov losses are observed if  $v > \frac{c_0}{n}$ . Where  $c_0$  is the velocity of light,  $v$  velocity of the electron and  $n$  is the refractive index of the material. One of the ways to reduce the effects of Cerenkov losses is to reduce the acceleration voltage in the microscope. These experiments presented here were done at 80 kV which gives a relativistic electron velocity of  $v = 1.506 \times 10^8 \text{ m/s}$ . Taking the refractive index of  $\text{LiFePO}_4$  and  $\text{FePO}_4$  to be  $\approx 1.6-1.7$  gives  $1.506 \times 10^8 \text{ m/s} < \frac{c_0}{n} = 1.87 \times 10^8 \text{ m/s}$ . Therefore it is assumed that the effects of Cerenkov losses on obtained spectra is

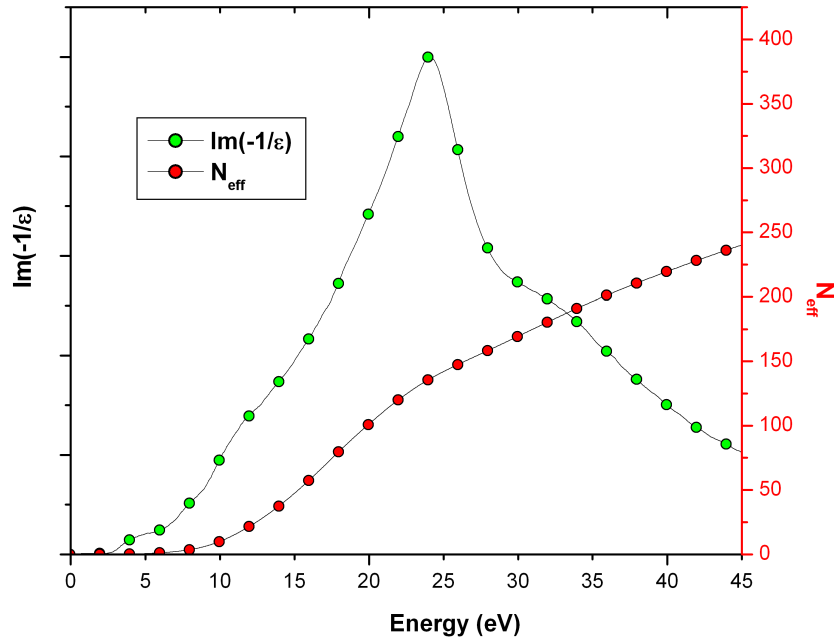
minimal. This leaves interband transitions and plasmon losses as the most likely excitations giving rise to the observed peaks. The next task is then to differentiate which of the observed peaks are plasmon peaks and which are due to interband transitions.

### $N_{\text{eff}}$ curves

The character of the transitions in the VEELS spectrum can be investigated using the effective number of electrons  $N_{\text{eff}}(E)$  participating in inter-band transitions. The quantity  $N_{\text{eff}}(E)$  can be derived from the experimental data and gives the number of valence electrons per unit cell contributing to transitions up to energy  $E$ .  $N_{\text{eff}}(E)$  can be calculated from  $\epsilon_2$  using the sum rule [60, 70, 75]

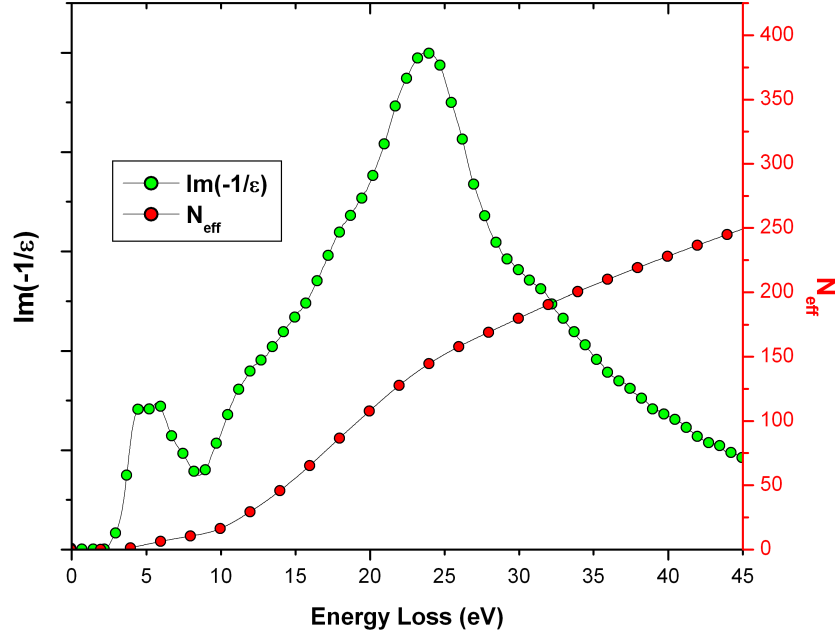
$$N_{\text{eff}} = \frac{2m}{Ne^2\hbar^2} \int_0^E E' \epsilon_2(E') dE' \quad (6.1)$$

Figure 6.2 shows the a plot of  $N_{\text{eff}}(E)$  from  $\text{LiFePO}_4$ . The  $N_{\text{eff}}(E)$  curve increases gradually between 0-20 eV indicating that this region is mainly characterized by inter-band transitions. After 20 eV the  $N_{\text{eff}}(E)$  curve is seen to saturate slightly most probably due to the onset of plasmon excitations. A new rise can be observed above the plasmon energy position of  $\approx 23$  eV due to the onset of inter-band transitions involving the deep-lying valence bands. Figure 6.3 shows the a plot of



*Figure 6.2: Number of electrons,  $N_{\text{eff}}(E)$ , involved in inter-band transitions for  $\text{LiFePO}_4$ .*

$N_{\text{eff}}(E)$  from  $\text{FePO}_4$ . The  $N_{\text{eff}}(E)$  curve increases gradually between 4-10 eV. The gradient of the curve then changes slightly and increases gradually until around 20 eV. A slight saturation of the curve is then observed. Similar to  $\text{FePO}_4$  the  $N_{\text{eff}}(E)$  curve does not saturate after the plasmon excitation due to the onset of inter-band transitions involving the deep lying valence band bands. The character



**Figure 6.3:** Number of electrons,  $N_{\text{eff}}(E)$ , involved in inter-band transitions for  $\text{FePO}_4$ .

of the  $N_{\text{eff}}(E)$  curves for  $\text{LiFePO}_4$  and  $\text{FePO}_4$  indicate that the energy region between 0-20 eV is mainly characterized by inter-band transitions. This analysis can be confirmed by looking at the behavior of the dielectric functions  $\epsilon_1$ ,  $\epsilon_2$ , and the energy loss function  $\text{Im}(-1/\epsilon(\omega))$  at this energy range

### Analysis of the dielectric function

To understand the procedure followed in this section, it is important to summarize the theoretical details presented in Chapter 3. As was shown, the energy loss function (ELF) which is derived from VEELS spectrum is proportional to the dielectric function  $\epsilon(\omega, q)$ . Accordingly, the measured VEELS spectrum describes the characteristics of the complex dielectric function and the local properties of the real and imaginary part of the dielectric function. From Equation 3.18 it can be seen that the dielectric function is made up of two parts, the real part of the dielectric function  $\epsilon_1$  and imaginary part of the dielectric function  $\epsilon_2$ . The real part of the

dielectric function,  $\epsilon_1$  shows the polarizability of the materials while  $\epsilon_2$  represents the absorption part of the dielectric function. The inter-band transitions are characterized by well-defined peak in the imaginary part of the dielectric function,  $\epsilon_2$ . As shown in Equation 4.25, the imaginary part of the dielectric function can be represented by a sum over all allowed interband transitions from the valence band to the conduction band multiplied by a density of states term. This relation allows the calculation of the dielectric function from bandstructure calculations. This is schematically shown in Figure 6.4 showing an interband transition from a valence state  $|v_k\rangle$  of energy  $E_{v_k}$ , to a conduction band state  $|c_k\rangle$  of energy  $E_{c_k}$ . The energy separating the two states is  $\hbar\omega$  which is provided through momentum transfer with the probing incident electron. This also means that the  $\epsilon_2$  curve

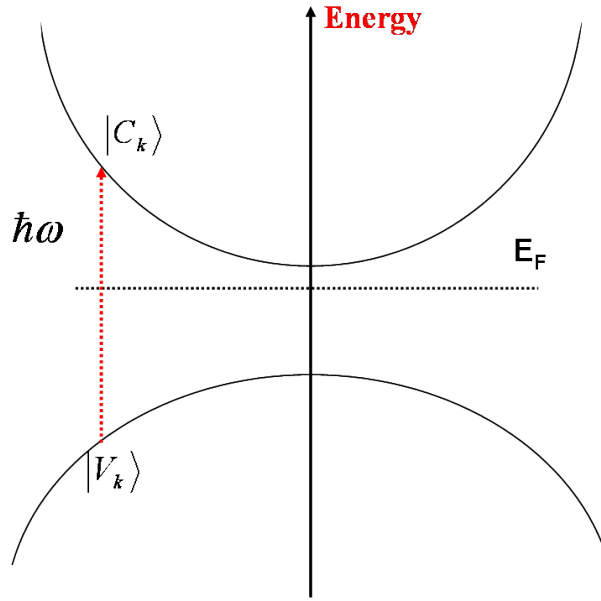


*Figure 6.4: An interband transition from the valence band  $|v_k\rangle$  to the conduction band  $|c_k\rangle$  separated by an energy  $\hbar\omega$ . The interband contribution contribute to the total intensity of the  $\epsilon_2$ .*

can also be decomposed into the various interband transitions which contribute to the its peaks. This can then be analyzed to provide information regarding the electronic structure. This is the procedure that was followed in this section. The position of the plasmon oscillations is characterized, in the real part of the dielectric function  $\epsilon_1$ , by the crossing of the abscissa axis [70]. This can be seen by looking at the limiting cases of Equation 4.23.

$$\text{Im}\left(-\frac{1}{\epsilon(q, \omega)}\right) = \frac{\epsilon_2}{(\epsilon_2^2 + \epsilon_1^2)} = \begin{cases} \frac{\epsilon_2}{|\epsilon_1^2|} & |\epsilon_1| \gg |\epsilon_2| \\ \frac{1}{|\epsilon_1^2|} & |\epsilon_1| \ll |\epsilon_2| \end{cases} \quad (6.2)$$

In the first case the large value of  $\epsilon_1$  reduces the features in the energy loss function. Thus the maxima in  $\epsilon_2$  curve are not visible in the loss function. The

most prominent peak in the energy loss function should appear when  $\epsilon_1 \rightarrow 0$  and  $\epsilon_2 \rightarrow 0$ . At this energy position the condition for plasmon excitation is fulfilled. This means that the dielectric function can be used to differentiate between plasmon excitations and interband transitions.

$\text{LiFePO}_4$  and  $\text{FePO}_4$  are both orthorhombic and therefore have an anisotropic dielectric properties and it is important to check the influence of crystal anisotropy on obtained dielectric function first. The experimental spectra examined in this thesis, were obtained from polycrystalline samples. This means that the obtained energy loss and dielectric functions are a complex mixture of individual components of the dielectric function. It was therefore not possible to investigate the anisotropy of the VEELS in  $\text{LiFePO}_4$  and  $\text{FePO}_4$  experimentally. However the effects of anisotropy on the spectra can be investigated from calculated spectra. Figure 6.5 shows the  $\epsilon_1$  and  $\epsilon_2$  for  $\text{LiFePO}_4$  and  $\text{FePO}_4$ . The curves shows the effects of anisotropy on the dielectric function in

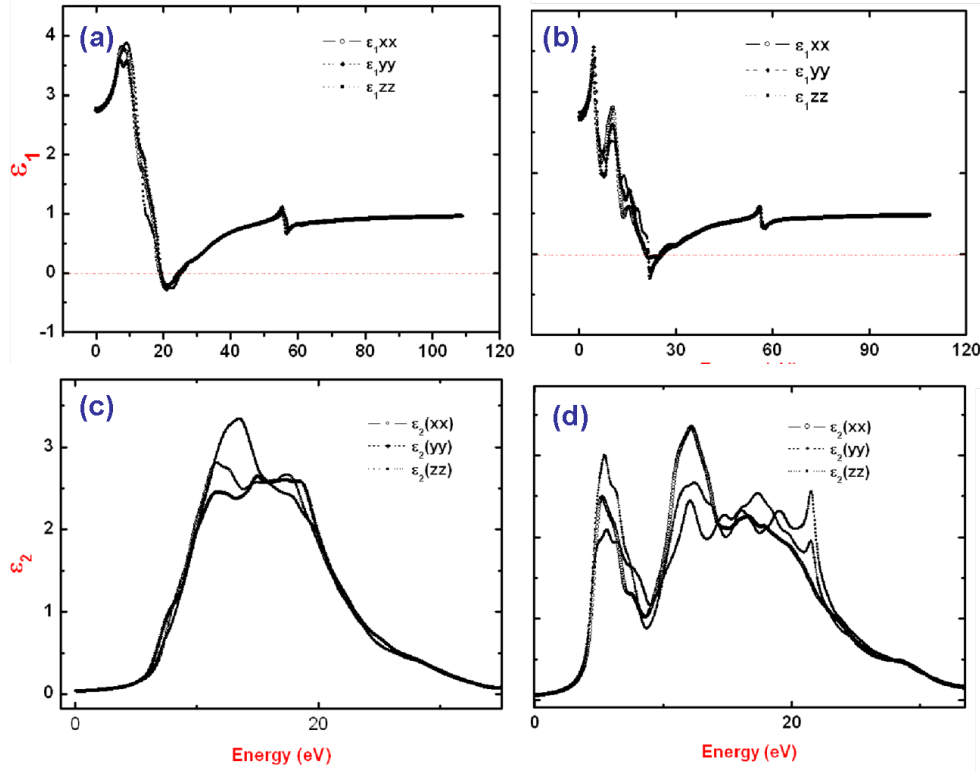


*Figure 6.5: The anisotropy of the calculated (a) , (b)  $\epsilon_1$  and (c) , (d)  $\epsilon_2$  for  $\text{LiFePO}_4$  and  $\text{FePO}_4$  respectively. The curves  $\epsilon_{xx}$ ,  $\epsilon_{yy}$ , and  $\epsilon_{zz}$  correspond to the crystallographic directions  $a$ ,  $b$ , and  $c$  respectively*

which case the intensities of certain peak features will vary depending on the crystal orientation. However, these anisotropic effects are not severe since all main peak features are reproduced independent of the crystal orientation. These curves show also that the differences between  $\text{LiFePO}_4$  and  $\text{FePO}_4$  curves is not dependent on the orientation. This means that the calculated curves can be used in

principle to interpret the features observed in the experimental spectrum.

Figure 6.6 shows the experimentally derived energy loss function  $\text{Im}(1/(\epsilon))$ ,  $\epsilon_1$ , and  $\epsilon_2$  for  $\text{LiFePO}_4$ . Figure 6.7 shows the calculated energy loss function  $\text{Im}(1/(\epsilon))$ ,  $\epsilon_1$ , and  $\epsilon_2$  for  $\text{LiFePO}_4$ . Comparing the  $\epsilon_1$  curve in both experimental

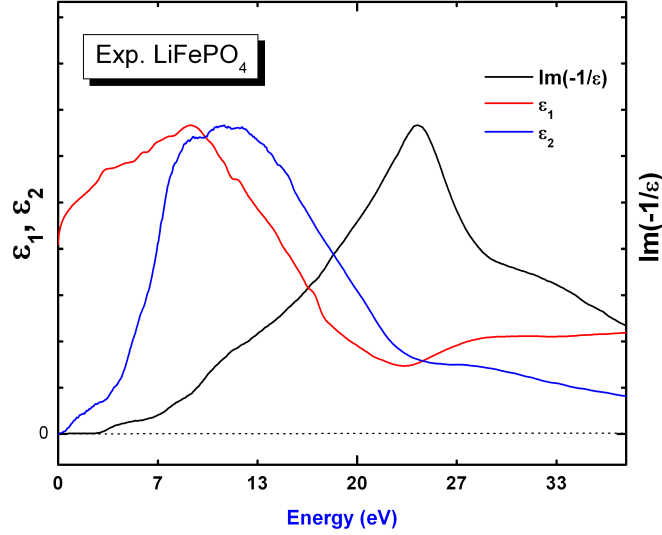


*Figure 6.6: Experimental  $\text{Im}(1/(\epsilon))$  (black curve),  $\epsilon_1$  (red curve),  $\epsilon_2$  (blue curve) loss spectrum for  $\text{LiFePO}_4$ .*

and calculated curves shows that the experimental curve does not cut the energy axis while the calculated spectra cuts the energy axis. In both sets of spectra, the  $\epsilon_1$  and  $\text{Im}(1/(\epsilon))$  are mostly featureless. In the calculated spectra it can be seen that the  $\epsilon_1$  curve cuts the energy axis with a positive slope at around 25 eV. As the  $\epsilon_1$  cuts the energy axis the  $\epsilon_2$  decreases towards zero. This is the condition for the plasmon excitation. The onset of  $\epsilon_2$  is approximately 2.7 eV which should correspond to the band-gap of  $\text{LiFePO}_4$ . The band-gap value obtained from optical experiments is 3.2 eV [45]. The discrepancy in these two values could arise due to the errors arising during the subtraction of the zero-loss peak from the VEELS spectra and the KKA analysis. This could also be one of the reasons why the experimental  $\epsilon_1$  does not cut the energy axis. Figure 6.8 shows the experimentally derived energy loss function  $\text{Im}(1/(\epsilon))$ ,  $\epsilon_1$ , and  $\epsilon_2$  for  $\text{FePO}_4$ . The calculated energy loss function  $\text{Im}(1/(\epsilon))$ ,  $\epsilon_1$ , and  $\epsilon_2$  for  $\text{FePO}_4$  are shown in Figure 6.9. Similar to the  $\text{LiFePO}_4$  curves the experimental and theoretical curves for  $\text{FePO}_4$  show very good agreement. The most apparent difference between the  $\text{FePO}_4$  and  $\text{LiFePO}_4$  spectra is in the energy regions between 4-8 eV and 12-17 eV where  $\text{FePO}_4$  shows peaks which are absent in  $\text{LiFePO}_4$ . In the  $\epsilon_2$  curve, it is seen that there is strong region of absorption between 3 eV and 7 eV after which the  $\epsilon_2$  curve decreases sharply between 8 eV and 12 eV. The curve



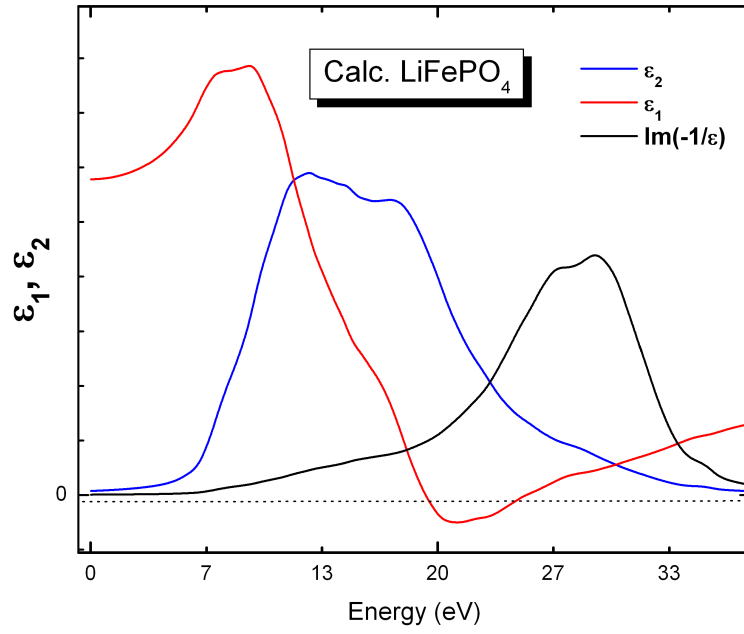


Figure 6.7: Calculated  $\text{Im}(1/(\epsilon))$  (black curve),  $\epsilon_1$  (red curve),  $\epsilon_2$  (blue curve) loss spectrum for  $\text{LiFePO}_4$ .

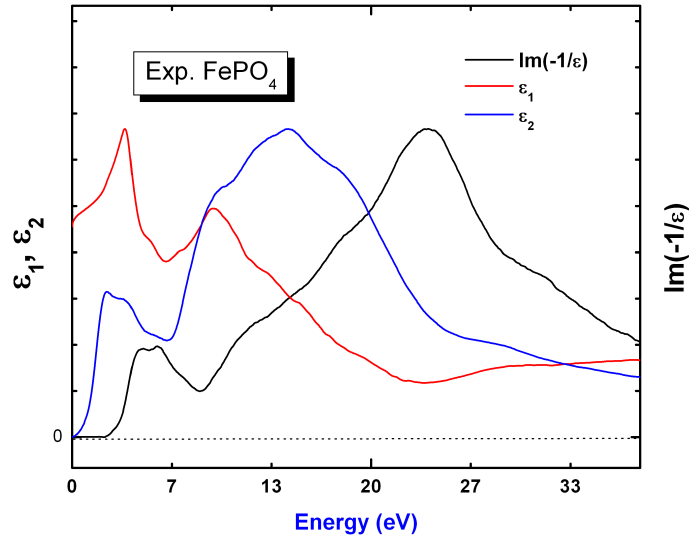
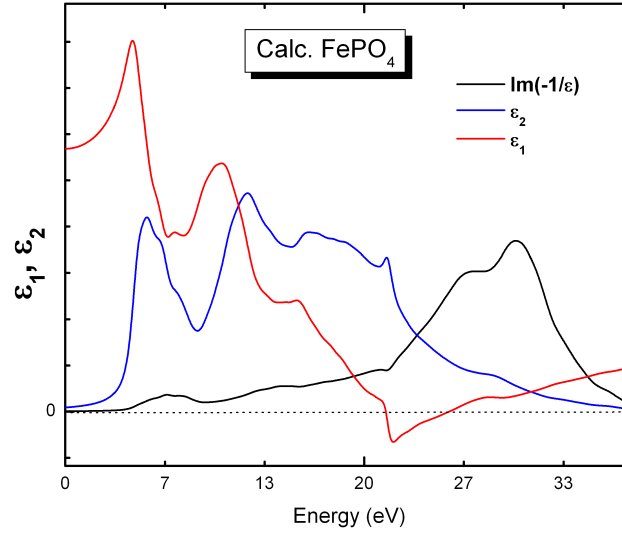


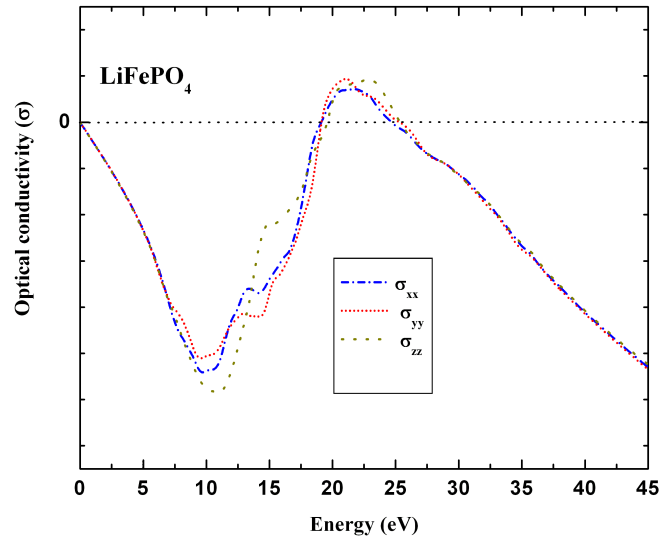
Figure 6.8: Experimental  $\text{Im}(1/(\epsilon))$  (black curve),  $\epsilon_1$  (red curve),  $\epsilon_2$  (blue curve) loss spectrum for  $\text{FePO}_4$ .

then shows a region of strong absorption between 12 and 16 eV. The curve then decreases towards zero with some small peaks between 16 and 20 eV. The  $\epsilon_1$  curve crosses the energy axis with a positive slope at 25 eV which corresponds to the position of the plasmon peak for  $\text{FePO}_4$ . Similar to the experimental spectra the position of the plasmon peak does not differ significantly between the two phases. As shown in Equations 3.20 and 3.21 the dielectric function can also be expressed

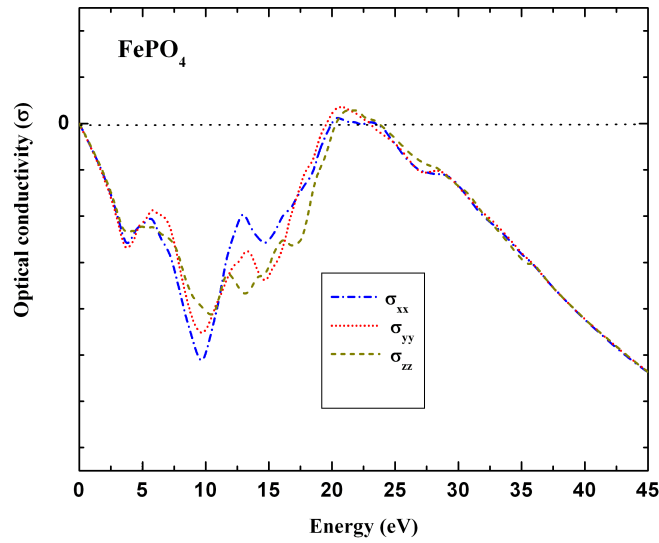


**Figure 6.9:** Calculated  $\text{Im}(1/(\epsilon))$  (black curve),  $\epsilon_1$  (red curve),  $\epsilon_2$  (blue curve) loss spectrum for  $\text{FePO}_4$ .

in terms of optical absorption. Figures 6.10(a), 6.10(b), 6.11(a), and 6.11(b) show the calculated/experimental imaginary and real parts of the optical absorption for  $\text{LiFePO}_4$  and  $\text{FePO}_4$  respectively. The information contained in the imaginary and real parts of the optical absorption can be considered to be equivalent to the one obtained from the dielectric functions  $\epsilon_1$  and  $\epsilon_2$  respectively (see equation refeq:conductivity2). However one of the curves may show more details than the other and as such it is helpful to examine both curves. Similar to the dielectric function the real part of the optical absorption gives information regarding the interband transitions. The  $(\sigma(\omega))$  curve has been calculated for the three cartesian directions,  $(\sigma(\omega)_{xx})$ ,  $(\sigma(\omega)_{yy})$ , and  $(\sigma(\omega)_{zz})$ . The real  $(\sigma(\omega))$  curve for  $\text{LiFePO}_4$  (Figure 6.11(a)) is mainly featureless in the energy region 0-20 eV. This is similar to the behavior observed for the  $\epsilon_2$  curve. The real  $(\sigma(\omega))$  curve for  $\text{FePO}_4$  on the other hand does show some peak features in this energy range (Figure 6.11(b)). The letters  $A_1, A_2, A_3, A_4$  mark the energy regions of the observable peak features. Looking at the calculated spectra, it can be seen that the peak feature  $A_1$  is missing from the  $\text{LiFePO}_4$  spectra, however it is observed in  $\text{FePO}_4$ . From the images it can be seen that peak feature  $A_1$  does not show strong anisotropic characteristics. This



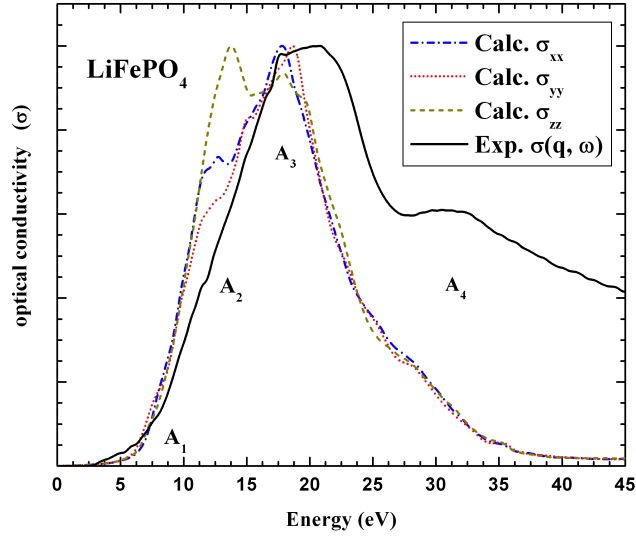
(a)



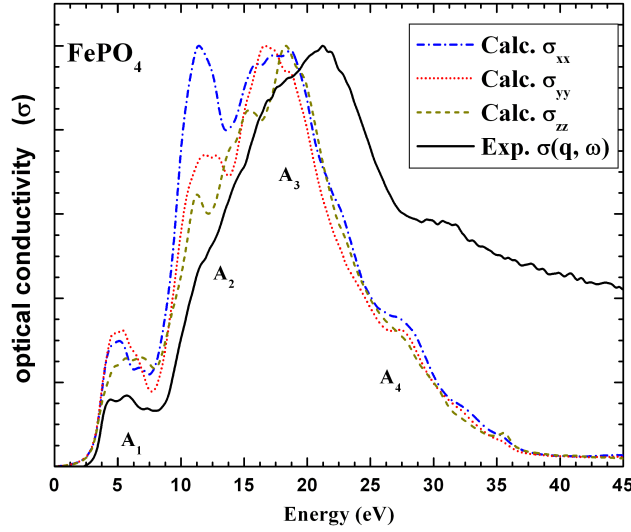
(b)

**Figure 6.10:** Calculated imaginary part of the optical conductivity ( $\sigma(\omega)$ ) for (a)  $\text{LiFePO}_4$  (b)  $\text{FePO}_4$  shown for the three cartesian co-ordinates.

means that the peak is reproduced in all major crystal directions. features. Peak features  $A_2$  on the other hand shows strong anisotropy. In experimental  $\text{LiFePO}_4$  and  $\text{FePO}_4$  spectra the peak feature  $A_2$  appears as a small shoulder. This could be attributed to the fact that the experimental spectra was obtained from poly-



(a)



(b)

**Figure 6.11:** Calculated and experimental real optical conductivity ( $\sigma(\omega)$ ) for (a)  $\text{LiFePO}_4$  (b)  $\text{FePO}_4$ . The ( $\sigma(\omega)$ ) was calculated for the three main cartesian coordinates ( $\sigma(\omega)_{xx}$ ), ( $\sigma(\omega)_{yy}$ ), ( $\sigma(\omega)_{zz}$ ). The letters  $A_1, A_2, A_3, A_4$  mark the energy regions of the observed peak features

crystalline samples and therefore the anisotropic effects cannot be seen from the spectra. Peak features  $A_3$  and  $A_4$  are observed in both phases and show very little anisotropy. It can also be seen that there is a slight disagreement in some peak

positions between the calculated and experimental  $\sigma(\omega)$  curves. This is especially more apparent in the higher energy regions. The disagreement in absolute peak positions in calculated spectra is a well known weakness of the DFT method. In many case the spectra have to be shifted manually in order to fit the experiment. However the peak features observed in the experimental curves have been very well reproduced in the calculated curve.

From the analysis presented in the above sections the peaks observed in Figure 6.1 can then be classified into either plasmon or inter-band transitions. These are presented in the table 6.1. The  $A_1$ ,  $A_2$ ,  $A_3$ ,  $A_4$ , peaks observed in the real

*Table 6.1: Classification of the peaks observed in the experimental VEELS spectra for  $\text{FePO}_4$  (Figure 6.4)*

Peak	Peak position (eV)	Type of excitation
peak (i)	2 eV	inter-band transition
peak (ii)	12 eV	interband transition
peak (iii)	17 eV	inter-band transition
peak (iv)	23 eV	plasmon peak
peak (v)	30 eV	core-transition

conductivity curve of  $\text{FePO}_4$  (Figure 6.11(b)) correspond to the peaks (i), (ii), (iii) and (v) observed in the ELF (Figure ??) and  $\epsilon_2$  (Figures 6.8 and 6.9). Since the nature of features in the experimental data is now identified, the task remains to find out the character of these inter-band transitions and plasmon excitation and the information they provide regarding the delithiation process in  $\text{LiFePO}_4$ .

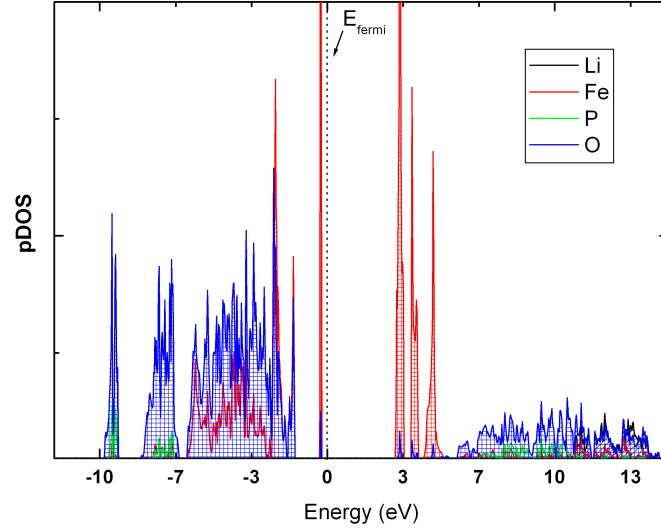
### 6.2.3 Character and the origin of the observed excitations

In order to understand the character and the origin of the features observed in  $\text{FePO}_4$  and  $\text{LiFePO}_4$  spectra it is necessary to also calculate the electronic and bandstructure of both phases.

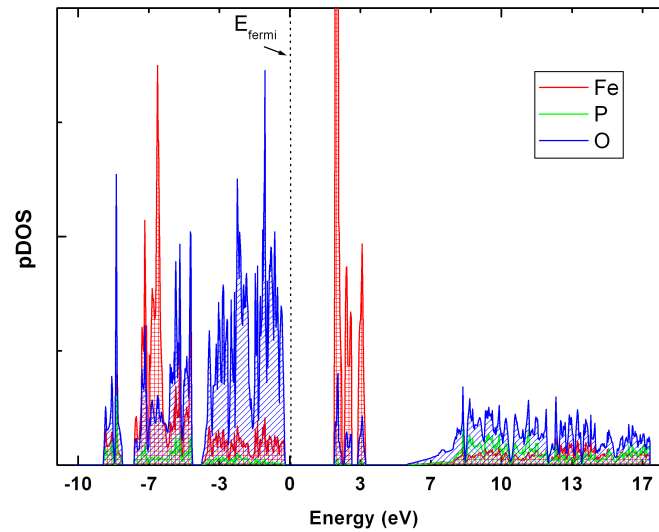
#### Electronic structures of $\text{LiFePO}_4$ and $\text{FePO}_4$

The total DOS and the contributions from Li, P, O and Fe to the total density of states for  $\text{LiFePO}_4$  and  $\text{FePO}_4$  are presented in Figures 6.12(a) and 6.12(b). Figure 6.12(a) shows the total DOS and partial DOS for Li, Fe, P, O in  $\text{LiFePO}_4$ . The partial density of states for lithium, iron, oxygen and phosphorous are shown by the black, blue, red and green curves respectively. The O-2p states are mixed with P-3p states in the lower two sets of bands and with Fe 3d states in the energy range between -7 eV and -0.5 eV. The Fe 3d states in the valence band are between 4 -7 eV. Above 7 eV, the DOS is dominated by the Li-2s Fe-4s and 4p states and

P-4s. A narrow band mainly with Fe 3d character and some O 2p contribution is seen between -0.5/0 eV.



(a)



(b)

**Figure 6.12:** Partial density of states (pDOS) for Li(black curve), Fe (red curve), O (blue curve) and P (green curve) for (a)  $\text{LiFePO}_4$  (b)  $\text{FePO}_4$

Figure 6.12(b) shows the total DOS and partial density of states for Fe, P, and O atoms for  $\text{FePO}_4$ . The partial density of states for iron, oxygen and phosphorous are shown by the blue, red and green curves respectively. The partial density of

states shows that the valence band near the  $E_F$  is mainly oxygen in character with some iron mixing and phosphorus contributions as a result of covalent interactions. Similar to  $\text{LiFePO}_4$ , the bottom of the valence band (-9/-4 eV) originates from the bonding states of the sub unit  $\text{PO}_4$ . The DOS associated with the  $\text{PO}_4$  units constitutes well separated  $a_1$  and  $t_2$  levels as a result of the tetrahedral symmetry. The second Fe 3d band is shifted lower in energy and is observed at around -7 eV. There are several differences in the density of states for  $\text{LiFePO}_4$  and  $\text{FePO}_4$ .

Figures 6.13 and 6.14 show the band structure for  $\text{LiFePO}_4$  and  $\text{FePO}_4$  respectively. In both cases the plotted are characterized by colored circles. These circles represent Fe 3d and O 2p character of each respective band. The Fe-3d or O 2p character is represented by the radius of the coloured circle. The larger the radius of the circle the more Fe 3d or O 2p character a band shows. Figure 6.13(a) shows the Fe 3d character of the bands while Figure 6.13(b) shows the O-2p character of the bands in  $\text{LiFePO}_4$ . The information provided by the bandstructure plots for  $\text{LiFePO}_4$  is similar to the one given for the DOS. It can be clearly seen that in  $\text{LiFePO}_4$  the Fe 3d bands in the valence band are found between -2.1/0 eV. The Fe 3d bands in the conduction band are overlapping with the main levels and are found between 3-6 eV.

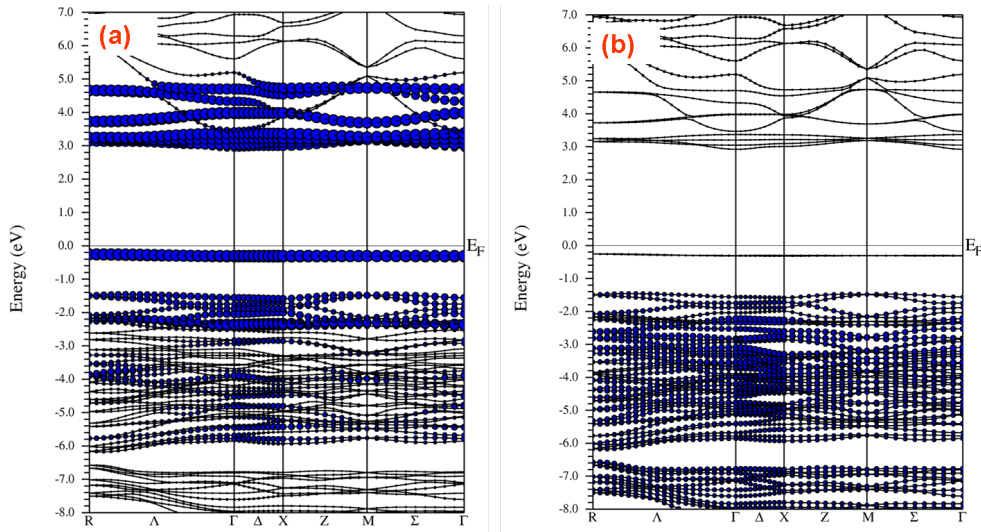


*Figure 6.13: Band structure of  $\text{LiFePO}_4$  showing (a) Fe 3d character (b) O 2p character of the bands between -9 eV/ 9eV. The radius of the colored circle represents the degree of respective character in a band.*

Figure 6.14(a) and Figure 6.14(b) show the Fe 3d and O 2p characters of bands in  $\text{FePO}_4$  respectively. The changes in the electronic structure with delithiation can be clearly seen. It can be seen that in  $\text{FePO}_4$  the Fe 3d bands in the valence band are shifted to lower energies and now found between -7.0/-6.0 eV. The Fe 3d bands in the conduction band are also shifted downward in energy and are no longer overlapping with the main levels. They are now found between 2-3 eV. The valence states near the  $E_F$  are now dominated by O 2p states.

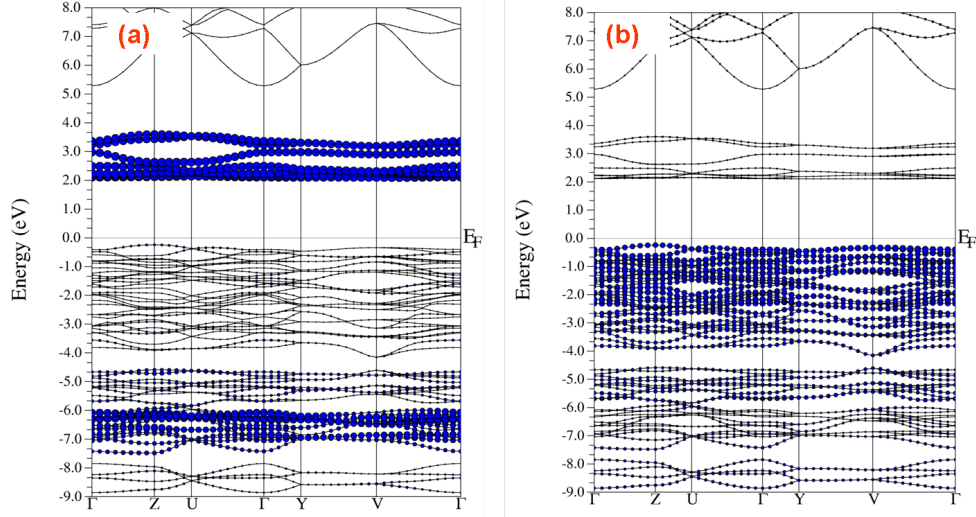


**Figure 6.14:** Band structure of  $\text{FePO}_4$  showing (a) Fe 3d character (b) O 2p character of the bands between -9 eV/ 9eV. The radius of the colored circle represents the degree of respective character in a band.

From chapter 2 it was shown that the  $\text{Fe}^{2+}$  ion in  $\text{LiFePO}_4$  has a  $t_{2g}(\uparrow)^3 e_g(\uparrow)^2 t_{2g}(\downarrow)^1$  electronic configuration. The  $\text{Fe}^{3+}$  ion in  $\text{FePO}_4$  has a configuration of  $t_{2g}(\uparrow)^3 e_g(\uparrow)^2$ . Since the Fe ion in  $\text{LiFePO}_4$  has an extra electron an additional Fe 3d band is filled ( between -0.5/0 eV in Figure 6.12(a) and 6.13(a)). This Fe 3d band then forms what is known as lower Hubbard band. The Fe 3d bands in the valence band are found between 4-7 eV. Which means they are closer to the main energy levels than in  $\text{FePO}_4$ . These upper Fe 3d bands form the upper Hubbard bands. This means that  $\text{LiFePO}_4$  is most likely to be a Mott-Hubbard insulator. In  $\text{FePO}_4$  the Fe 3d band between -7 eV (Figure 6.12(b) and 6.14(a)) forms the lower Hubbard band. The states at the Fermi level are mainly O 2p states. The Fe 3d bands in the conduction band are well separated from the main energy levels. These Fe 3d bands then form the upper Hubbard band. Contrary to  $\text{LiFePO}_4$ ,  $\text{FePO}_4$  appears to be a charge-transfer insulator.

### Origin and character of the observed interband-transitions

From the analysis presented in the previous section it was shown that the peaks observed between 0-20 eV in  $\text{FePO}_4$  spectra are due to interband transitions from the valence band to the conduction band. Taking the calculated electronic structure and dielectric functions into consideration it is now possible to assign the interband transitions and their character. This is done through the band-by-band analysis of the  $\epsilon_2$  for  $\text{FePO}_4$  and  $\text{LiFePO}_4$ . In this case the valence band is then divided into several energy ranges and the interband transitions from the bands in these energy ranges to the conduction band are used to calculate partial  $\epsilon_2$  curves which can then be compared with the experimental and calculated full



$\epsilon_2$  curves. Figure 6.15 shows the partial  $\epsilon_2$  curves for  $\text{LiFePO}_4$  calculated for inter-band transitions from bands between -44 eV/-0.2 to the conduction band.

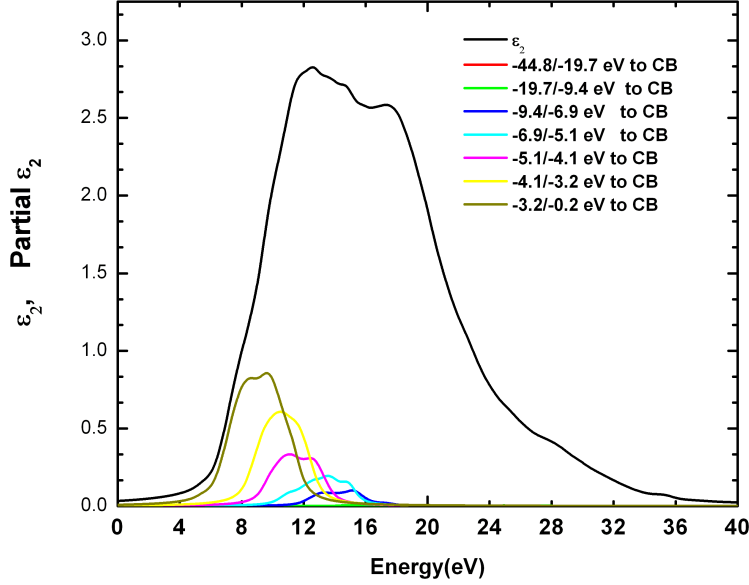


*Figure 6.15: Partial  $\epsilon_2$  calculated from selected bands in  $\text{LiFePO}_4$ . The black curve shows the calculated total  $\epsilon_2$ . The coloured curves shows the partial  $\epsilon_2$  calculated for transitions involving bands -44.8/-19.7 eV to the conduction band (CB), -19.7/-9.4 eV to CB, -9.4/-6.9 eV to CB, -6.9/-5.1 eV to CB, -5.1/-4.1 eV to CB, -4.1/-3.2 eV to CB, -3.2/-0.2 eV to CB*

The shape obtained from the partial  $\epsilon$  in  $\text{LiFePO}_4$  mimics the shape of the conduction band. As can be seen in the DOS in figure 6.12(a) the upper Hubbard band is shifted upwards in the energy and is overlapping with the main energy levels above 7 eV. Interband transitions to these states that very close in energy results in the  $\epsilon_2$  being almost featureless due to the averaging out of the transitions. This could explain why the  $\epsilon_2$  curve for  $\text{LiFePO}_4$  is almost featureless.

Figure 6.16 shows the partial  $\epsilon_2$  curves for  $\text{FePO}_4$  calculated for inter-band transitions from bands between -20.5 eV/-0.2 to the conduction band. The partial  $\epsilon_2$  for  $\text{FePO}_4$  show a very different picture. It can be seen that the partial  $\epsilon$  for  $\text{FePO}_4$  show the same features: a well defined first peak which is then followed by a second peak at least 7 eV higher in energy (for example the 3 eV and 11 eV for the gold curve in Figure 6.16). Both peaks are well separated from each other. This peak shape mimics the shape of the conduction band where levels created by the Fe 3d states (upper Hubbard Band around 2 eV) are well separated from higher energy levels (above 7 eV)(this can be seen by comparing Figures 6.12(b) and 6.16). The progressive decrease of intensity (from gold to the red curve) is as a result of decrease in the valence band-conduction band oscillator strengths

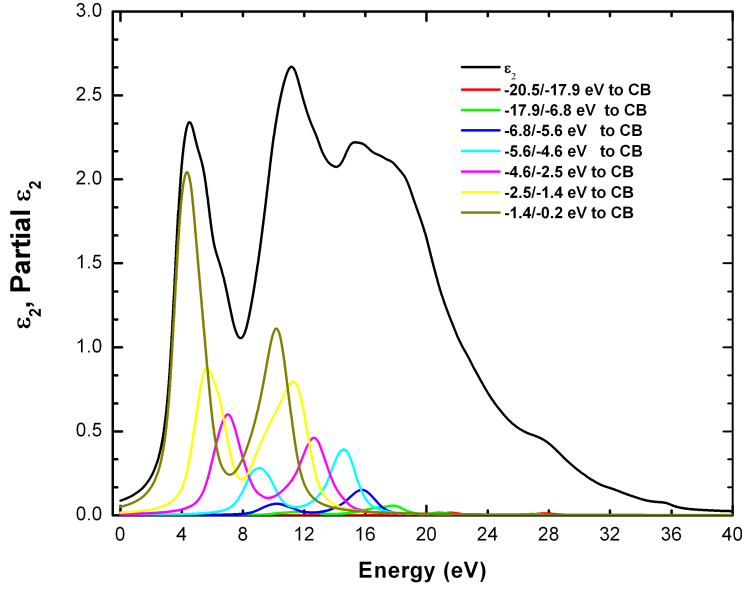


*Figure 6.16: Partial  $\epsilon_2$  calculated from selected bands in  $\text{FePO}_4$ . The black curve shows the calculated total  $\epsilon_2$ . The coloured curves show the partial  $\epsilon_2$  calculated for transitions involving bands -20.5/-17.9 eV to the conduction band, -17.9/-6.8 eV to CB, -6.8/-5.6 eV to CB, -5.6/-4.6 eV to CB, -4.6/-2.5 eV to CB, -2.5/-1.4 eV to CB, -1.4/-0.2 eV to CB*

originates from the lower valence band-conduction band oscillator strengths as the energy separation between initial and final states increases. Another consequence of the decrease in the oscillator strength is that the first peak intensity decreases with respect to higher energy peaks. The interband transitions responsible for the peaks observed in the energy range 0-20 eV in  $\text{FePO}_4$  are therefore due to transitions from the mainly O 2p bands in the conduction band to the upper Hubbard band in the valence band. This could there be seen as charge transfer transitions in a charge-transfer insulator

### Origin and character of the observed plasmon excitations

From the analysis in the previous section it was shown that the intense peak labeled as peak (iv) in the experimental spectra (6.1) is due to the volume plasmon peak. As shown in Chapter 3, the position of the plasmon peak can be approximated using the free electron approach given by Drude or Horie approach for the semiconductors and insulators. The question now arises what number of valence electrons per  $\text{LiFePO}_4$ ,  $\text{FePO}_4$  cell have to be taken in order to calculate the density of valence electrons  $N_e$  and subsequently  $\hbar\omega_p$ . This means, which Li, Fe, P and O states can be considered to be valence states that participate in the

volume plasmon excitation. In table 6.2 the calculated free electron  $\hbar\omega_f$  and  $\hbar\omega_p$  are presented for various values of  $N_e$ . According to Liang et al [129], in narrow band semiconductors in which all filled bands ( $l$ ) other than the top valence band ( $l < v$ ) are well removed from both the highest valence band  $v$  and the conduction band  $c$ , such that  $\omega_{cv} < \omega_p \ll \omega_{cl}$ . The energy of the plasma resonance is approximately that for the free electron. However, in a semiconductor in which the valence band is made up of two separate groups  $v$  and  $u$  ( $v > u$ ), plasma resonances can be found arising from

- Valence electrons from both bands giving the plasma resonance frequency of

$$\omega_{p^2}^2 = 4\pi N_e e^2 \left( \frac{n_v + n_u}{m} \right) \quad (6.3)$$

- Valence electrons from the highest valence band only.

*Table 6.2: Plasmon energies  $\hbar\omega_f$  and  $\hbar\omega_p$  for different  $N_e$  values in  $\text{LiFePO}_4$*

States included in the valence	$N_e$	$\hbar\omega_f$	$\hbar\omega_p$
4xLi (2s) <sup>1</sup> , 4xFe (3d) <sup>6</sup> (4s) <sup>2</sup> , 4xP(3p) <sup>3</sup> , 16xO(2p) <sup>4</sup>	112	23 eV	23.19 eV
4xLi(1s) <sup>2</sup> (2s) <sup>1</sup> , 4xFe (3d) <sup>6</sup> (4s) <sup>2</sup> , 4xP(3s) <sup>2</sup> (3p) <sup>3</sup> , 16xO(2p) <sup>4</sup>	128	24.6 eV	24.8

Referring band-structures shown in the Figures 6.13 and 6.14, it can be seen that  $\text{LiFePO}_4$  has three bands in the valence region which lie between Fermi level ( $E_F$ ) and -8 eV.  $\text{FePO}_4$  has two broad bands in the valence region. From the DOS it can be seen that these bands have a majority of  $\text{O}(2p^4)\text{Fe}(3d^6/3d^5)$  character but they also contain contributions from  $\text{Li} - (2s^1), \text{P}(3p^3)$  semi-core states. Considering that there are 4 Fe, 4 Li 4 P and 16 atoms in a  $\text{LiFePO}_4$  unit cell give a total of 112 electrons in the valence region. From Table 6.2 it can be seen that the experimental value of the plasmon peak is given by a total of 112 electrons. Both Drude and Hourie formula give a plasmon peak energy that is very close to the experimental value. This calculation also confirm the first assumption that the peak (iv) is due to plasmon excitations.

### 6.2.4 Implications for the delithiation process

The results obtained from the VEELS spectra and bandstructure calculations point towards an extensive re-organization of the electronic structure with delithiation. These results can be summarized using the schematic presented in Figures 6.17(a) and 6.17(b).

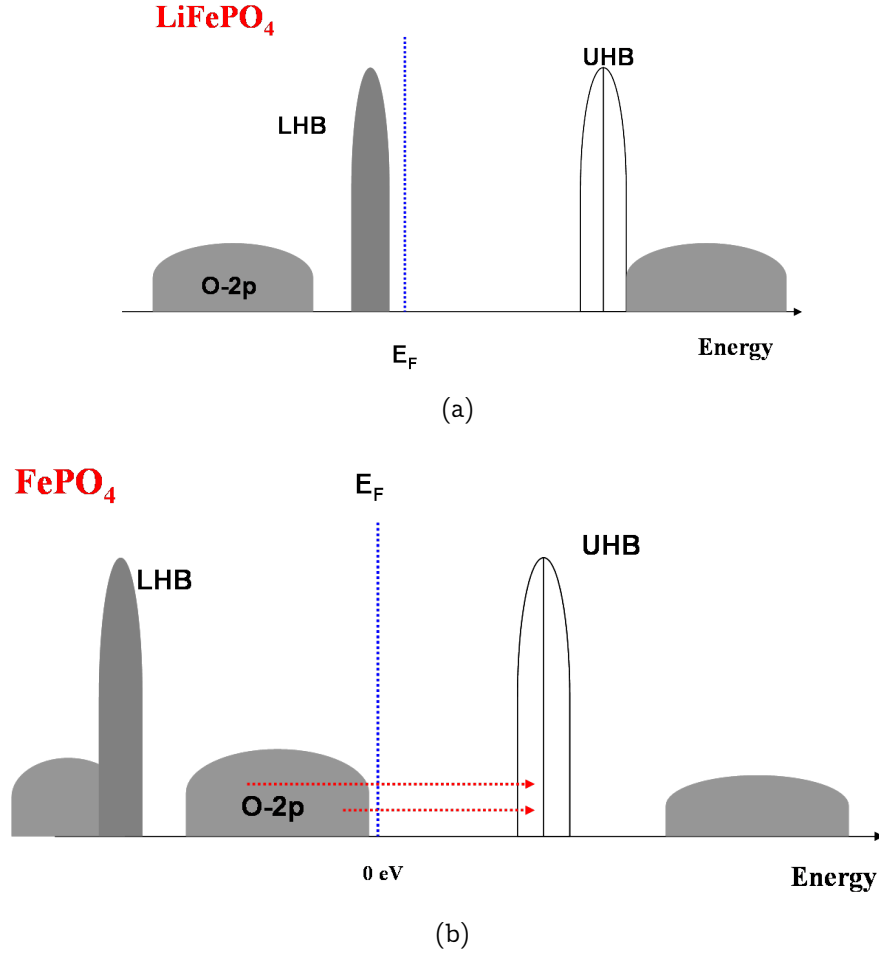


**Figure 6.17:** A schematic picture for the changes in the electronic structure with delithiation. (a)  $\text{LiFePO}_4$  can be considered to be Mott-Hubbard insulator (b)  $\text{FePO}_4$  can be considered to be charge-transfer insulator. LHB represents the lower Hubbard band and UHB represents the upper Hubbard band. The red arrows indicate the possible interband transitions observed in the VEELS spectra of  $\text{FePO}_4$

Figure 6.17(a) presents a schematic of the DOS for  $\text{LiFePO}_4$  obtained from calculated DOS and VEELS spectra. The obtained results indicate that  $\text{LiFePO}_4$  is possibly a Mott-Hubbard insulator with the LHB found between -0.5 and 0 eV and UHB found between 4 and 7 eV. Figure 6.17(b) presents a schematic of the DOS for  $\text{FePO}_4$  obtained from calculated DOS and VEELS spectra. Extraction of lithium ions results in a downward shift of the UHB to around 2 eV and LHB to between around -7 eV in  $\text{FePO}_4$ . The shift of the UHB band to lower energy means

that the UHB is well separated from the other energy levels in the conduction band. This change in the electronic structure is then reflected in the VEELS spectra of  $\text{FePO}_4$ . The observed interband transitions in  $\text{FePO}_4$  shown with the red arrow in Figure 6.17(b) involve transitions from the O 2p dominated states near the Fermi level to the UHB in the conduction band. The VEELS spectra shows characteristic peaks at 4-20 eV in the delithiated  $\text{FePO}_4$  phase. These characteristic peaks are either missing or are less intense in the  $\text{LiFePO}_4$  VEELS spectra. Analysis of the derived  $\epsilon_1$  and  $\epsilon_2$  show that these peaks are due to interband transitions. Band-by-band analysis of the  $\epsilon_2$  curve show that these peaks are due to interband transitions arising from the bands at the top of the valence band to the unoccupied bands in the conduction band. From bandstructure calculation it is shown that the energy states at the top of the valence band in  $\text{FePO}_4$  are mainly O-2p states and the states at the bottom of the conduction band are mainly Fe-3d states. Therefore interband transitions that characterize the VEELS spectra of  $\text{FePO}_4$  involve mainly transitions from bands with a O 2p character to bands with a Fe 3d character in the conduction band.



## Core-loss Spectra in $\text{Li}_{(1-x)}\text{FePO}_4$

This chapter focuses on core-loss EELS spectra. As introduced in Chap. 3, core-loss EELS involves the excitation of deep lying core-shell electrons into the unoccupied bands. For example the K edge is due to the excitation of the 1s electrons to the 2p states in the unoccupied bands. The 1s electron core states are found several hundred eV below the Fermi energy. This is in contrast with VEELS which involves excitations from the valence band found only a few eV from the Fermi Level. However the information provided by both methods should be same as they both probe the unoccupied density of states. After introduction and experimental In order to interpret VEELS theoretical calculations are often necessary. Experimental and calculation details are given in Sec.7.1, Sec.7.2 respectively . The results obtained are discussed in terms of the nature, character and origin of the observed core EELS excitations which are given in more details in Sec. 7.3. The chapter concludes by outlining what core-loss EELS spectra ( and the associated calculations) reveal about the electronic structure changes with delithiation.

### 7.1 Introduction

From the VEELS and bandstructure results shown in the Chapter ??, it was shown that the extraction of lithium ions from the  $\text{LiFePO}_4$  lattice is accompanied by extensive changes in the electronic structure. Two major conclusion could be made based on these results including

- Delithiation is accompanied by a shift of the Fe 3d bands in the valence (LHB) and conduction band (UHB) to lower energies

- delithiation is characterized by increased hybridization between Fe 3d-O2p states

As a result it was argued that  $\text{LiFePO}_4$  could be characterized as Mott-Hubbard insulator and  $\text{FePO}_4$  as charge-transfer insulator. Core-loss EELS provides a means to confirm these conclusions. As presented in Chapter 3, both VEELS and core-loss EELS probe the unoccupied states in the conduction band. Both spectroscopy methods probe the unoccupied electronic states in the conduction band. The key difference being that core EELS spectra involves the study of electronic structure through the excitation of core-shell electrons into the conduction band while VEELS involves electronic excitations between the valence and the conduction bands. In addition VEELS spectra is also characterized by excitations which are not observed in core EELS. These include energy losses due to the collective excitation of the valence electrons (plasmons), lattice vibrations (phonons), intra-band transitions and relativistic losses (Cherenkov losses) which are not observed in core EELS. However the information provided by both sets of spectra should be equivalent since they both probe the unoccupied states in the valence band. This is particularly the case with core-loss EELS from the the O-K and  $\text{FeL}_{2,3}$  edges. The O-K and  $\text{FeL}_{2,3}$  probe the unoccupied O-2p and Fe 3d states respectively. It was shown using VEELS that the most important changes in the electronic structure involve the O 2p and Fe 3d unoccupied states in the conduction band respectively.

## 7.2 Experimental and calculation details

The core-edges in  $\text{LiFePO}_4$  and  $\text{FePO}_4$  including Li-k, Fe  $M_{2,3}$  (55-57 eV), O K (532 eV) edge and  $\text{FeL}_{2,3}$ , (708, 720 eV) were all acquired at 80 kV. The exposure times were 3 sec. for Li-K and 8 sec. for the O-K and  $\text{FeL}_{2,3}$  edges. The spectra was corrected for the background and multiple scattering using the procedures elucidated in Chapter 3. The O-K edge was calculated within the DFT code. The core-hole effects were not taken into consideration. In order to interpret the experimental spectra of the  $\text{FeL}_{2,3}$ -edges absorption spectra, theoretical spectra were calculated using ligand field multiplet as implemented in the CTM4xas code [106,130]. This approach takes into account all the electronic-electronic interactions, spin-orbit coupling as well as the crystal field effects (as introduced in subsection 4.1.2, Chap 4). To describe the crystal field effects, ligand field splitting  $10Dq$  is used as an adjustable parameter. The charge transfer  $\Delta$  which represents the mixing between the Fe and O ligand is also used in the calculations. The calculated spectra are broadened with a Lorentzian function of width 0.2 eV for  $L_3$  and 0.4 for the  $L_2$  edge and a Gaussian function of width 0.45 eV in order to describe lifetime and instrumental broadening respectively.



## 7.3 Results and Discussion

### 7.3.1 O-K edge

Figure 7.1 shows the O-K edge plotted both for lithiated  $\text{LiFePO}_4$  and delithiated  $\text{FePO}_4$ . The O 1s spectrum is as a result of the dipole allowed transition in which a oxygen 1s electron is promoted to unoccupied 2p oxygen orbital. In a purely ionic picture the divalent oxygen ion has an electronic configuration  $1s^2 2s^2 2p^6$  and as such the O-2p states are fully occupied. Based on this view, we should not expect to see intensity arising from the 1s to 2p transition. The fact that the O-K edge is observed experimentally is a direct result of the covalency and hybridization between Fe 3d states and O 2p states [131–133].

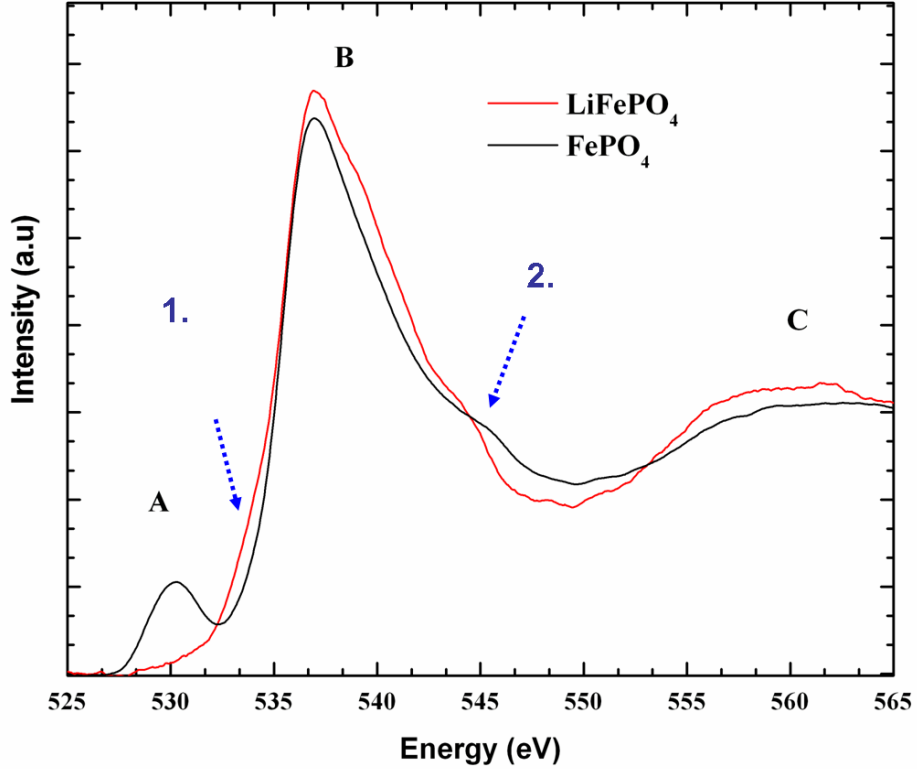


*Figure 7.1: The fine structure of the O-K edge before and after delithiation. The various peaks have been labeled as peaks A, B, C*

The features at the O-K edge are therefore good indicators of the degree of covalency between the transition metal and the oxygen atoms. The spectra are characterized by three peak features which are labeled A, B and C in the figure. The first peak which is labeled A is a pre-edge peak that appears only in the

delithiated sample and which is centred at 529 eV. The second peak which is the most prominent peak is centred at 538 eV and is labeled as peak B. The third peak feature is a broad peak observed at energies above 540 eV which is labeled as peak C. The last two peaks appear in both delithiated and undelithiated samples. The extra peak features have been marked with arrows 1 and 2. Peak 1 is a shoulder found slightly above the threshold of the O-K edge in  $\text{LiFePO}_4$ . Peak feature 2 is found on both phases spectra.

### Modelling the O-K edge

To a first approximation the  $1s \rightarrow 2p$  transitions (K edge) spectra can be considered to be a projection of the unoccupied O 2p component of the hybridized Fe-3d O-2p density of the unoccupied states. In this case theoretically calculated partial density of states (PDOS) can be used to interpret the peak features observed in the experimental and theoretical spectra [123,126]. Figure 7.2 shows the spin-up and spin-down oxygen p projected density of states (*p*PDOS) in the energy region between -10 and 20 eV for  $\text{LiFePO}_4$  and  $\text{FePO}_4$  respectively. The origin of the energy scale has been fixed at the Fermi level,  $E_f$ . The DOS of the 8 inequivalent O atoms and 16 atoms in the  $\text{LiFePO}_4$  and  $\text{FePO}_4$  supercells respectively, have been weighted and added. Differences in the DOS are clearly seen between these phases particularly in the energy states above the Fermi energy. The  $\text{FePO}_4$  *p*PDOS shows a high density of 2p states in the energy region 2-4 eV which are missing in  $\text{LiFePO}_4$ . This difference in O 2p-PDOS is reflected in the ELNES of the corresponding O-K edge and is responsible for the observed pre-edge peak in the O-K spectra of  $\text{FePO}_4$ .

As was mentioned in the section 2.1 the oxygen atom is octahedrally co-ordinated to Li and Fe, and tetrahedrally co-ordinated to the phosphorous ions in  $\text{LiFePO}_4$  and  $\text{FePO}_4$ . The oxygen atoms occupy several inequivalent sites which depend on their next neighbours. The inequivalent oxygen in  $\text{LiFePO}_4$  include are O(1)  $\rightarrow$  Li-O-Fe, O(2)  $\rightarrow$  Li-O-P, O(3)  $\rightarrow$  Fe-O-P. Figure 7.3 shows the various oxygen sites in  $\text{LiFePO}_4$  (drawn after Streltsov *et al* [11]). The inequivalent sites are similar for  $\text{FePO}_4$  with the only difference being that the Li ions are missing. Due to difference in bonding environment the electronic structure around each inequivalent atom will be different and as such inequivalent sites will contribute differently to the intensity of the core spectrum. The calculated ELNES for the various inequivalent oxygen sites in  $\text{LiFePO}_4$  and  $\text{FePO}_4$  calculation super-cells is presented in Figures 7.4(a),7.4(b)

The different coordination geometry is mirrored in the contributions of the different oxygen atoms to the total ELNES. The theoretical spectra for the inequivalent sites shows that the intensity of the pre-edge peak has some site dependence is dependent on the respective O site. To experimentally probe site dependence of the eels spectra would involve doing momentum dependent EELS experiment. This can only be done using single crystal samples. In this case the EELS spectra

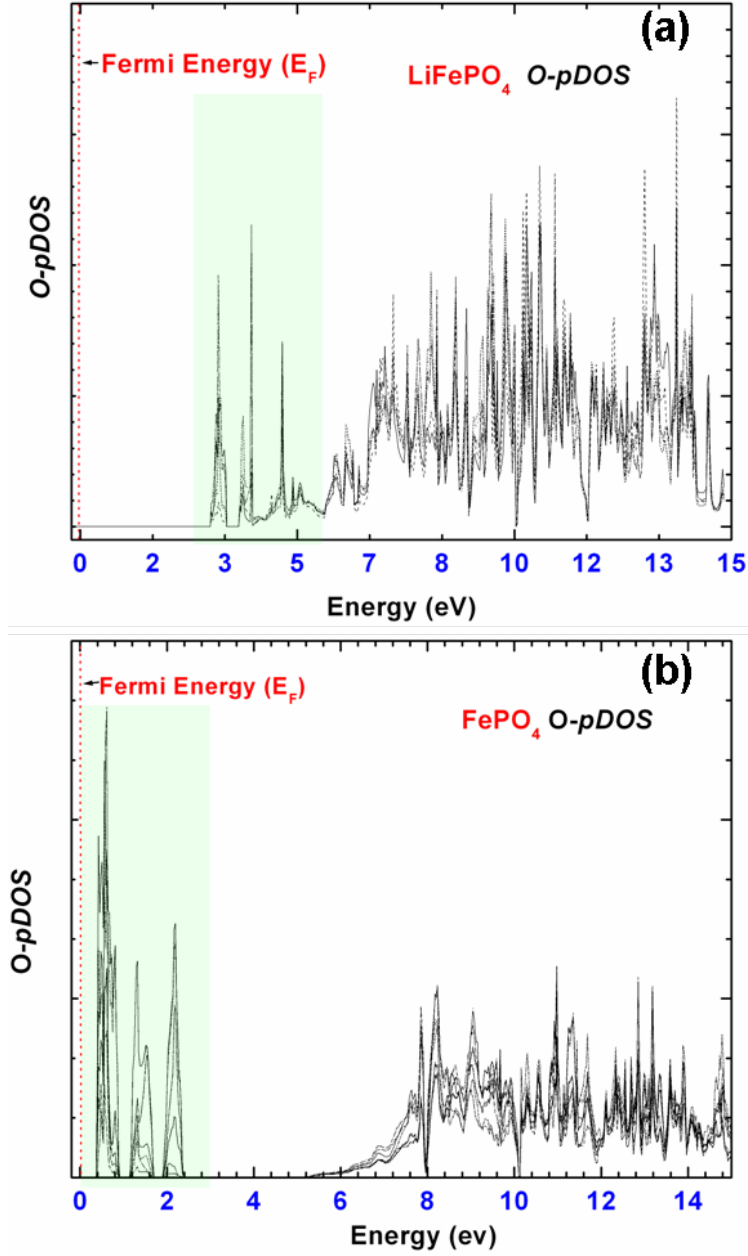


*Figure 7.2: PDOS for O states shown for (a)  $\text{LiFePO}_4$  (b)  $\text{FePO}_4$ . The major difference between the PDOS for the two phases is in the energy region 2-6 eV in the areas marked green.  $\text{FePO}_4$  the DOS is shifted to lower energies between 2-4 eV while in  $\text{LiFePO}_4$  it is shifted to higher energies between 4-6 eV*

was collected from polycrystalline samples and hence the anisotropy of the EELS spectra was not examined. In the case of polycrystalline samples the obtained experimental spectra obtained in our case is taken to be a weighted sum of all the inequivalent sites. The main features and their relative intensities of the experimental peaks are fairly well reproduced in the theoretical spectrum. Particularly, the pre-peak feature which was experimentally observed in  $\text{FePO}_4$  is well repro-

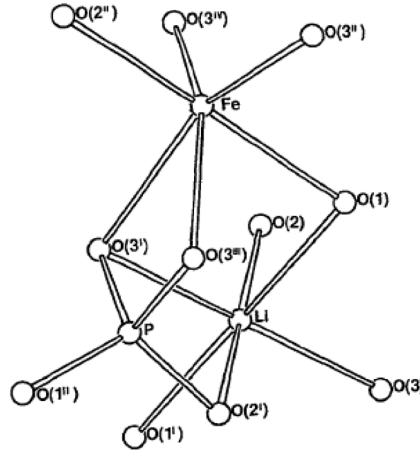
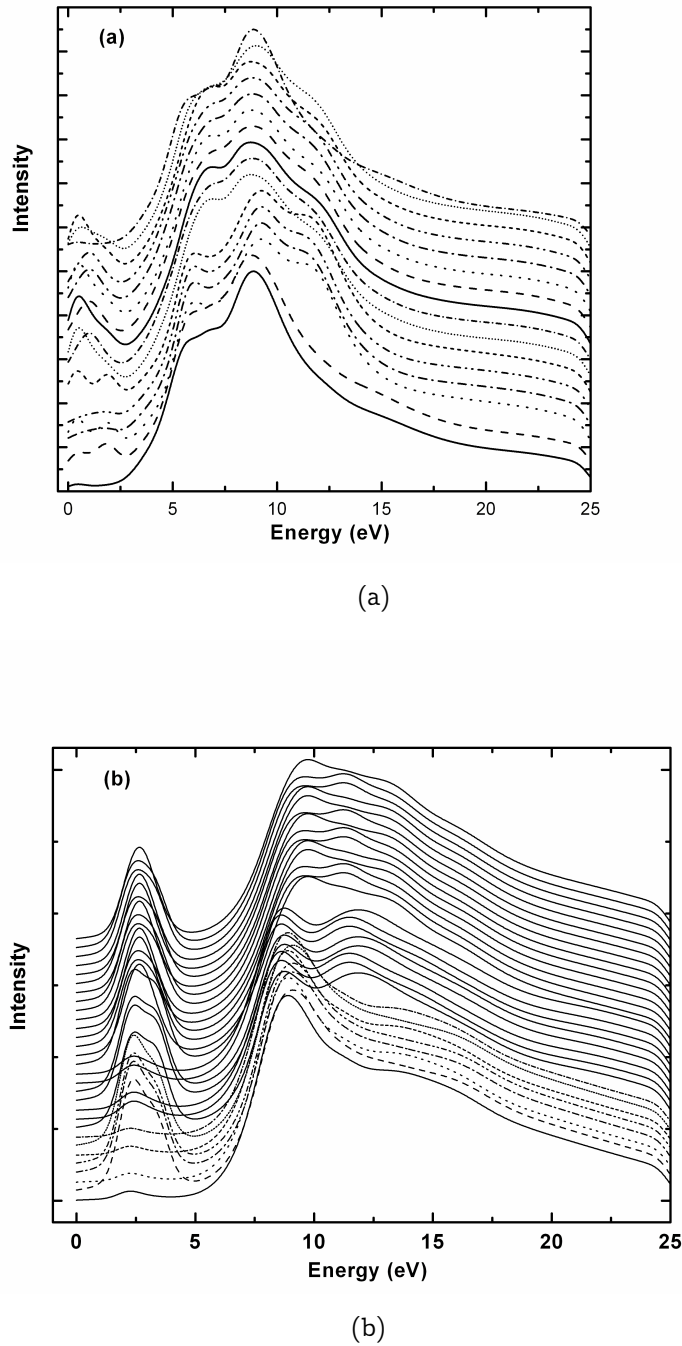


Figure 7.3: The inequivalent O sites in  $\text{LiFePO}_4$ . (After Ref [11])

duced in the theoretical spectra for  $\text{FePO}_4$ . The experimental peak feature B is also reproduced however the theoretical peak shows extra peak features which are not observed in the experimental peak. These differences can be qualitatively explained from the fact that core-hole effects were not included in the calculation of the spectra. We also used a smaller instrumental resolution in the calculation than in the experiment in order to see more details of the peak fine structure.

### Origin of the pre-edge peak

The bonding characteristics in both phase was already introduced in section 6.1, the O 2p states form molecular orbitals with Fe 3d, 4s and 4p orbitals resulting in  $e_g$ ,  $t_{2g}$ ,  $a_{1g}$  and  $t_{1u}$  molecular orbitals respectively. Due to this extensive hybridization of the respective energy states, the extraction/insertion of Li into the lattice cannot be simply explained as reduction/oxidation of the transition metal ion. As mentioned previously, the fact that the O-K edge is observed experimentally is as a result of the covalency and hybridization between Fe-3d states and O-2p states [124,125,132,133]. The threshold region of the O-K edge, ranging from the onset of the ionization edge to 7eV, represents transitions to the unoccupied 2p states which have been hybridized with the Fe-3d, about 15 eV from the threshold the ionization edge represents transitions to the unoccupied states 2p which have hybridized with the Fe-4s and-4p states. The O-K pre-edge peaks have been observed in studies conducted on O-K edges of similar transition metal compounds, particularly in superconductors. [118,120,122,124–126]. In these cases the pre-edge peaks was interpreted as originating from transitions from O 1s states to empty O 2p component of metal 3d hybridized with O 2p states. It is particularly interesting to note that the evolution of the O-K pre-edge in the  $\text{LiFe}^{\text{II}}\text{PO}_4/\text{Fe}^{\text{III}}\text{PO}_4$  system is similar to the O-K pre-edge signature observed when doping  $\text{La}^{\text{III}}$  by  $\text{Sr}^{\text{II}}$  in  $\text{La}_{(2-x)}\text{Sr}_x\text{CuO}_4$ . [122] According to the results obtained from calculations



*Figure 7.4: .*

Calculated O-K edge for the various inequivalent Oxygens in (a)  $\text{LiFePO}_4$  and  $\text{FePO}_4$

$\text{La}^{\text{III}}/\text{Sr}^{\text{II}}$  substitution creates holes at the top of the oxygen valence band which explain this pre-edge feature. However, based on the electronic structure presented in Fig. 6.1 (a) and (b) the explanation for the observed pre-edge peak in

$\text{LiFe}^{\text{II}}\text{PO}_4/\text{Fe}^{\text{III}}\text{PO}_4$  system appears to be different. The pre-peak has also been observed in similar transition metal compounds used in lithium ion batteries including  $\text{Li}_x\text{CoO}_2$  [134, 135], and  $\text{Li}_x[\text{Ni}_{0.3}\text{Co}_{0.3}\text{Mn}_{0.3}]\text{O}_2$ . [136] It was shown that the intensity and position of the pre-edge peak gradually changes with the extraction and insertion of Lithium ions. The position of the pre-edge peak is thus determined by the charge transfer, i.e. the reduction or oxidation on the metal site, which then influences the position of the d band with respect to the conduction band. The larger the charge transfer, the closer the d band will be with respect to the conduction band. The pre-edge peak also exists in  $\text{LiFePO}_4$  however it shifted 1-2 eV from the threshold of the main O-K peaks and as such it hidden within the main O-K edge which was represented by the peak B in Figure 7.1. The pre-edge peak in  $\text{LiFePO}_4$  therefore appears as the shoulder on the main peak which was marked with the blue arrow 1. Delithiation in  $\text{LiFePO}_4$  causes the 3d bands to be shifted to lower energies (as was shown in the DOS in Figures 6.12(a), 6.12(b), and 7.2. This makes the pre-edge peak visible in the EELS spectra of  $\text{FePO}_4$ . The pre-edge intensity is therefore related to the changes in the hybridization with the extraction of Li ions from the system. Adding/removing one lithium atom will roughly transfer/remove one electron to/from the Fe 3d band. This will reduce/increase the number of empty 3d levels and consequently change the intensity of the pre-edge peak.

### 7.3.2 $\text{FeL}_{2,3}$ edge

As mentioned in the preceding section, the  $\text{L}_{2,3}$  edges can be used as a direct probe of the formal valency and the spin state of the transition metal atoms. Figure 7.5 shows the Fe –  $\text{L}_{2,3}$  absorption edges before and after delithiation. In both cases, the Fe –  $\text{L}_{2,3}$  edge arises from the dipole allowed transition from 2p to 3d Fe states and is characterized by two peaks, the lower energy  $\text{L}_3$  edge at 708 eV and the  $\text{L}_2$  edge at 721 eV. The  $\text{L}_3$  edge and  $\text{L}_2$  edge, arise from the two ways that the spin quantum number,  $s$ , couples to the orbital angular momentum,  $l$ , giving the angular momentum,  $j = l + s$ . The total angular momentum  $\mathbf{J}$  is calculated by summing by all individual (angular momentum) and  $s$  (spin) values for every electron. This summing gives the total orbital ( $L$ ), spin ( $S$ ) angular momentum quantum numbers (and  $J=L+S$ ). This is known as Russell-Saunders or LS coupling. Additionally, this initial state will have a degeneracy given by  $2S + 1$  where  $S$  is the total spin. This process forms both the  $\text{L}_3$  edge and  $\text{L}_2$  edges. The  $\text{L}_3$  edge is due to transitions from the  $^2p_{3/2}$  ( $j = 3/2$ ) initial state, and the  $\text{L}_2$  edge is result of  $^2p_{1/2}$  ( $j = 1/2$ ) initial state transitions [137]. The  $\text{L}_2$  edge is broadened due to Coster-Kronig decay of the excited state leading to the smearing of the fine structure, the effects of this broadening are less in the  $\text{L}_3$  edge [67, 138]. Figures 7.6(a) and 7.6(b) show the  $\text{FeL}_3$  edge for  $\text{LiFePO}_4$  and  $\text{FePO}_4$  respectively. The observed peak features have been marked with colored arrows for both spectra. The  $\text{FeL}_{2,3}$  edge for  $\text{FePO}_4$  shows an energy shoulder at low energy side of the

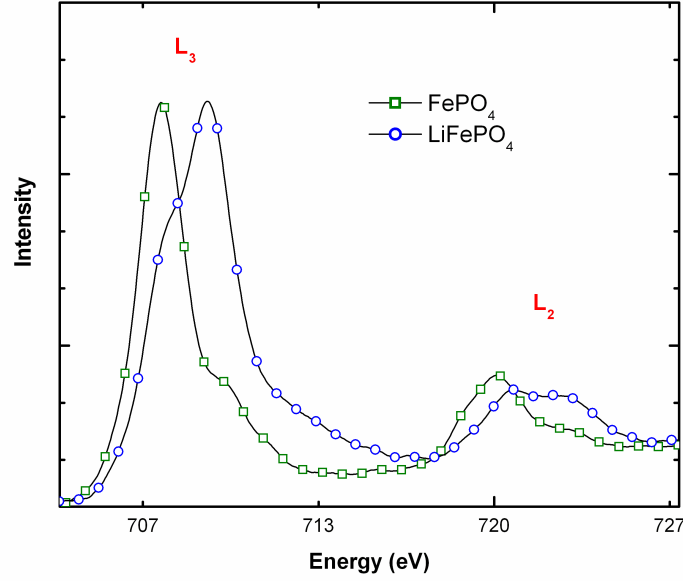


Figure 7.5: The fine structure of the  $\text{FeL}_{2,3}$  edge before and after delithiation.

main peak. The  $\text{FeL}_{2,3}$  edge for  $\text{LiFePO}_4$  shows an energy shoulder at high energy side of the main peak. The main peak is shifted to lower energies in the  $\text{FeL}_{2,3}$  edge for  $\text{FePO}_4$ . There are also changes in the  $L_3$  edge between the two phases. To investigate the origin of these changes it is essential to calculate the  $\text{FeL}_{2,3}$ . Unlike the O-K edge transitions the Fe  $L_{2,3}$  edge cannot be accurately calculated using single-particle DFT calculations due to the electronic-electronic interactions of the 3d electrons and because the effects of core-hole left after the excitation cannot be ignored [113]. As such ligand multiplet calculations that take into account electronic-electronic interactions, spin-orbit coupling, core-hole, covalency and crystal-field effects. Covalency effects are taken into account by introducing the ground and final state configurations and reduction of the Slater integrals. Ligand field theory has several parameters that have to be tweaked in order to fit the experimental results. In this case the main parameters that were fitted are the charge transfer energy  $\Delta$ , and energy separating the  $t_{2g}$  and  $e_g$  states,  $10Dq$ .

### Crystal field effects

As introduced in previous chapter 2, the electronic configuration of  $\text{Fe}^{2+}$   $\text{LiFePO}_4$  is  $t_{2g}(\uparrow)^3 e_g(\uparrow)^2 t_{2g}(\downarrow)^1$  which means three electrons occupy the spin up  $t_{2g}$  levels, two electrons occupy the spin up  $e_g$  levels and one electron occupies the spin-down  $t_{2g}$  level. The electronic configuration of the  $\text{Fe}^{3+}$  ion in  $\text{FePO}_4$  is  $t_{2g}(\uparrow)^3 e_g(\uparrow)^2$  where three electrons occupy localized  $t_{2g}$  levels, and two electrons in the  $e_g$  level. The energy separating the  $t_{2g}$  and  $e_g$  states is known as  $10Dq$ . Figures

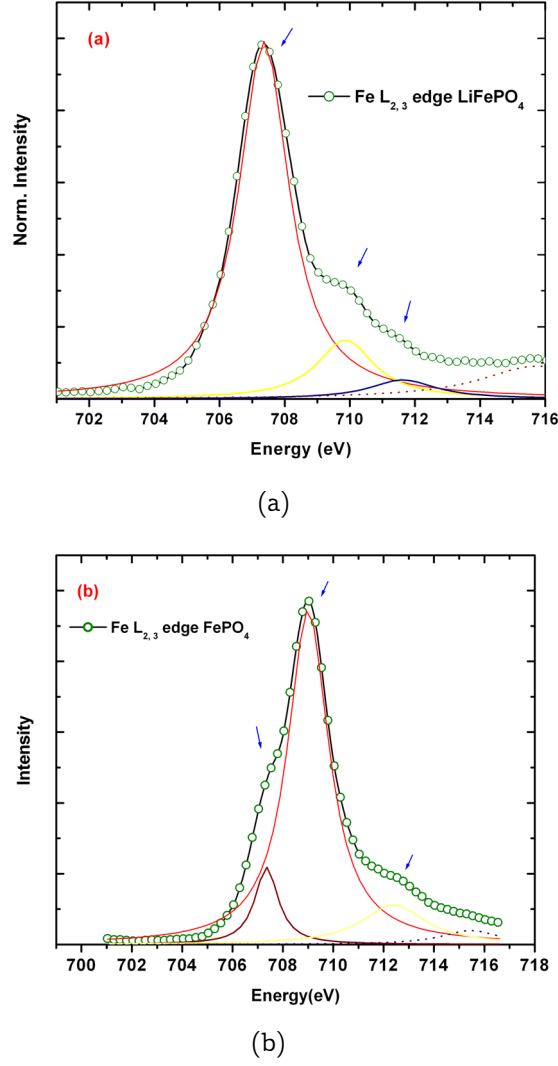
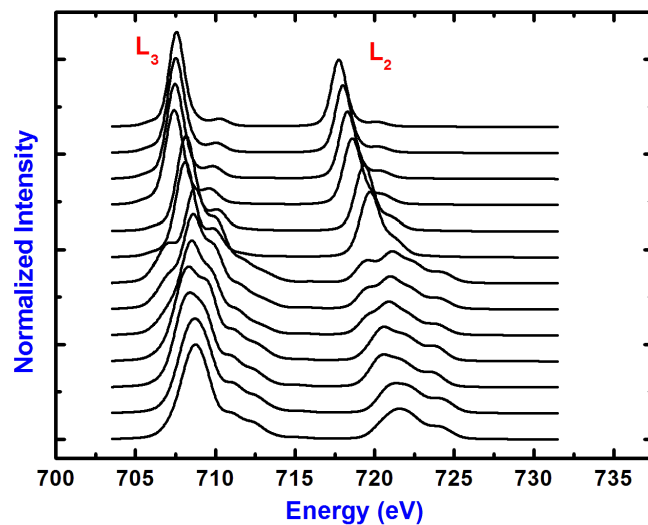


Figure 7.6: .

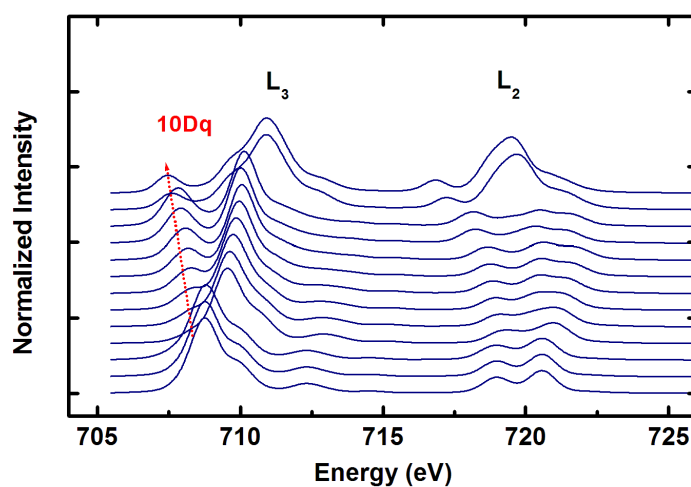
Fe  $L_3$  edge for (a)  $\text{Fe}^{2+}$  in  $\text{LiFePO}_4$  and (b)  $\text{Fe}^{3+}$  in  $\text{FePO}_4$ . The arrows mark the position of various peak features. The curves have been fitted using Lorentzian curves

7.7(a) and 7.7(b) show the calculated  $\text{Fe}L_{2,3}$  spectra for with increasing values of splitting energy  $10Dq$  and in an octahedral symmetry  $O_h$  for  $\text{Fe}^{2+}(\text{LiFePO}_4)$  and  $\text{Fe}^{3+}(\text{FePO}_4)$  respectively. In both cases the crystal field strength is varied between 0 eV to 3.9 eV. A positive  $10Dq$  means that the  $e_g$  states are higher in energy than the  $t_{2g}$  states. In a negative  $10Dq$  the  $e_g$  states are lower in energy than  $t_{2g}$  states. A  $10Dq$  value of 0 eV corresponds to a pure atomic multiplet case in which there is no crystal field but with p-d and d-d interactions taken into consideration. A crystal field splitting strength of 0.5 eV for  $\text{Fe}^{2+}$  and 1.5 eV for  $\text{Fe}^{3+}$  gives the best qualitative fit to the experimental data. In both cases the ions are in a high spin state and the change from high spin to low-spin state can be seen by a drastic change in the fine structure of the spectra above  $10Dq = 2.1$  eV.





(a)  $\text{FeL}_{2,3}$  edge calculated for  $\text{Fe}^{2+}$  calculated for an increasing cubic crystal field. The value of  $10Dq$  is increased from 0.0 to 3.9 eV.



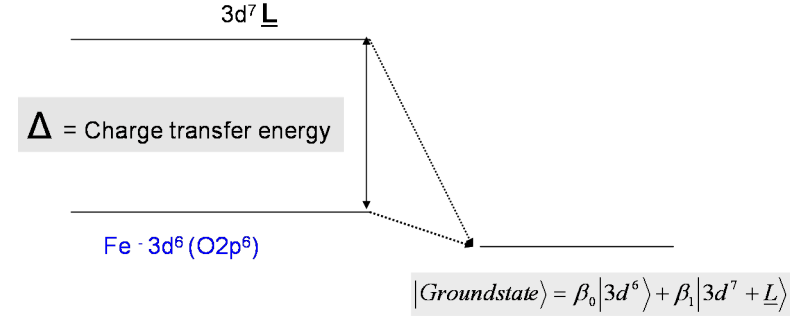
(b)  $\text{FeL}_{2,3}$  edge calculated for  $\text{Fe}^{3+}$  calculated for an increasing cubic crystal field. The value of  $10Dq$  is increased from 0.0 to 3.9 eV

**Figure 7.7:**  $\text{FeL}_{2,3}$  edge calculated for  $\text{Fe}^{2+}$  and  $\text{Fe}^{3+}$  calculated for an increasing values of  $10Dq$ .

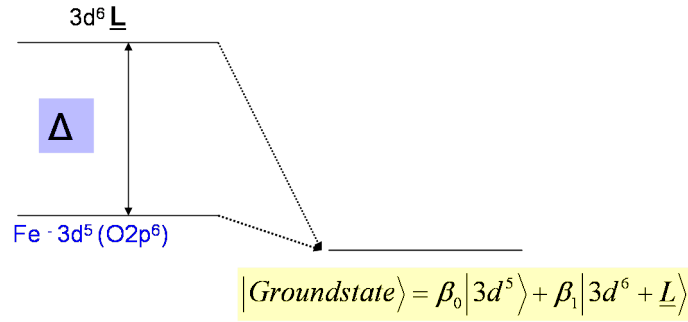
### Charge transfer effects

The parameter  $\Delta$  is an indicator of the degree of mixing between the Fe 3d and O 2p states. When the interaction between the Fe 3d and O 2p is taken to be

purely ionic, the the ground state is  $|3d^n\rangle$ , introducing some degree of covalent between the Fe 3d and O 2p states gives a ground state that is mixture of ionic and covalent interactions giving a ground state configuration of  $|3d^n\rangle + |3d^{n+1}\underline{L}\rangle$ .  $\underline{L}$  represents a core-hole in the O-2p valence band due to the covalent interaction. These ground state configurations are shown schematically in Figures 7.8(a) and 7.8(b) for  $\text{Fe}^{2+}(\text{LiFePO}_4)$  and  $\text{Fe}^{2+}(\text{LiFePO}_4)$  respectively.



(a) Ground state configuration in  $\text{LiFePO}_4$  ( $\text{Fe}^{2+}$ ) described by ionic configuration ( $3d^6$ ) and contribution of charge transfer (hybridization) with the oxygen ligands ( $3d^7\underline{L}$ )



(b) Ground state configuration in  $\text{LiFePO}_4$  ( $\text{Fe}^{2+}$ ) described by ionic configuration ( $3d^6$ ) and contribution of charge transfer (hybridization) with the oxygen ligands ( $3d^7\underline{L}$ )

**Figure 7.8:** Ground state configurations for (a)  $\text{Fe}^{2+}$  in  $\text{LiFePO}_4$  and (b)  $\text{Fe}^{3+}$  in  $\text{FePO}_4$

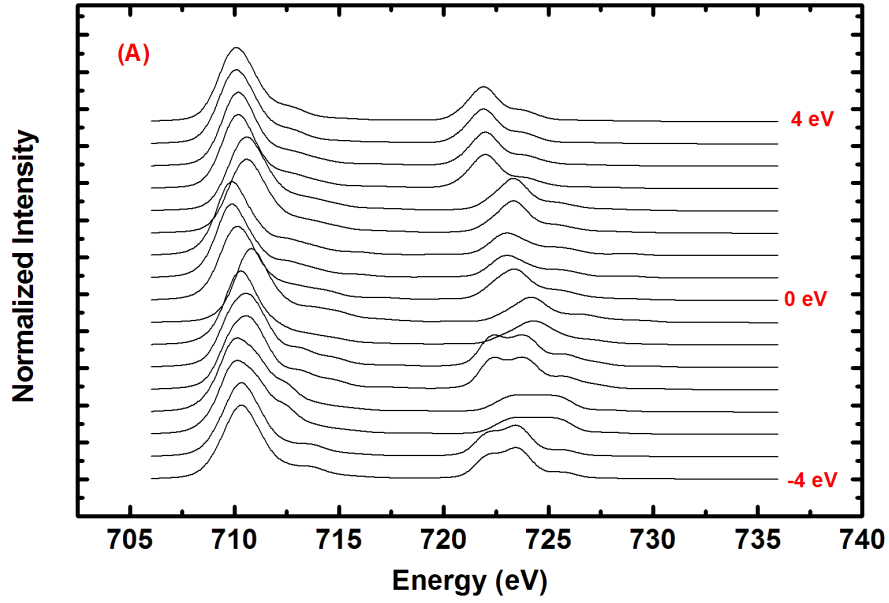
Figures 7.9(a) and 7.9(b) show the calculated spectra for  $\text{LiFePO}_4$  and  $\text{FePO}_4$  with varying charge transfer energy  $\Delta$ . In the case of  $\text{LiFePO}_4$ , (7.9(a)) the Fe ion is taken to be in a divalent oxidation state,  $\text{Fe}^{2+}$ , ( $3d^5$ ), and the first two configurations are  $|3d^5\rangle, |3d^6\underline{L}\rangle, |3d^7\underline{L}^2\rangle, \dots$ . In the case of  $\text{FePO}_4$  (7.9(b)), the iron ion is assumed to be in trivalent  $\text{Fe}^{3+}$ , ( $3d^6$ ), oxidation state and the possible configurations include  $|3d^6\rangle, |3d^7\underline{L}\rangle, |3d^8\underline{L}^2\rangle, \dots$ . The ground-state is then expressed as a linear combination of possible configurations for  $\text{LiFePO}_4$   $|g\rangle = \alpha_0|3d^5\rangle + \alpha_1|3d^6\underline{L}\rangle + \alpha_2|3d^7\underline{L}^2\rangle$ . After the excitation of a 2p electron the final state is  $|g\rangle = \beta_0|3d^6\rangle + \beta_1|3d^7\underline{L}\rangle + \beta_2|3d^8\underline{L}^2\rangle$  for  $\text{Fe}^{3+}$  in  $\text{FePO}_4$  the ground-state is then expressed as a linear combination of possible configurations  $|g\rangle =$

$\alpha_0|3d^6\rangle + \alpha_1|3d^7\bar{\underline{L}}\rangle + \alpha_2|3d^8\bar{\underline{L}}^2\rangle$ . After the excitation of a 2p electron the final state is  $|g\rangle = \beta_0|3d^7\rangle + \beta_1|3d^8\bar{\underline{L}}\rangle + \beta_2|3d^9\bar{\underline{L}}^2\rangle$ . From these curves the value for  $\Delta$  that qualitatively best fits the experimental spectra was used. This value together with the fitted values for 10Dq, Slater integrals, and calculated  $U_{dd}$  were then used to calculate the  $\text{FeL}_{2,3}$  spectra for both ionic species. The parameters used in the calculations of the  $\text{FeL}_{2,3}$  edge are listed in the table 7.1 The input param-

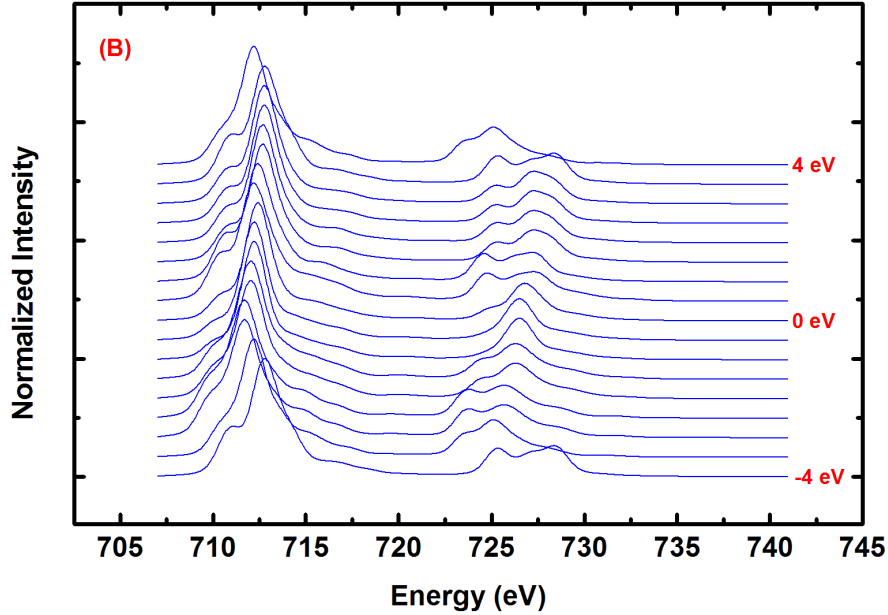
*Table 7.1: Parameters used in the calculation of the  $\text{FeL}_{2,3}$  edge for  $\text{Fe}^{2+}$  and  $\text{Fe}^{3+}$*

Parameter (eV)	$\text{Fe}^{2+}$	$\text{Fe}^{3+}$
$\Delta$	3	3
$\kappa$	80%	75%
$\xi$	0	0
$U_{dd}$	4	5
$U_{pd}$	5	5
T1(b1)	0.5	0.5
T1(a1)	0.5	0.5
T1(b2)	0.25	0.25
T(e)	0.25	0.25
10Dq	0.5	1.5

eters are O-2p-Fe-3d charge transfer energy  $\Delta$ , 3d-3d Coulomb repulsion  $U_{dd}$ , the Fe-2p-Fe-3d Coulomb interaction  $U_{pd}$ , the  $O_h$  crystal splitting field 10Dq, Slater integrals  $\kappa$ , and the Fe-3d-O-2p and O-2p-O-2p hopping integrals. The values for  $U_{dd}$  were obtained from theoretical calculations. Figure 7.10(a) and 7.10(b) show the calculated  $\text{FeL}_{2,3}$  edges for  $\text{Fe}^{2+}$  and  $\text{Fe}^{3+}$ , respectively, compared with experimentally derived results. In Figure 7.10(a), the agreement between the calculated and experimental spectra is excellent. The main  $L_3$ -edge shape is reproduced, including a lower-energy peak at 707 eV and the  $L_2$ -edge is also clearly reproduced. For  $\text{Fe}^{3+}$ , Figure 7.10(b) the agreement between calculated and theoretical  $L_3$  edge is also good, however the theoretical spectrum overestimates the intensity of  $L_3$  peak. (708-712) and  $L_2$  intensity (719-725 eV). In the ligand field multiplet model, the ground state is approximated by a single electronic configuration  $d^n$ . Including charge transfer effects allows for mixing of the metal valence d orbitals with ligand valence p orbitals and therefore necessitates multiple configurations. The charge transfer multiplet model adds a  $d^{n+1}L$  configuration to the single configuration  $d^n$  ground state of the ligand field model. The fitting of the experimental spectra for the  $\text{FeL}_{2,3}$  edge have given a configuration of 81.121% $|3d^6\rangle$ , 18.889% $|3d^7\bar{\underline{L}}\rangle$  for  $\text{Fe}^{2+}$  and 80.121% $|3d^6\rangle$ , 18.889% $|3d^7\bar{\underline{L}}\rangle$   $\text{Fe}^{3+}$ . This means the Fe-O bond is largely ionic with some covalency. Delithiation process increases covalency slightly

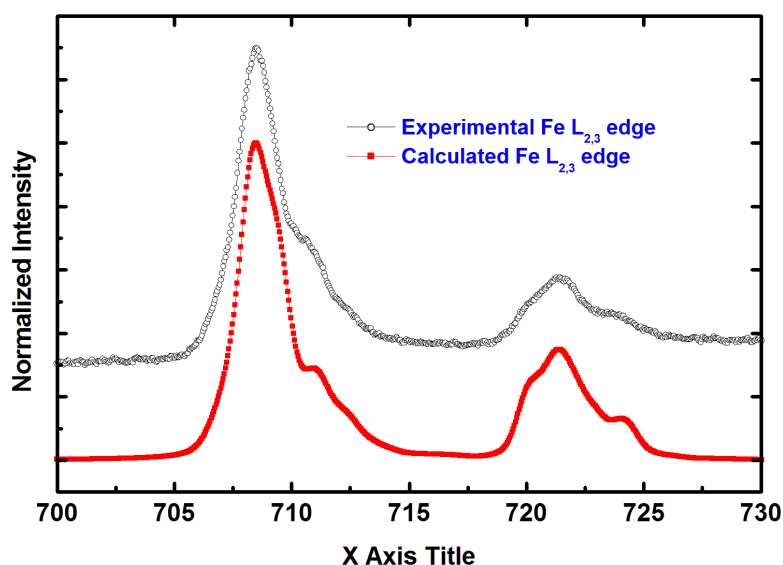


(a)  $\text{FeL}_{2,3}$  edge calculated for  $\text{Fe}^{2+}$  calculated for a varying charge transfer  $\Delta$ . The value of  $\Delta$  is increased from -4 to 4 eV.

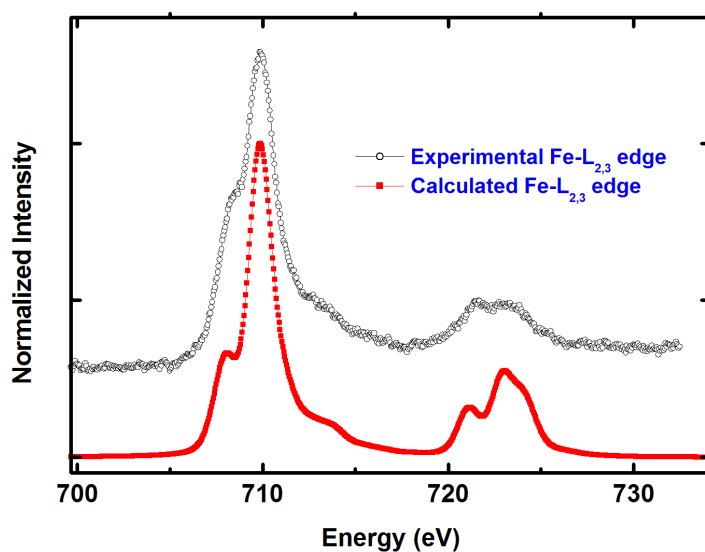


(b)  $\text{FeL}_{2,3}$  edge calculated for  $\text{Fe}^{3+}$  calculated for a varying charge transfer  $\Delta$ . The value of  $\Delta$  is increased from -4 to 4 eV.

*Figure 7.9:  $\text{FeL}_{2,3}$  edge calculated for  $\text{Fe}^{2+}$  and  $\text{Fe}^{3+}$  for varying values of  $\Delta$ .*



(a)  $\text{FeL}_{2,3}$  edge calculated for  $\text{Fe}^{2+}$  after incorporating charge transfer effects.



(b)  $\text{FeL}_{2,3}$  edge calculated for  $\text{Fe}^{3+}$  after incorporating charge transfer effects.

*Figure 7.10: Calculated  $\text{Fe}^{2+}$  and  $\text{Fe}^{3+}$  spectra. The values of the parameters used in the calculations are listed in Table 6.1*

### Analysis of the $\text{FeL}_{2,3}$ edge

From the analysis presented in this section it can be seen that the  $\text{Fe L}_{2,3}$  edge exhibits several characteristics changes delithiation. These included

- Shift in peak position (Chemical shift) The energy shift observed at the  $\text{FeL}_{2,3}$

edge has already been observed in other transition metal compounds and is attributed to the oxidation of  $\text{Fe}^{2+}$  to  $\text{Fe}^{3+}$  ion with delithiation [114]. The explanation for this energy shift has to do with the change of the valence electron distribution around the Fe ion with delithiation. The oxidation of  $\text{Fe}^{2+}$  to  $\text{Fe}^{3+}$  with delithiation, results in the decrease of valence charge density around the transition metal ion which results in a reduced screening of its nuclear field and subsequently results in positive shift [60, 139]. These changes in the  $\text{FeL}_{2,3}$  position are related to the shift in the Fe 3d band to lower energies with delithiation (this was presented in Figures 6.12(a) and 6.12(b)).

- Changes in the fine-structure The fine structure of the  $\text{FeL}_{2,3}$  edge was modeled using crystal field (10Dq) and charge transfer effects ( $\Delta$ ). As was shown in the electronic calculations and VEELS the  $\text{FePO}_4$  could be considered to be Charge-transfer insulator and  $\text{LiFePO}_4$  could be taken to be Mott-Hubbard insulator. The changes in the fine structure with delithiation could therefore be related to the changes in the interaction between the Fe 3d bands and O 2p bands with delithiation. As mentioned previously both  $\text{Fe}^{2+}$  in  $\text{LiFePO}_4$  and  $\text{Fe}^{3+}$  in  $\text{FePO}_4$  are in a high-spin state where both  $e_g$  and  $t_{2g}$  energy states are occupied. This gives an electronic configuration  $t_{2g}(\uparrow)^3 e_g(\uparrow)^2 t_{2g}(\downarrow)^1$  for  $\text{LiFePO}_4$  and  $t_{2g}(\uparrow)^3 e_g(\uparrow)^2$ . When Lithium ions are removed from the lattice an electron is removed from  $t_{2g}$ , this lowers the energy of the  $t_{2g}$  states with respect to the O 2p states and increases the hybridization of the Fe 3d states with O 2p states. As such  $\text{FePO}_4$  is more covalent. The reverse happens when Li is inserted into the lattice during the lithiation process the spin down  $t_{2g}(\downarrow)^1$  is occupied increasing the energy of the Fe 3d states and consequently reducing the hybridization with O 2p states and as such  $\text{LiFePO}_4$  is more ionic [140].

The spin state of the Fe ion does not change with delithiation. Fe ion is in a high spin state in both  $\text{LiFePO}_4$  and  $\text{FePO}_4$ . The co-ordination environment also does not change. It was found that the ground state of Fe in  $\text{LiFePO}_4$  and  $\text{FePO}_4$  is best described by the configuration  $|3d^n\rangle + |3d^{n+1}\underline{L}\rangle$  where  $\underline{L}$  represents a core hole in the O-2p valence band. This mixture of configurations shows that the Fe-O bond has partial ionic and covalent character.

### 7.3.3 Li-K edge

Figure 7.11 shows the Li-K edge and Fe –  $M_{2,3}$  edge (55-57 eV) absorption edges for the lithiated  $\text{LiFePO}_4$  and delithiated  $\text{FePO}_4$  respectively.

In this case it is very hard to accurately analyze the structure of the Li K edge since it is transposed to the Fe –  $M_{2,3}$  edge. The  $\text{FeM}_{2,3}$  arises from the dipole allowed  $3p \rightarrow 3d$  and as such probes the unoccupied 3d states of the Fe ion. The

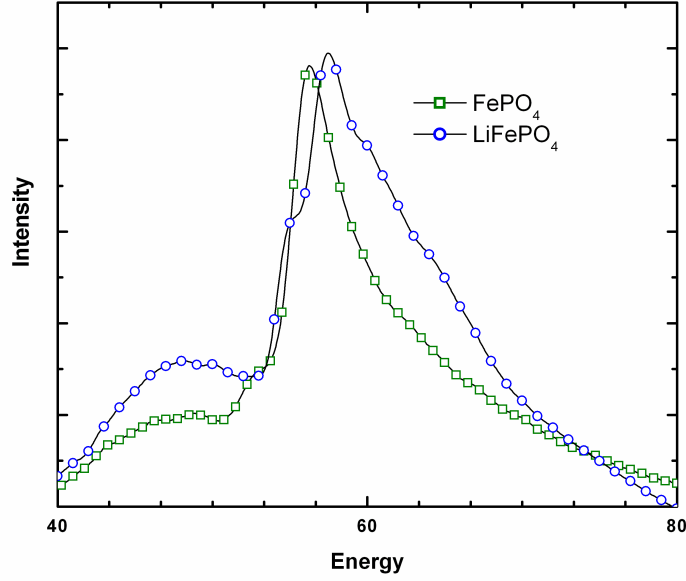


Figure 7.11: *Li-K and Fe  $M_{2,3}$  edges for  $\text{LiFePO}_4$  and  $\text{FePO}_4$*

effects of electronic correlations cannot be ignored and single-particle description of Li-K edge and the Fe –  $M_{2,3}$  is not sufficient.

### 7.3.4 P-K edge

The P-K edge is free of interference and correlation effects and should provide useful information regarding the role of the phosphate polyanion ( $\text{PO}_4^{2-}$ ) in regulating the electronic structure of  $\text{LiFePO}_4$  and  $\text{FePO}_4$  unit. The fine structure of the P-K spectra does not vary much with delithiation. The spectra are both characterized by three peak features. The P-K before and after delithiation is shown in Figure 7.12. The first two peaks are sharp and featureless while the third peak is also featureless but much more broad. The most important observation is that an edge shift is observed after delithiation. The P-K edge in  $\text{FePO}_4$  is shifted to a lower energy when compared to the  $\text{LiFePO}_4$ . Difference between  $\text{LiFePO}_4$  and  $\text{FePO}_4$  are more visible in the O-K and  $\text{FeL}_{2,3}$  edges.

As introduced in sec. 3.3, Chap.3, an ionization edge results from the transition of core electrons to unoccupied states in the conduction band; for these transitions to take place the energy transfer between the incident electron and the core electron must be greater than the binding energy. Hence, the core-edge onsets represent the ionization threshold supplied by these transitions. Core-loss edge onsets represent the ionization

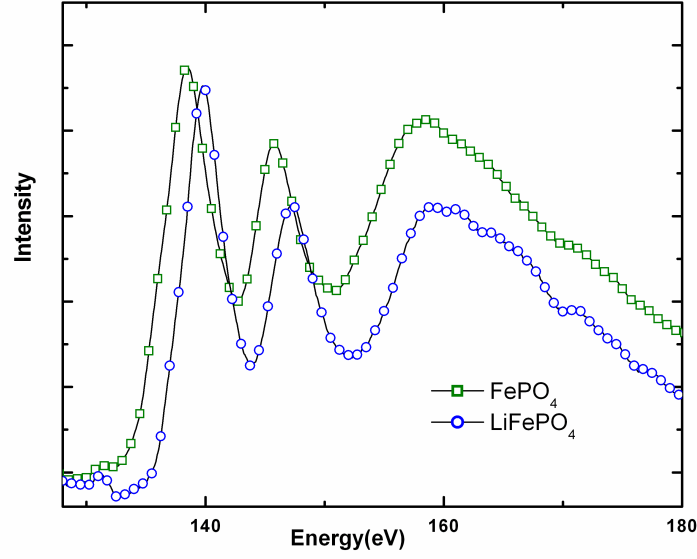


Figure 7.12: P-K edge for  $\text{LiFePO}_4$  and  $\text{FePO}_4$ .

threshold, the energy that approximately corresponds to the inner-shell binding energy. [60, 114]. In reality however the core-shift are more complex since the effects of the core-hole effects. In both P-K and  $\text{FeL}_{2,3}$  edges a chemical shift of the ionization edge is observed with delithiation. The energy shift observed at the P – K edge is also related to the changes in the electronic structure around the the Fe and O ions. As shown in Figure 2.1 the  $\text{FeO}_6$  octahedra and  $\text{PO}_4$  share an edge In both  $\text{LiFePO}_4$  and  $\text{FePO}_4$ . As a result the P atoms share a common oxygen nearest neighbor with Fe along a  $\text{Fe} \rightleftharpoons \text{O} \rightleftharpoons \text{P}$  linkage. This gives rise to what is known as the inductive effect. As explained by Tang *et al* [42] and Padhi *et al* [10], the inductive effect causes the electron cloud between the atoms to be displaced towards the more electronegative of the two atoms, in this case the P atom. atoms. This causes a permanent state of bond polarization, where the more electronegative atom has a slight negative charge ( $\sigma^-$ ) and the other atom has a slight positive charge ( $\sigma^+$ ). Therefore, the strength of the covalent Fe-O bond is weakened via the inductive effect making the Fe-O bond more ionic in  $\text{LiFePO}_4$  and subsequently influences the redox potential of the  $\text{Fe}^{2+}/\text{Fe}^{3+}$  couple. Delithiation causes the change of oxidation state of the Fe ion increasing the covalent nature of the Fe-O bond, as such the electron density around phosphorous atoms is reduced and this results in the shift of the P-K edge. This effect has also been observed in the delithiation of  $\text{LiCoPO}_4$  [141].



## 7.4 Conclusion

In summary the results presented in these chapter show the changes and reorganization of the electronic structure in  $\text{LiFePO}_4$  with delithiation. These changes in the electronic structure are reflected in the observed changes of core loss EELS spectra. These include shifts in the peak position (chemical shifts) for the  $\text{FeL}_{2,3}$  and P-K edges, and changes in the fine structure of the  $\text{FeL}_{2,3}$  and O-K edges. Chemical shifts have been interpreted as arising from the changes in the valence electron density around the Fe and P ions with delithiation. Delithiation cause the electron density around the Fe ion to decrease and makes the Fe-O-P bond more covalent. Consequently the electron density around the P atoms decreases this is seen as the peak shift in the EELS spectra of the P-K edge. Chemical shifts on the  $\text{FeL}_{2,3}$  edge reflect the shifting of the Fe-3d band to lower energies with delithiation.

We have also modeled the fine structure of  $\text{FeL}_{2,3}$  edge and showed that the ground state of Fe in  $\text{LiFePO}_4$  and  $\text{FePO}_4$  is best described by the configuration  $|3d^n\rangle + |3d^{n+1}\underline{L}\rangle$  configurations where  $\underline{L}$  represents a core hole in the O 2p valence band. This mixture of configuration shows that the Fe 3d and O 2p states are hybridized and consequently the Fe-O band shows both ionic and covalent character. The fine structure of the O-K edge in  $\text{FePO}_4$  shows a pre-edge peak that is observed above the threshold of the O-K edge. This peak is absent in  $\text{LiFePO}_4$  spectrum. The differences in the O-K spectra between  $\text{LiFePO}_4$  and  $\text{FePO}_4$  are also reproduced in the calculated O-K edges. The pre-edge peak at the O-K edge is interpreted to be due to transitions from the O -1s state to the O 2p component of the Fe3d-O-2p states in the conduction band. The intensity of the pre-edge peak is related to the increase in the degree of hybridization between Fe 3d-O2p states with the extraction of lithium from the lattice. The results obtained from core-loss EELS agree with the ones obtained using VEELS and theoretical calculations. The changes in the electronic structure with delithiation which included shift of the Fe 3d band and increased hybridization between Fe 3d and O 2p states are therefore characterized in the core-loss EELS spectra by chemical shift of the  $\text{FeL}_{2,3}$  edge and the pre-edge peak respectively.



## Structural properties in $\text{Li}_{(1-x)}\text{FePO}_4$

As was indicated in the introductory sections both electronic and ionic conduction properties have a very important influence on the electrochemical properties of  $\text{LiFePO}_4$ . It has been proposed that the mobility of Li ions across the  $\text{LiFePO}_4 - \text{FePO}_4$  phase interface determines the rate of Li diffusion within the grain [10, 27]. There are several delithiation mechanisms which have been advanced to explain this process. This include the core-shell model [10], the one-dimensional delithiation model [27, 38] and the domino-cascade model [36]. These models have been explained in more details in Chapter 2. As shown in the phase diagram of  $\text{LiFePO}_4$  (Figure 2.6, Chapter 2) the delithiation process in  $\text{LiFePO}_4$  is a two phase process, characterized by two end members fully lithiated  $\text{LiFePO}_4$  and fully delithiated  $\text{FePO}_4$ . According to the phase diagram there should be two  $\text{LiFePO}_4$  and  $\text{FePO}_4$  phases at a partial state of delithiation. Therefore one way to examine the delithiation mechanism is to examine the nature of phase interface and phase distribution in partially delithiated grains. This chapter presents structural studies obtained from partially delithiated grains

### 8.1 Experimental Details

Partially delithiated and fully delithiated samples were obtained through chemical and electrochemical delithiation methods described in the following section. The state of delithiation was established by using X-ray diffraction and Rietveld methods as introduced in Chapter 3 Sample preparation methods for TEM have

been known to cause defects in the TEM samples since they involve mechanical grinding, and ion milling and this can lead generation of defects and destroy the sample. Therefore, to avoid this sample grinding has not been done. Since most particles are in the order of 100 nm thickness, high acceleration voltage of 300 kV was used in making HRTEM images.

### 8.1.1 Electrochemical Measurements

For electrochemical delithiation, the electrodes were prepared with 20 wt % of conductive carbon and 10 wt% of PTFE powder being added to the lithium iron phosphate powder and mixed in an agate mortar. These were then rolled into a free standing film flaked and pressed into strips of Aluminum grid. Lithium metal was used as counter and reference electrode and 1M  $\text{LiPF}_6$  in EC: DMC = 1:1 was used as the electrolyte. Cell assembling and electrochemical measurements were performed in an argon box. The cells were galvanostatically cycled at room temperature between 2.9 and 4.0 V versus  $\text{Li}/\text{Li}^+$  at a specific current of  $C/20$ . Partially delithiated electrodes ( $\text{Li}_{(0.5)}\text{FePO}_4$ ) were removed at state of charge (SOC) of 50%. Chemical delithiated samples were obtained by treating the  $\text{LiFePO}_4$  powders with a  $\text{K}_2\text{S}_2\text{O}_8$  solution in varying ratios to give partially and fully delithiated samples. The formula for the delithiation is  $2\text{LiFePO}_4 + \text{S}_2\text{O}_8^{2-} \rightarrow 2\text{FePO}_4 + 2\text{Li}^+ + 2\text{SO}_4^{2-}$ . Half delithiated samples  $\text{Li}_{0.5}\text{FePO}_4$  delithiated samples were obtained from a 4:1 ratio of  $2\text{LiFePO}_4$  to  $\text{K}_2\text{S}_2\text{O}_8$  while fully delithiated  $\text{FePO}_4$  samples were obtained by using 2:1 ratio between  $\text{LiFePO}_4$  and  $\text{K}_2\text{S}_2\text{O}_8$ .

## 8.2 Results and Discussion

Figure 8.1 shows the charge-discharge curve of  $\text{LiFePO}_4$ . The blue curve represents a full charge-discharge cycle while the red curve represents the partial charge giving a stoichiometry of  $\text{Li}_{0.5}\text{FePO}_4$ . Partially delithiated samples examined in this section are represented by the red curve. As can be observed in the the charge-discharge curve  $\text{LiFePO}_4$  maintains a constant voltage through the discharge cycle until the delithiation process is almost complete. The curve shows a full charge-discharge curve (blue curve) and a partial charge curve (red curve). During the partial charge, half of the Li ions have been removed from the  $\text{LiFePO}_4$  lattice.

According to Padhi et al [10], the charge-discharge curves for  $\text{LiFePO}_4$  show that the voltage is independent of value of  $x$  for the over a long range of which indicates that delithiation/lithiation processes proceed by the motion of a two-phase interface. This is demonstrated by the voltage plateau observed in the figure 8.1. The presence of the voltage plateau suggest that a two phase relationship is maintained within the crystallite. The XRD patterns shown in Figure 8.2 show that at a partial delithiated state ( $\text{Li}_{(0.5)}\text{FePO}_4$ ) the samples contains two phases ,  $\text{LiFePO}_4$  and  $\text{FePO}_4$ .

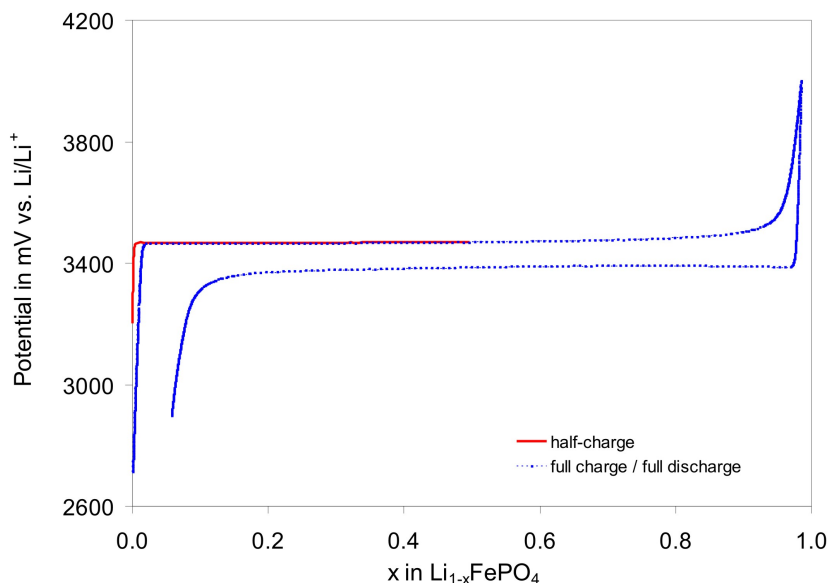


*Figure 8.1: The charge-discharge curve for the delithiation of  $\text{LiFePO}_4$ . The charge-discharge process is accompanied by phase transformation between the two end-members  $\text{LiFePO}_4$  and  $\text{FePO}_4$*

XRD results give the phase composition of partially delithiated  $\text{LiFePO}_4$  however this information does not provide clarity on the nature of the interface between the two phases or whether the two phases are in one grain or different grains are made up of different phases. While being very important in phase and structure analysis XRD and neutron diffraction techniques provide a volume averaged picture of the crystal structure. To obtain local information regarding the atomic structure of the delithiated grain, TEM techniques need to be used. Figure 8.3 shows the microstructure of the grains in a partially delithiated sample. Delithiated grains show extensive defective micro-structure arising as a result of the lattice mismatch between the lithiated and the delithiated phases.  $\text{LiFePO}_4 - \text{FePO}_4$  transformation results in a lattice volume mismatch of  $\approx 7\%$ . This kind of defective micro-structure was not observed in non-delithiated samples.

HRTEM images were taken across the (the area indicated by red square in figure 8.3) defected regions. Phase analysis of the HRTEM image was also done following the schemes presented in Chapter 3. The main idea behind the use of GPA method is to use the distribution of lattice parameters to map out the structure of phases in partially delithiated grain. Figure 8.4(a), (b) and (c) show respectively the HRTEM image, an intensity map showing the distribution of lattice parameters, and an intensity profile obtained from the lattice parameter distribution map. The lattice parameter distribution has been calculated for the reflection  $g_{(010)}/b$ . This crystal direction is important as it is parallel to the reported Li diffusion path [27]. i.e perpendicular to the (010) planes. The lattice parameters are represented in a colour/intensity map where the the brighter the

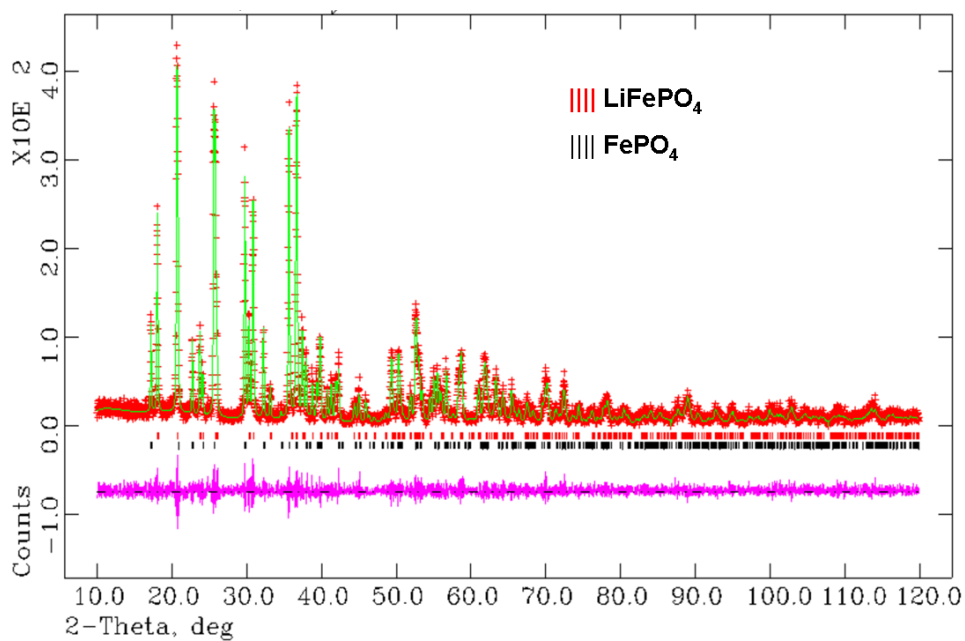


*Figure 8.2: X-ray diffraction pattern of partially delithiated  $\text{Li}_{0.5}\text{FePO}_4$  sample. The results show that at a partially delithiated state two phases  $\text{FePO}_4$  and  $\text{LiFePO}_4$  co-exist*

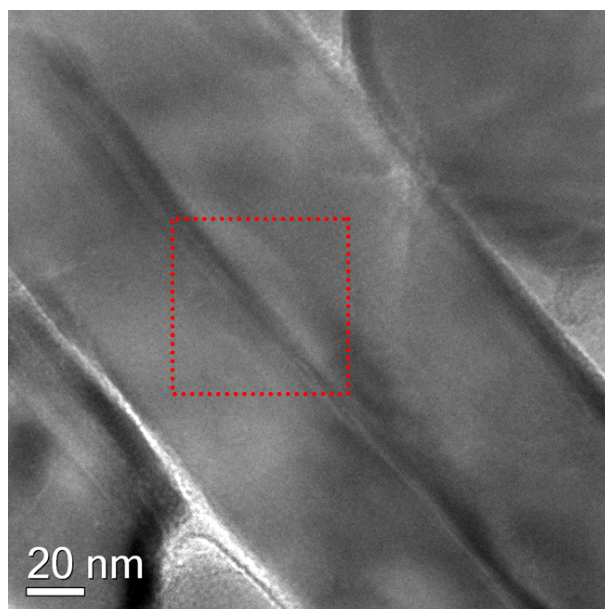


*Figure 8.3: Microstructure from a partially delithiated sample. The grains are characterized by a defect that run parallel to the elongation axis of the particle. The dotted square shows the region where HRTEM images were obtained*

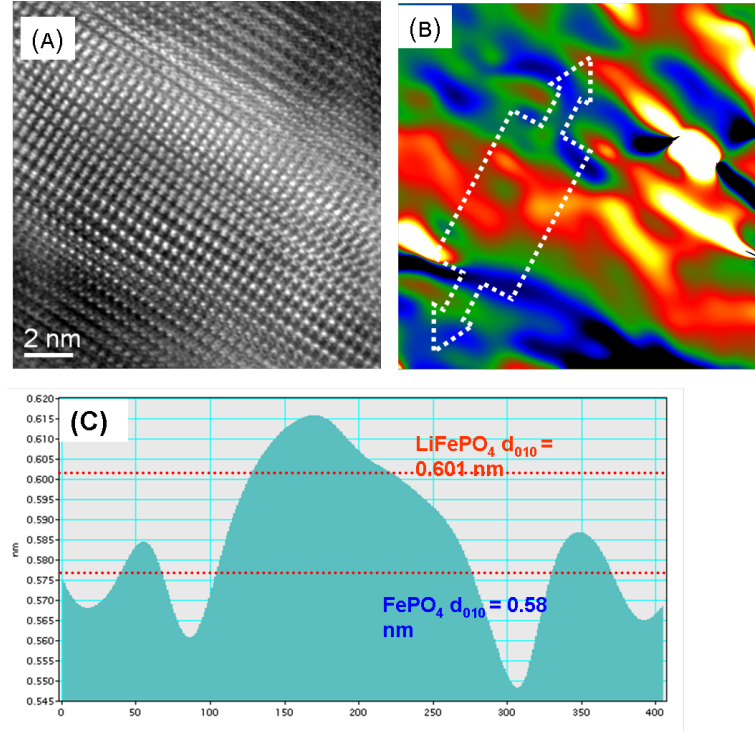


**Figure 8.4:** (a) HRTEM image from a partially delithiated grains (b) Colour map showing the distribution of the  $d_{010}$  lattice parameter in the HRTEM image. The broad white arrow shows the integrated region where the intensity profiles were obtained (c) Intensity profile obtained from the lattice parameter distribution map.

color/intensity represents a certain value of the lattice parameter. In the case of Figure 8.4(b) the red colour/high intensity represent areas where the lattice parameter of  $\approx 0.61$  nm has been measured. The darker regions represent regions where the lattice parameter ( $d_{hkl}$ ) of  $\approx 0.58$  nm has been determined. The former corresponds to the b parameter for  $\text{LiFePO}_4$  and the latter to the  $\text{FePO}_4$  lattice parameter.

In order to obtain a statistically relevant results many grains were examined. Figure 8.5 shows a HRTEM image, lattice parameter intensity map and intensity profile obtained from another partially delithiated grain. Similar to the previous result it can be seen that the distribution of the lattice parameters corresponds to b for both  $\text{LiFePO}_4$  and  $\text{FePO}_4$ .

This analysis was repeated for many grains and the cases represented above were found. In many instances both  $\text{LiFePO}_4$  and  $\text{FePO}_4$  were found to co-exist in same grain. These results show that the phase interface of the various phases is formed perpendicular to the  $[010]$  direction which corresponds to the  $\text{Li}^+$  diffusion path. The results presented above correspond to model proposed by Chen. [38,51]. However contrary to Chen we did not see any amorphous boundary between the delithiated and lithiated phases. In fact the interfaces seemed to be coherent. Delmas *et al* reported that the partial delithiation process results in single phase

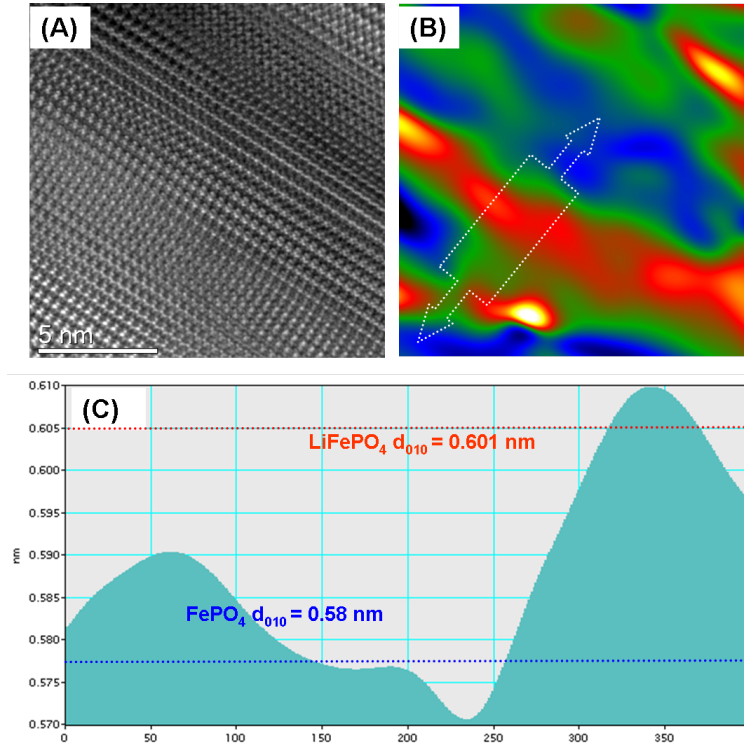


*Figure 8.5: (a) HRTEM image from a partially delithiated grains (b) Colour map showing the distribution of the  $d_{010}$  lattice parameter in the HRTEM image. The broad white arrow shows the integrated region where the intensity profiles were obtained (c) Intensity profile obtained from the lattice parameter distribution map.*

grains, i.e either  $\text{LiFePO}_4$  or  $\text{FePO}_4$  and not two-phase as reported previously [36]. These results support the 1D model of delithiation. We did not find any evidence to support the core-shell model.

### 8.2.1 Modelling the $\text{LiFePO}_4$ - $\text{FePO}_4$ interface

The accuracy of GPA depends on several factors. These include [142, 143]

- Errors associated with the technique itself. This includes the accuracy of the masks to select the reflection and errors in the determination of peak centers
- Errors arising from the sample including sample thickness, beam damage, and amorphous layers.
- Errors due to the microscope aberrations especially the spherical aberration and distortions from the lens system [88]

This section tries to investigate the accuracy of the GPA in determining phase distribution in a sample. A theoretical model of the interface between  $\text{LiFePO}_4$  and  $\text{FePO}_4$  phases was made and HRTEM images calculated using a variety of



sample and imaging conditions. Figure 8.6(a) shows the atomic model of the  $\text{LiFePO}_4$ - $\text{FePO}_4$  interface while figure 8.6(b) shows the a calculated HRTEM from the atomic model. The model consists of alternating  $\text{FePO}_4$  and  $\text{LiFePO}_4$  unit cells.

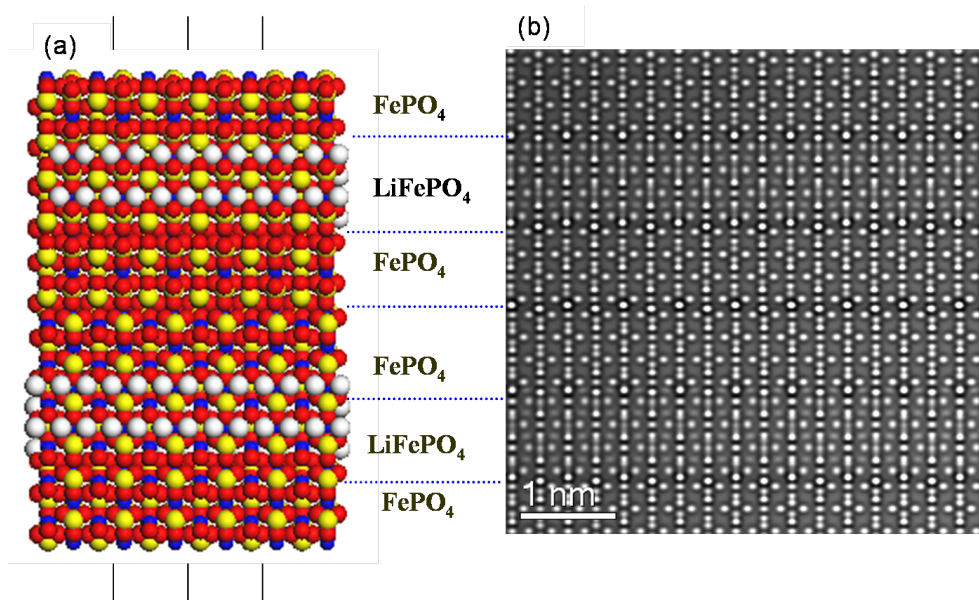


*Figure 8.6: (a) Atomic model of the  $\text{LiFePO}_4$ - $\text{FePO}_4$  interface (b) Simulated HRTEM images obtained from the atomic model*

The simulated HRTEM images were calculated using an in-house software utilizing the multislice algorithm. The multislice algorithm is a numerical integration method to solve the Schrödinger equation [?]. In this method the incident electrons interacting with the sample are represented by plane waves. The sample unit cell is then cut into thin slices and the electron plane wave is propagated through each slice and the projected potential for each slice calculated. The final projected potential is a sum of all projected potentials derived from each slice. The HRTEM images were calculated for several imaging conditions including defocus, Cs value and sample thickness ( for explanation on this parameters see Chapter 3). The Cs, was set to  $20 \mu \text{m mm}$ , and the thickness of the sample was varied between 2 nm to 20 nm. The convergence half-angle was set to 0.5 mrad and a defocus spread to 1 nm. A multislice calculation was performed where the unit cell was divided with separate slices for each atomic layer was performed in order to create the HRTEM image. A series of HRTEM images calculated for various thickness are shown in Figure 8.7. The HRTEM images are for the [001] orientation. This means the (010) and (100) atomic planes lie in the x,y plane of the image. The reason for calculating HRTEM images at different thicknesses was to show how the GPA method varies with the crystal thickness. As such lattice parameter distribution was calculated for various lattice thicknesses.

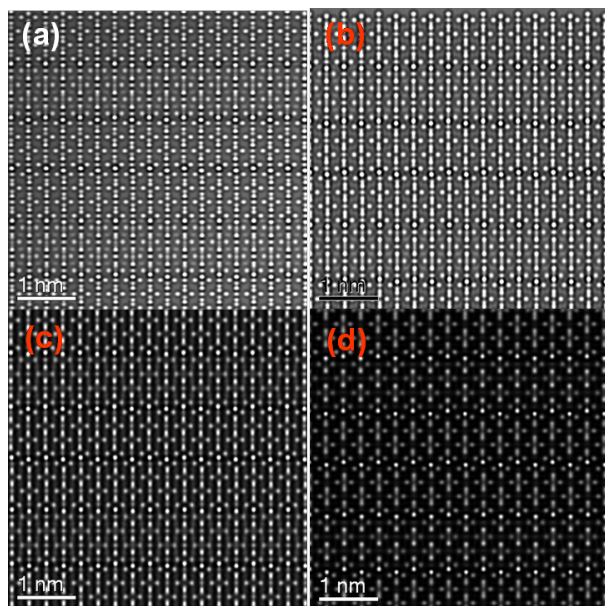


*Figure 8.7: Simulated HRTEM images for various thicknesses layer thicknesses (a) 2 nm (b) 5 nm (c) 10 nm (d) 20 nm*

The lattice parameter distribution for the interplanar distance between (011) planes ( $d_{011}$ ) in  $\text{LiFePO}_4$  and  $\text{FePO}_4$  are shown in Figure 8.8. The lattice profile are shown calculated for varying thicknesses including 2 nm, 5 nm, 10 nm and 20 nm. It can be seen that the structure of the atomic model used to calculate the interface  $\text{LiFePO}_4\text{--FePO}_4\text{--FePO}_4\text{--LiFePO}_4\text{--FePO}_4$  (8.6) can be derived from the distribution of lattice parameters. Two important observations can also be made from the lattice profiles. First, the thinnest sample (2 nm) shows the distribution of both  $\text{LiFePO}_4$  and  $\text{FePO}_4$  phases very well. However, as the thickness increases the interface between  $\text{LiFePO}_4$  and  $\text{FePO}_4$  becomes more diffuse and cannot be determined accurately at high sample thicknesses. This is due to the phenomena of increased delocalization of HRTEM lattice fringes with increased sample thickness. This means that the lattice fringes appear to continue well beyond the edge of a specimen or interface. As a result an interface appears blurred and increases the error of finding the interface position. However the GPA method still shows that two different phases with different lattice parameters are present. At very high thickness however the distinction between the two phases becomes more difficult. Another observation is that the difference between the calculated value of the lattice parameters and the experimental parameter becomes larger with increased thickness. This can be observed clearly in Figure 8.8. The experimental values for  $d_{011}$  are  $\approx 0.3745$  nm for  $\text{LiFePO}_4$  and  $\approx 0.3687$  nm for  $\text{FePO}_4$ .

It should be noted that the obtaining strain profiles from calculated HRTEM images is also characterized by certain problems. Some of the errors encountered in calculating strain from the HRTEM images include the problem of image discretization. This causes the FFT of the HRTEM image to have streaks which

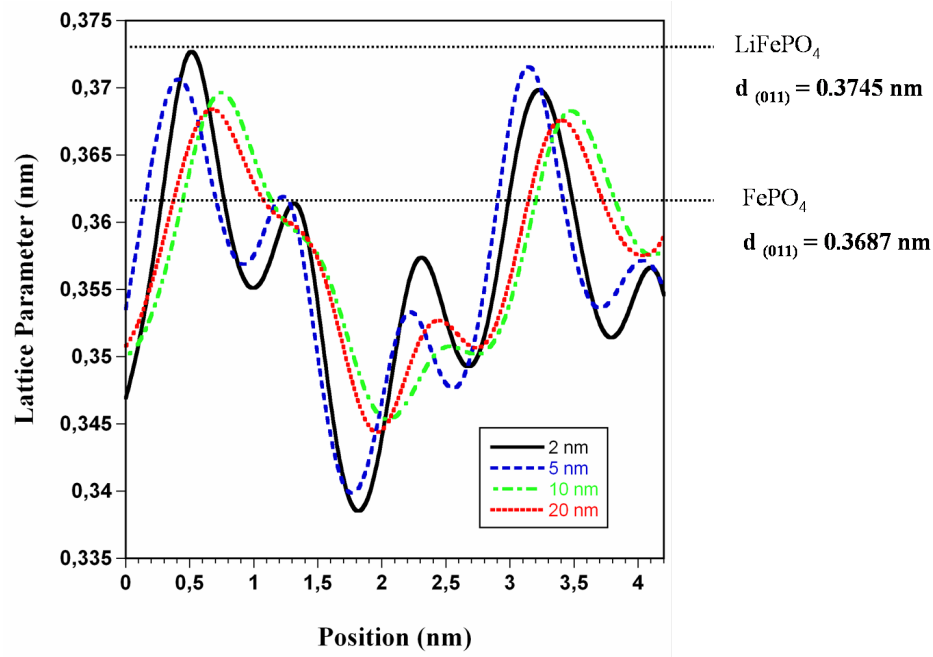


*Figure 8.8: An intensity profile of the distribution of of the (011) lattice parameters in figure 8.6. The experimental interplanar distance between the (011) planes is 0.3745 nm for  $\text{LiFePO}_4$  and 0.3687 nm for  $\text{FePO}_4$ . The profiles are shown for various  $\text{LiFePO}_4 - \text{FePO}_4$  model thicknesses 2 nm, 20 nm and 50 nm.*

interfere in the calculation of the phase images and the lattice parameter distribution. Recalling the introduction to the GPA method which was given in Chapter 3, the calculation of the phase image and the lattice parameter distribution involves selecting a reflection from the FFT of the HRTEM image using a Gaussian or Lorentzian mask. In selecting a reflection the effects of the other reflections should be as small as possible. However with streaking in the FFT pattern it is difficult not to select the intensity of the other spots. This can be seen in Figure 8.9

Selecting a reflection in the FFT of the calculated image (Figure 8.9(a)) is prone to errors since the reflection is not a spot like in the experimental FFT (Figure 8.9(b)). Rather it is streaked and it means the size of the mask used to select the spot is critical. In this case streaking was minimized by multiplying the image with a windowing function, however it was not possible to eliminate this effect. This could have led to systematic errors in the calculation of strain profiles in calculated images. The analysis presented in this section shows that the GPA method is very accurate in showing the phase distribution in various samples. However it was also shown that the method becomes less accurate at large sample thicknesses. The size of the samples examined in these theses have ranged from nanosized particles to particles measuring hundreds of nanometers. The data presented in the results was obtained from many particles of varying sizes. It can be concluded the GPA method gives good description of lattice parameter distribution but not the absolute values of the lattice parameter or the

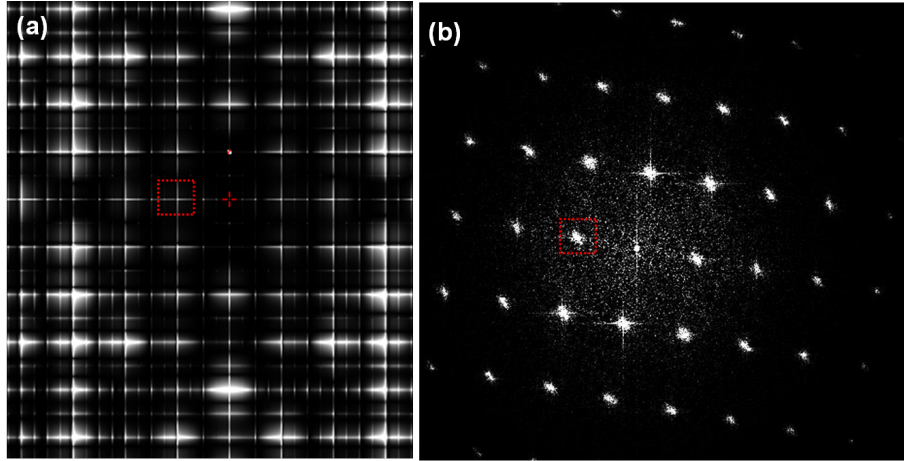


*Figure 8.9: Streaking in the FFT obtained from calculated HRTEM image (a). an experimental HRTEM image is shown in comparison (b). The dotted red squares show single reflections.*

exact position of the interface.

## 8.2.2 Electron beam effects

The second issue that may give rise to inaccuracy is the effect due to the electron beam used in TEM investigations. As shown in earlier sections of this thesis,  $\text{LiFePO}_4$  can suffer from drastic beam damage at the high acceleration voltages common in most TEM instruments. Figure 8.10 a-d shows a time series showing the amorphization of the  $\text{Li}_{0.5}\text{FePO}_4$  grain under exposure to the beam.

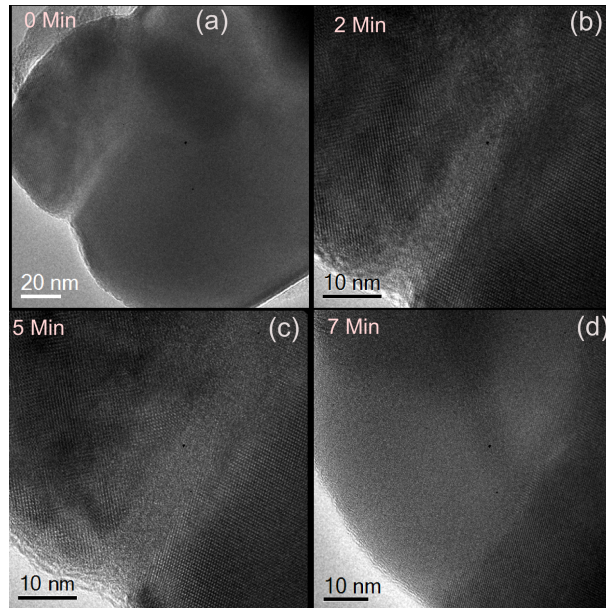


*Figure 8.10: Amorphization of  $\text{Li}_{0.5}\text{FePO}_4$  grain under the electron beam.*



In the beginning the grain is characterized by two large domains separated by an interface (figure 8.10a). The amorphization process is then observed to begin from interface outwards (figure 8.10c-d). After at least 8 minutes the whole grain is amorphous. This phenomena could explain why Chen et al also observed an amorphous interface between the delithiated and lithiated phase [38] which were not observed in this thesis. This also shows that the structure of  $\text{Li}_{(1-x)}\text{FePO}_4$  is highly unstable under the electron beam at high acceleration voltages. According to the results in Chapter 5., at high acceleration voltages one of the main damage mechanisms is the knock-off damage in which case there is a preferential loss of Li atoms from the lattice. To reduce radiation damage the acceleration voltage of the microscope can be lowered. This reduces the kinetic energy of the electrons and reduces damage done on the sample. If this is not possible then the electron dose and exposure times can also be reduced. Examining in greater details the influence of electron beam and stoichiometry on  $\text{LiFePO}_4$  remains one of the future goals.

### 8.3 Conclusion

In this chapter we examined the structural properties of partially delithiated  $\text{Li}_{(0.5)}\text{FePO}_4$  grains using HRTEM analysis. We used the distribution of lattice parameters to show the distribution of the delithiated and lithiated phases in a  $\text{Li}_{(0.5)}\text{FePO}_4$  grain. We have found that partially delithiated grains have both  $\text{FePO}_4$  and  $\text{LiFePO}_4$  phases in the same grain. A phenomenological description of the accuracy of the GPA method the on the large particle  $\text{LiFePO}_4$  samples has also been given. A more quantitative description is one of the future goals. The results obtained in this chapter support the one-dimensional Li transport model as the most likely model of delithiation.



## Part IV

### Final Discussion and Future Outlook





## Final Discussion

In this chapter we present a final discussion of the various results obtained in this thesis. In the light of the main objectives presented in chapter 1, we sought to understand the electronic structure of  $\text{LiFePO}_4$  and the delithiated phase  $\text{FePO}_4$  using EELS and theoretical calculations thesis. We also sought to understand the delithiation mechanism in  $\text{LiFePO}_4$  by examining the structure of partially delithiated  $\text{Li}_{0.5}\text{FePO}_4$ . The results in this thesis can therefore be summarized as

1. Electronic properties of  $\text{LiFePO}_4$  and  $\text{FePO}_4$  and the changes with extraction of Li ions from the lattice. Which were investigated using valence and core-electron energy loss spectroscopy and theoretical calculations.
2. The delithiation mechanism of  $\text{LiFePO}_4$  as obtained from atomic scale mapping of  $\text{LiFePO}_4$  and  $\text{FePO}_4$  phases in partially delithiated samples.

The electronic and structural properties of  $\text{Li}_{1-x}\text{FePO}_4$  are presented in Sec. 9.1 and Sec. 9.2 respectively.

### 9.1 Electronic properties of $\text{Li}_{1-x}\text{FePO}_4$

The electronic properties of  $\text{Li}_{1-x}\text{FePO}_4$  ( $x=0, 0.5, 1$ ) were examined using both theoretical calculation and electron energy loss spectroscopy before and after extraction of Li ions from the lattice. Both core loss and valence electron energy loss spectra were interpreted with the help of bandstructure calculations and theoretical spectra. Electronic structure calculations in chapter 6 showed  $\text{LiFePO}_4$  and  $\text{FePO}_4$  to be insulators. This is in agreement with previous calculations by other

authors [37, 42, 45, 50]. In  $\text{LiFePO}_4$  the energy states at the top of the valence band are dominated by Fe 3d states with minor contribution from O 2p states. These states form the lower Hubbard bands in  $\text{LiFePO}_4$ . The conduction band in  $\text{LiFePO}_4$  shows Fe 3d-O2p dominated states between 4 eV and 7 eV. These states then form the upper Hubbard band in  $\text{LiFePO}_4$ . The electronic states above 6 eV are mainly O2p states hybridized with Fe 4s, P and Li 2s states. Extracting Lithium from the lattice leads to the re-organization of the electronic states such that in  $\text{FePO}_4$  the electronic states at the top of the valence bands are now O2p dominated. The lower Hubbard band is shifted to lower energies in relation to  $\text{LiFePO}_4$  to about -7 eV below the  $E_F$ . The upper Hubbard band is also shifted to lower energies such that between 2-4 eV the energy states are now mainly Fe3d. Above 6 eV the energy states remain the same with Fe 4s, 4p, and O 2p hybridized states. As such  $\text{LiFePO}_4$  could be characterized as a Mott-Hubbard insulator while  $\text{FePO}_4$  could be considered to be a charge-transfer insulator.

This picture of the changes in the electronic structure with delithiation was then investigated using experimentally using electron energy spectroscopy. This thesis presents for the first time a detailed analysis of the valence electron energy loss spectra (VEELS) for  $\text{Li}_{(1-x)}\text{FePO}_4$ .  $\text{FePO}_4$  VEELS spectra were characterized by peaks between 4-20 eV. These peaks were either missing in  $\text{LiFePO}_4$  or had much less intensity. These differences between the  $\text{LiFePO}_4$  and  $\text{FePO}_4$  VEELS spectra were also reproduced in calculated energy loss functions and dielectric functions,  $\epsilon_1$  and  $\epsilon_2$ . Analysis of these peaks features showed that they were due to inter-band transitions from the bands at the top of the valence band to the bands at the bottom of the conduction band. The origin of these interband transitions was also determined through band-by-band analysis of the theoretical  $\epsilon_2$  curves for  $\text{LiFePO}_4$  and  $\text{FePO}_4$ . This analysis showed that the observed peaks in the  $\text{FePO}_4$  VEELS spectra were as a result of inter-band transitions from the O-2p dominated states at the top of the valence band to the Fe 3d dominated states at the bottom of the conduction band. This confirmed the results obtained from band structure calculations that the extraction of Li ions leads to the shift of the Fe 3d-O2p hybridized bands in the conduction band to lower energies. Interband transitions from the valence band to these hybridized states leads to the observed peaks in  $\text{FePO}_4$  VEELS. Hence, the inter-band transitions observed in  $\text{FePO}_4$  indicate the re-organization of the electronic structure with delithiation.

Changes in the fine structure of the ionization edges were also observed in the O-K edge and the  $\text{FeL}_{2,3}$  edges. The O-K edge was characterized by a pre-edge peak whenever Li ions were extracted from the  $\text{LiFePO}_4$  lattice. This pre-edge peak was only observed in the EELS spectra of  $\text{FePO}_4$  and not in  $\text{LiFePO}_4$ . It was shown that the pre-edge peak also exists in  $\text{LiFePO}_4$  however it shifted 1-2 eV from the threshold of the main O-K peaks and as such it is hidden within the main O-K edge. Delithiation in  $\text{LiFePO}_4$  causes the 3d bands to be shifted to lower energies. This makes the pre-edge peak visible in the EELS spectra of  $\text{FePO}_4$ . The pre-edge

peak position is therefore related to the shift in the 3d bands with the delithiation. The intensity of the peak is on the other hand related to the changes in the hybridization with the extraction of Li ions from the system. Adding/removing one lithium atom will roughly transfer/remove one electron to/from the Fe 3d band. This will reduce/increase the number of empty 3d levels and consequently change the intensity of the pre-edge peak. The Fe  $L_{2,3}$  edge also showed changes which reflected the re-organization of the electronic structure with delithiation. Extraction of Li ions from the lattice was characterized by the chemical shift of the Fe  $L_{2,3}$  with delithiation. The explanation for this energy shift has to do with the change of the valence electron distribution around the Fe ion with delithiation. The oxidation of  $Fe^{2+}$  to  $Fe^{3+}$  with delithiation, results in the decrease of valence charge density around the transition metal ion which results in a reduced screening of its nuclear field and subsequently results in positive shift [60,139]. These changes in the  $FeL_{2,3}$  position are related to the shift in the Fe 3d band to lower energies which was observed in the electronic structure calculations and at the O-K edge. VEELS results, bandstructure calculations and core-loss spectra show that  $FePO_4$  could be considered to be a charge-transfer insulator and  $LiFePO_4$  could be taken to be Mott-Hubbard insulator.

## 9.2 Delithiation mechanism in $LiFePO_4$

As was mentioned in the introduction the exact mechanism of Li extraction and insertion is still not completely understood. And therefore one of the goals in this thesis was to gain some insight on the delithiation mechanism in  $LiFePO_4$ . In order to summarize the results obtained in this section it is essential to recall the various existing delithiation models. These include the core-shell model where the delithiation process starts from the surface of the  $LiFePO_4$  grain with the delithiated phase  $FePO_4$  phase forming a core around the undelithiated  $LiFePO_4$  shell. The second model was the one-dimensional model it is argued that the Li ions are extracted through channels parallel to the  $\langle 010 \rangle$  crystal direction. According to this model the delithiation process should result in the formation of both phase separated by a phase interface perpendicular to the delithiation direction. The third model is known as domino cascade model in which case it is argued that the delithiation process occurs rapidly faster than the nucleation of the any phase such that at a partial delithiated state the grain is either fully delithiated or partially delithiated. One way to examine these models is to investigate the structural properties and phase characteristics of partially delithiated grains. If any or all of these models are correct then an investigation of the partially delithiated grains using atomic-structure methods such as  $LiFePO_4$  should show the phase distribution. Chapter 8 presents the results on the atomic scale mapping of the structure in partially delithiated  $LiFePO_4$ . It was shown that in partially delithiated grains the delithiated phases and undelithiated phases do co-exist in the same

grain. From the distribution of the observed phases, it was also observed that the two phases formed domain-like structures in the grains. This observation does not agree with both core-shell and domino models and agrees more with the one dimensional model as proposed by Chen et al [38]. The observation by Chen et al [38] that the delithiated phase and the undelithiated phase are separated by an amorphous/disordered interface was however not observed in this case. Their observation of an amorphous interface could be due to the electron beam damage which causes amorphization of the grains which starts from the interface. The effects of the electron on the structure will be investigated further in the future

## 9.3 Electron beam effects

This thesis showed that  $\text{LiFePO}_4$  undergoes significant chemical and physical changes due to the electron beam under certain experimental conditions. It was shown in Chapter 6 that high beam energies (300 kV) lead to a dramatic decrease in the intensity of the Li K edge. This was attributed to the mass loss of Li atoms from the lattice due to the electron beam. It was shown that this could be avoided by reducing the accelerating voltage to 80 kV. This essentially decreases the kinetic energy of the incident electron and avoids physical damage to the sample. However it also shown that at high electron current/doses and exposure times lead to chemical damage (ionization damage) even at low accelerating voltages. In order to reduce these forms of damage care was therefore taken to reduce electron dose, exposure times and accelerating voltage.

## 9.4 Future Outlook

### 9.4.1 Electron beam induced damages on $\text{LiFePO}_4$

The most pressing issue that has to be addressed in greater details should be the effects of the electron beam on the crystal structure and electronic structure of the lithium containing materials. The points to address include

- The knock-on threshold for light atoms including Li, O and P in  $\text{LiFePO}_4$
- The maximum electron dose needed to avoid beam damage in the sample
- The mechanism of beam induced damage at low acceleration voltages

### 9.4.2 Momentum dependent EELS

As shown in Chapter 3, the momentum loss in EELS can vary with crystallographic orientation in anisotropic materials.  $\text{LiFePO}_4$  and  $\text{FePO}_4$  are anisotropic materials and this means the electronic structure varies with the direction of the crystal. In this thesis the direction dependence of the EELS spectra was not investigated since

the experimental spectra were obtained from polycrystalline samples. Momentum dependent investigations can be only done using single crystal samples. At the moment single crystal samples of  $\text{FePO}_4$  are not available. It is therefore of interest to grow single crystals of both phases and subsequently study the momentum dependence of the EELS spectra.



## References

- [1] M.Winter and R.J. Brodd. What are batteries, fuel cells, and supercapacitors. *Chemical Review*, 104:4245–4269, 2004.
- [2] C.Julien. *Design Considerations for Lithium batteries*, pages 1–21. Kluwer Academic press, Doderecht, Netherlands, 1999.
- [3] J. Molenda. Lithium ion batteries - state of art. novel phospho-olivine cathode materials. *Materials Science - Poland*, 24:61, 2006.
- [4] M. S.Whittingham. Lithium batteries and cathode materials. *Chem. Rev.*, 104:4271–4301, 2004.
- [5] Y.S.Meng and M. Elena Arroyo de Dompablo. First principles computational materials design for energy storage materials in lithium ion batteries. *Energy and Enviromental Science*, 2:589, 2009.
- [6] J.M.Tarascon. *Better electrode materials for energy applications through chemistry*, pages 1–21. Kluwer Academic press, Doderecht, Netherlands, 1999.
- [7] W. Weppner. *Chemical stability of high performance lithium batteries*, pages 1–21. Kluwer Academic press, Doderecht, Netherlands, 1999.
- [8] M.S. Whittingham, Y.Song, S.Lutta, P.Y.Zavalij, and N.A. Chernova. Some transition metal (oxy)phosphates and vanadium oxides for lithium batteries. *Journal of Materials Chemistry*, 15:3362–3379, 2005.
- [9] A. Mannthiram. *Smart Battery Materials*, pages 8/1–8/7. CRC Press, Boca Raton, 1939.

- [10] A. K. Padhi, K. S. Nanjundaswamy, and J. B. Goodenough. Phospho-olivines as positive-electrode materials for rechargeable lithium batteries. *J. Electrochem. Soc.*, 144:1188, 1997.
- [11] V. A. Streltsov, E. L. Belokoneva, V. G. Tsirelson, and N. K. Hansen. Multi-pole analysis of the electron density in triphylite,  $\text{LiFePO}_4$ , using x-ray diffraction data. *Acta Cryst.*, B49:153–158, 1993.
- [12] G. Rousse, J. Rodriguez-Carvajal, S. Patoux, and C. Masquelier. Magnetic structures of the triphylite  $\text{LiFePO}_4$  and of its delithiated form  $\text{FePO}_4$ . *Acta Cryst.*, 15:4082–4090, 2003.
- [13] C. N. R. Rao. Transition metal oxides. *Annual Review of Physical Chemistry*, 40:291–326, 1989.
- [14] R. Gross and A. Marx. Spinelektronik. *Vorlesungsskript, Walther-Meissner-Institut*, 2:589, SS 2004.
- [15] A. S. Andersson, B. Kalska, L. Haggstrom, and J. O. Thomas. Lithium extraction/insertion in  $\text{LiFePO}_4$ : an x-ray diffraction and mössbauer spectroscopy study. *Solid State Ionics*, 130:41–52, 2000.
- [16] F. Bloch. Bemerkung zur elektronentheorie des ferromagnetismus und der elektrischen leitfähigkeit. *Z. Phys.*, 57:545, 1929.
- [17] A. H. Wilson. The theory of electronic semi-conductors. *Proc. Roy. Soc. A*, 133:458–491, 1931.
- [18] H. J. de Boer and E. J. W. Verwey. Semi-conductors with partially and with completely filled 3d-lattice bands. *Proc. Roy. Soc. A*, 49:59–71, 1937.
- [19] N. F. Mott. The basis of the electron theory of metals, with special reference to the transition metals. *Proc. Roy. Soc. A*, 62:416–422, 1949.
- [20] J. Hubbard. Electron correlations in narrow energy bands. *Proc. Roy. Soc. A*, 276:238–257, 1963.
- [21] J. Zaanen, G. A. Sawatzky, and J.W. Allen. Band gaps and electronic structure of transition-metal compounds. *Phys. Rev.Lett*, 64:2442, 1985.
- [22] M. Winter, J.O. Besenhard, M.E. Spahr, and P. Novak. Insertion electrode material for re-chargeable lithium batteries. *Advanced Materials*, 10:725–763, 1998.
- [23] M.S Islam, D. Driscoll, C.A.J. Fisher, and P.R Slater. Atomic-scale investigation of defects, dopants and lithium transport in the  $\text{LiFePO}_4$  olivine-type battery material. *Chem. Mater*, 17:5085–5092, 2005.
- [24] N. Ravet, J.F. Magnan, S. Besner, M. Gauthier, and M. Armand. Electroactivity of natural and synthetic triphylite. *Journal of Power Sources*, 97-8:503–507, 2004.



- [25] A. Yamada, S. C. Chung, and K. Hinokuma. Optimized  $\text{LiFePO}_4$  for lithium battery cathodes. *J. Electrochem. Soc.*, 148:A224–A229, 2001.
- [26] R. Dominko, M. Gaberseck, A. Bele, D. Mihailovic, and J. Jamnik. Carbon nanocoatings on active materials for li-ion batteries. *J. Eur. Ceram. Soc.*, 27:909–913, 2007.
- [27] D. Morgan, A. Van der Ven, and G. Ceder. Li conductivity in  $\text{Li}_x\text{MPO}_4$  ( $\text{M} = \text{Mn, Fe, Co, Ni}$ ) olivine materials. *Electrochem. Solid State Lett.*, 7:A30–A32, 2004.
- [28] S.P. Herle, B. Ellis, N. Coombs, and L.F. Nazar. Nano-network electronic conduction in iron and nickel olivine phosphates. *Nature Mater.*, 3:147–152, 2002.
- [29] M. Whittingham, Jing-Dong Guo, Rongji Chen, T. Chirayil, G. Janauer, and P. Zavalij. The hydrothermal synthesis of new oxide materials. *Solid state ionics*, 75:257–268, 1995.
- [30] G. Arnold, J. Garche, R. Hemmer, S. Ströbele, C. Vogler, and M. Wohlfahrt-Mehrens. Fine-particle lithium iron phosphate  $\text{LiFePO}_4$  synthesized by a new low-cost aqueous precipitation technique. *Journal of Power Sources*, 119-121:247–251, 2003.
- [31] G. Arnold, J. Garche, R. Hemmer, S. Ströbele, C. Vogler, and M. Wohlfahrt-Mehrens. Comparison between different  $\text{LiFePO}_4$  synthesis routes and their influence on its physico-chemical properties. *Journal of Power Sources*, 119-121:252–257, 2003.
- [32] J. Dodd, R. Yazami, and B. Fultz. Phase diagram of  $\text{Li}_x\text{FePO}_4$ . *Electrochem. Solid-State Lett.*, 9:A151–A155, 2006.
- [33] A. S. Andersson, J. O. Thomas, B. Kalska, and L. Haggstrom. Thermal stability of  $\text{LiFePO}_4$ -based cathodes. *Electrochem. Solid-State Lett.*, 3:66–68, 2000.
- [34] J.M. Tarascon C. Masquelier C. Delacourt, P. Poizot. The existence of a temperature-driven solid solution in  $\text{Li}_x\text{FePO}_4$  for  $0 \leq x \leq 1$ . *Nature Mater.*, 4:254, 2005.
- [35] F. Zhou, T. Maxisch, and G. Ceder. Configurational electronic entropy and the phase diagram of mixed-valence oxides: The case of  $\text{Li}_x\text{FePO}_4$ . *Phys. Rev. Lett.*, 97:155704, 2006.
- [36] C. Delmas, M. Maccario, L. Croguennec, F. Le Cras, and F. Weill. Lithium deintercalation in  $\text{LiFePO}_4$  nanoparticles via a domino-cascade model. *Nature Mater.*, 7:665–671, 2008.
- [37] A. Augustsson, G. V. Zhuang, S. M. Butorin, J. M. Osorio-Guillen, C. L. Dong, R. Ahuja, C. L. Chang, P. N. Ross, J. Nordgren, and J.-H. Guo.

- Electronic structure of phospho-olivines  $\text{Li}_x\text{FePO}_4$  ( $x=0,1$ ) from soft-x-ray-absorption and -emission spectroscopies. *Journal of Chemical Physics*, 123:1847171–1847179, 2005.
- [38] G. Chen, X. Song, and T. J. Richardson. Electron microscopy study of the  $\text{LiFePO}_4$  to  $\text{FePO}_4$  phase transition. *Electrochem. Solid-State Lett.*, 9:A295–A298, 2006.
- [39] H. Gabrisch, J. Wilcox, and M. M. Doeff. Tem study of fracturing in spherical and plate-like  $\text{LiFePO}_4$  particles. *Electrochemical and Solid-State Letters*, 11:A25–A29, 2008.
- [40] N. Meethong, Y.-H. Kao, M. Tang, H.-Y. Huang, W. C. Carter, and Y.-M. Chiang. Electrochemically induced phase transformation in nanoscale olivines  $\text{Li}_{1-x}\text{MPO}_4$  ( $\text{M} = \text{Fe, Mn}$ ). *Chem. Mater.*, 20:6189–6198, 2008.
- [41] V. Srinivasan and J. Newman. Discharge model for the lithium iron-phosphate electrode. *Journal of Electrochemical Society*, 151:A1517–A1529, 2004.
- [42] P. Tang and N. A. W. Holzwarth. Electronic structure of  $\text{FePO}_4$ ,  $\text{LiFePO}_4$ , and related materials. *Physical Review B*, 68:165107, 2003.
- [43] J. Jiang, C. Ouyang, H. Li, Z. Wang, X. Huang, and L. Chen. First-principles study on electronic structure of  $\text{LiFePO}_4$ . *Solid State Communications*, 143:144–148, 2007.
- [44] C. Ouyang, S. Shi, Z. Wang, X. Huang, and L. Chen. First-principles study of Li ion diffusion in  $\text{LiFePO}_4$ . *Physical Review B*, 69:104303, 2004.
- [45] F. Zhou, K. Kang, T. Maxisch, G. Ceder, and D. Morgan. The electronic structure and band gap of  $\text{LiFePO}_4$  and  $\text{LiMnPO}_4$ . *Solid State Communications*, 132:181–186, 2004.
- [46] A. J. Bosman and H. J. van Daal. Small-polaron versus band conduction in some transition-metal oxides. *Advances in Physics*, 77:1 – 117, 1970.
- [47] I. G. Austin and N. F. Mott. Polarons in crystalline and non-crystalline materials. *Advances in Physics*, 71:41 – 102, 1969.
- [48] Miao Shu, M. Kocher, P. Rez, F. Bultz, R. Yazami, and C. C. Ahn. Local electronic structure of olivine phases of  $\text{Li}_x\text{FePO}_4$ . *Journal of physical chemistry. A*, 111:4242–4247, 2007.
- [49] W. Sigle, R. Amin, K. Weichert, P. A. van Aken, and J. Maier. Delithiation study of  $\text{LiFePO}_4$  crystals using electron energy-loss spectroscopy. *Electrochem. Solid-State Lett.*, 12:A151–A154, 2009.
- [50] P. Moreau, V. Mauchamp, and F. Boucher. Fast determination of phases in  $\text{Li}_x\text{FePO}_4$  using low losses in electron energy-loss spectroscopy. *Applied Physics Letters*, 94:123111–123114, 2009.

- [51] L. Laffont, C. Delacourt, P. Gibot, M. Y. Wu, P. Kooyman, C. Masquelier, and J. M. Tarascon. Study of the  $\text{LiFePO}_4/\text{FePO}_4$  two-phase system by high-resolution electron energy loss spectroscopy. *Chem. Mater.*, 18:5520, 2006.
- [52] D.X. Gouveia, V. Lemos, J.A.C. de Paiva, A.G.S. Filho, J. M. Filho, S.M. Lala, L.A. Montoro, and J.M Rosolen. Spectroscopic studies of  $\text{Li}_x\text{Fe}_{0.03}\text{Fe}_{0.97}\text{PO}_4$  ( $x = \text{Cr, Cu, Al, Ti}$ ). *Phys. Rev. B*, 72(2):024105, Jul 2005.
- [53] A. Hunt, W.-Y. Ching, Y.-M. Chiang, and A. Moewes. Electronic structures of  $\text{LiFePO}_4$  and  $\text{FePO}_4$  studied using resonant inelastic x-ray scattering. *Physical Review B*, 73:205120, 2006.
- [54] M.C. Tucker, M.M Doerff, T.J. Richardson, R. Finones, E.J. Cairns, and J.A. Reimer. Hyperfine fields at the Li site in  $\text{LiFePO}_4$ -type olivine materials for lithium rechargeable batteries: A  $^7\text{Li}$  mas nmr and squid study. *Journal of American Chemical Society*, 124:3832–3833, 2002.
- [55] David B. Williams and C. Barry Carter. *Transmission Electron Microscopy, Basics I*. Springer, 1996.
- [56] J. M. Howe B. Fultz. *Transmission Electron Microscopy and Diffraction of Materials*. Springer, 2002.
- [57] Marc de Graef. *Introduction to Conventional Transmission Electron Microscopy*. Cambridge University Press, 2003.
- [58] David B. Williams and C. Barry Carter. *Transmission Electron Microscopy, Diffraction II*. Springer, 1996.
- [59] R. F. Egerton. Electron energy-loss spectroscopy in the tem. *Rep. Prog. Phys.*, 72:016502–016527, 2009.
- [60] R.F. Egerton. *Electron Energy-Loss Spectroscopy in the Electron Microscope*. Plenum Press New York and London, 1996.
- [61] G. A. Botton, C. B. Boothroyd, and W. M. Stobbs. Momentum dependent energy loss near edge structure using ctem: the reliability of the methods available. *Ultramicroscopy*, 59:93–107, 1994.
- [62] R. D. Leapman, P. L. Fejes, and J. Silcox. Orientation dependence of core edges from anisotropic materials determined by inelastic scattering of fast electrons. *Phys. Rev. B*, 28:2361–2373, 1983.
- [63] R. D. Leapman and J. Silcox. Orientation dependence of core edges in electron-energy-loss spectra from anisotropic materials. *Phys. Rev. Lett*, 42:1361–1364, 1979.
- [64] H. Bethe. Zur theorie des durchgangs schneller korpuskularstrahlung durch materie. *Annalen der Physik*, 3:325–400, 397.
- [65] R. H. Ritchie. Plasma losses by fast electrons in thin films. *Physical Review*, 106, 1957.

- [66] Mitio Inokuti. Inelastic collisions of fast charged particles with atoms and molecules - the bethe theory revisited. *Reviews of Modern Physics*, 43, Number 3, 1971.
- [67] R. D. Leapman, L. A. Grunes, and P. L. Fejes. Study of the  $l_{2,3}$  edges in the 3d transition metals and their oxides by electron-energy-loss spectroscopy with comparisons to theory. *Phys. Rev. B*, 26:614–635, 1982.
- [68] W. Sigle. Analytical transmission electron microscopy. *Annual Review of Materials Research*, 35:239–314, 2005.
- [69] I.Egri. Trends in the plasmon dispersion of insulators and semiconductors. *J.Phys. C: Solid State Phys.*, 18:1191–1196, 1985.
- [70] H.R. Philipp and H. Ehrenreich. Optical of semiconductors. *Physical Review*, 129:1550–1560, 1963.
- [71] E. Kröger. Transition radiation, cerenkov radiation and energy losses of relativistic charged particles traversing thin foils at oblique incidence. *Zeitschrift für Physik*, 235:403–421, 1970.
- [72] D.Pines. *Elementary excitations in solids*. Perseus books, 1966.
- [73] J.Fink. *Recent developments in Energy Loss Spectroscopy*, pages 122–226. Academic Press, Massachussets, 1989.
- [74] Paul Drude. Zur elektronentheorie der metalle. *Annalen der Physik*, 306, 1900.
- [75] W.Tews and R. Gründler. Electron-energy-loss spectroscopy of  $al_2o_3(i)$ . *phys.stat.sol. (b)*, 109:255–264, 1982.
- [76] M. Stöger-Pollach. Optical properties and bandgabs from low loss eels: Pitfalls and solutions. *Micron*, 2008.
- [77] J. Silcox C. H. Chen and R. Vincent. Electron-energy losses in silicon: Bulk and surface plasmons and cerenkov radiation. *Phys. Rev. B*, 197:64–71, 1975.
- [78] N.Martensson and A. Nilsson. On the origin of core-level binding energy shifts. *Journal of Electron Spectroscopy and Related Phenomena*, 75:209–223, 1995.
- [79] R. F. Egerton, B. G. Williams, and T.G. Sparrow. Fourier deconvolution of electron energy-loss spectra. *Proceedings of the Royal Society London A*, 398:395–404, 1985.
- [80] E. Zeitler D. S. Zu. Background problem in electron-energy-loss spectroscopy. *Physical Review B*, 47, 1992.
- [81] M.G.Bell and W.Y. Liang. Electron energy loss studies in solids; the transition metal dichalcogenides. *Advances in physics*, 25:53–86, 1976.

- [82] J.Pflüger and J. Fink. *Determination of optical constants by high resolution electron energy loss spectroscopy(EELS)*, pages 42–80. Academic press, Massachussets, 1991.
- [83] D. Van Dyck. *High-Resolution Electron Microscopy*, pages 8/1–8/7. CRC Press, Boca Raton, 1939.
- [84] Michael A. O’Keefe. Seeing atoms with aberration-corrected sub-angstrom electron microscopy. *ultramicroscopy*, page 196, 2008.
- [85] O. Sherzer. Seeing atoms with aberration-corrected sub-angstrom electron microscopy. *J. App. Phys.*, 20:20, 1949.
- [86] S.Uhlemann E.Schwan B.Kabius M. Haider, H.Rose and K.Urban. A spherical-aberration-corrected 200 kv transmission electron microscope. *Ultramicroscopy*, 75(1):53, October 1998.
- [87] J.C.H. Spence. *High Resolution Electron Microscopy*. Oxford Science Publications, 2003.
- [88] M.J. Hytch, E. Snoeck, and R. Kilaas. Quantitative measurement of displacement and strain fields from hrem micrographs. *Ultramicroscopy*, 74:131–146, 1998.
- [89] S. Kret, P. Ruterana, A. Rosenauer, , and D. Gerthsen. Extracting quantitative information from high resolution electron microscopy. *Phys. stat. sol.*, 227:247–295, 2001.
- [90] E. Snoeck, B. Warot, H. Ardhuin, A. Rocher, M.J. Casanove, R. Kilaas, and M.J. Hytch. Quantitative analysis of strain field in thin films from hrtem micrographs. *Thin Solid Films*, 319:157–162, 1998.
- [91] M. J. Hytch, J-L. Putaux, and J-M. Penisson. Measurement of the displacement field around dislocations to 0.03Å by electron microscopy. *Nature*, 423:270–273, 2003.
- [92] A.C. Larson and R.B. von Dreele. *GSAS. Report No. LAUR 86-748*. Los Alamos National Laboratory, New Mexico, 2000.
- [93] P. Hohenberg and W. Kohn. Inhomogeneous electron gas. *Physical Review*, 136:864–871, 2005.
- [94] W. Kohn and L.J Sham. Self-consistent equations including exchange and correlation effects. *Physical Review*, 140:A1133–A1138, 1965.
- [95] D. Singh. *Planewaves, Pseudopotentials and the LAPW Method*. Kluwer Academic Publishers, Boston/Dordrecht/London, 1994.
- [96] C. J. Pickard. *An initio Electron Energy Loss Spectroscopy*. PhD thesis, Christ’s College and Cambridge University, 1997.
- [97] M. Weinert, E. Wimmer, and A. J. Freeman. Total-energy all-electron density functional method for bulk solids and surfaces. *Physical Review*, 26:4571–4578, 1982.

- [98] E. Wimmer, H. Krakauer, M. Weinert, and A. J. Freeman. Full-potential self-consistent linearized-augmented-plane-wave method for calculating the electronic structure of molecules and surfaces: O<sub>2</sub> molecule. *Physical Review*, 24:864–875, 1981.
- [99] O. K. Andersen. Linear methods in band theory. *Phys. Rev. B*, 12:3060, 1975.
- [100] J. C. Slater. Wave functions in a periodic potential. *Physical Review*, 51:546, 1937.
- [101] P. Blaha, K. Schwarz, G. K. H. Madsen, D. Kvaniscka, and J. Luitz. *WIEN2k, An Augmented Plane Wave + Local Orbitals Program for Calculating Crystal Properties*. K. Schwarz and Techn. Universität Wien, Austria,, 2001.
- [102] D. S. Sholl and J. A. Steckel. *Density Functional Theory: A Practical Introduction*. Wiley, 2009.
- [103] K. Zeppenfeld. Anisotropie der plasmaschwingungen in graphit. *Zeitschrift für Physik*, 211:391–399, 1968.
- [104] C. Ambrosch-Draxl and J. O. Sofo. Linear optical properties of solids within the full-potential linearized augmented planewave method. *Computer Physics Communications*, 175:1–14, 2006.
- [105] Frederic Wooten. *Optical Properties of Solids*. Academic Press, 1972.
- [106] F. de Groot and A. Kotani. *Core Level Spectroscopy of Solids*. Taylor And Francis, 2008.
- [107] N. Vast, L. Reining, V. Olevano, P. Schattschneider, and B. Jouffrey. Local field effects in the electron energy loss spectra of rutile tio<sub>2</sub>. *Phys. Rev.Lett*, 88:037601–1–037601–4, 2002.
- [108] V. Mauchamp, P. Moreau, G. Ouvrard, and F. Boucher. Local field effects at li k edges in electron energy-loss spectra of li, li<sub>2</sub>o and lif. *Phys. Rev.B*, 77:045117, 2008.
- [109] J. Luitz. *Simulation of core level spectra using Density Funcional Theory*. PhD thesis, Technischen Universität Wien, 2006.
- [110] C. Hebert. Practical aspects of running the wien2knext term code for electron spectroscopy. *Micron*, 38:12–28, 2007.
- [111] F. de Groot. High-resolution x-ray emission and x-ray absorption spectroscopy. *Chem. Rev*, 101:1779–1808, 2001.
- [112] W.T. Silfvast. *Laser Fundamentals*. Cambridge University Press, 2004.
- [113] F. de Groot. Multiplet effects in x-ray spectroscopy. *Coordination Chemistry Reviews*, 249:31–63, 2005.

- [114] L. A.J. Garvie and A. J. Craven. Electron-beam-induced reduction of  $\text{Mn}^{4+}$  in manganese oxides as revealed by parallel eels. *Ultramicroscopy*, 54:83–92, 1994.
- [115] N. Jiang and J. C.H. Spence. Electron irradiation induced phase decomposition in alkaline earth multi-component oxide glass. *J. App. Phys*, 92:2310–2317, 2002.
- [116] J. Cazaux. Correlations between ionization radiation damage and charging effects in transmission electron microscopy. *Ultramicroscopy*, 60:411–425, 1995.
- [117] Ludwig Reimer. *Transmission Electron Microscopy*. Springer, 1997.
- [118] A. Krol, C.S. Lin, Z.H. Ming, C.J. Sher, Y.H. Kao, C.T.Chen, F. Sette, Y. Ma, G.C. Smith, Y.Z. Zhu, and D.T. Shaw. X-ray-absorption studies of y-ba-cu-o and bi-sr-ca-cu-o films at oxygen k edge by means of fluorescence and total electron yield: A comparison of two techniques. *Phys. Rev. B*, 42:2635–2638, 1990.
- [119] J. Fink, N. Nuecker, E. Pellegrin, H. Romberg, M. Alexander, and M. Knupfer. Electron energy-loss and x-ray absorption spectroscopy of cuprate superconductors and related compounds. *J. Electr. Spectro. Relat. Phenom.*, 66:395–452, 1994.
- [120] P. Kuiper, G. Kruizinga, J. Ghijsen, M. Grioni, P. J. Weijs, F. M. de Groot, G. A. Sawatzky, H. Verweij, L. F. Feiner, and H. Petersen. X-ray absorption study of the o 2p hole concentration dependence on o stoichiometry in yba2cu3ox. *Phys. Rev. B*, 38:6483–6489, 1988.
- [121] N. Nuecker, H. Romberg, X.X. Xi, J. Fink, B. Gegenheimer, and Z.X. Zhao. Symmetry of holes in high-tc superconductors. *Phys. Rev. B*, 39:6619–6629, 1989.
- [122] N. Nücker, J. Fink, J. C. Fuggle, P. J. Durham, and W. M. Temmerman. Evidence for holes on oxygen sites in the high-tc superconductors  $\text{La}_{2-x}\text{Sr}_x\text{CuO}_4$  and  $\text{YBa}_2\text{Cu}_3\text{O}_{7-y}$ . *Phys. Rev. B*, 37:5158–5163, 1988.
- [123] N. Jiang and J. C.H. Spence. Interpretation of oxygen k pre-edge peak in complex oxides. *Ultramicroscopy*, 106:215–219, 2006.
- [124] M. Grioni, M. T. Czyzyk, F. M. de Groot, J. C. Fuggle, , and B. E. Watts. Unoccupied electronic states of cuo: An oxygen 1s x-ray-absorption spectroscopy investigation. *Phys. Rev. B*, 39:4886–4890, 1989.
- [125] F. M. F. de Groot, M. Grioni, J. C. Fuggle, J. Ghijsen, G. A. Sawatzky, and H. Petersen. Oxygen k near-edge fine structure: An electron-energy-loss investigation with comparisons to new theory for selected 3d transition-metal oxides. *Phys. Rev. B*, 25:7157–7173, 1982.

- [126] F. M. F. de Groot, M. Grioni, J. C. Fuggle, J. Ghijsen, G. A. Sawatzky, and H. Petersen. Oxygen 1s x-ray-absorption edges of transition-metal oxides. *Phys. Rev. B*, 40:5715–5723, 1988.
- [127] M. L. Knotek and Peter J. Feibelman. Ion desorption by core-hole auger decay. *Phys. Rev. Lett.*, 40:964–967, 1978.
- [128] M.C. Nichols eds. J.W. Anthony, K.W. Bladh. *Handbook of Mineralogy*. Mineral Data Publishing, 1990.
- [129] W.Y.Liang and S.L. Cundy. Electron energy loss studies of the transition metal dichalcogenides. *Philosophical magazine*, page 1031, 1969.
- [130] H.Ikeno, F. M. F. de Groot, E. Stavitski, and I. Tanaka. Multiplet calculations of  $l_{2,3}$  x-ray absorption near-edge structures for 3d transition-metal compounds. *J. Phys: Condens. Matter*, 21:104208, 2009.
- [131] L. A. Grunes, R. D. Leapman, C. N. Wilker, R. Hoffmann, and A. B. Kunz. Oxygen k near-edge fine structure: An electron-energy-loss investigation with comparisons to new theory for selected 3d transition-metal oxides. *Phys. Rev. B*, 25:7157–7173, 1982.
- [132] F. M. F. de Groot, M. Abbate, J. van Elp, G. A. Sawatzky, Y. J. Ma, C. T. Chen, and F. Sette. Oxygen 1s and cobalt 2p x-ray absorption of cobalt oxides. *J. Phys: Condens. Matter*, 5:277–2288, 1993.
- [133] J.P. Crocombette and F. Jollet. Covalency effect on cation 2p x-ray absorption spectroscopy in 3d transition metal oxides. *J.Phys. Condes. Matter*, 8:5253–5268, 1996.
- [134] J. van Elp, J. L. Wieland, H. Eskes, P. Kuiper, G. A. Sawatzky, F. M. F. de Groot, and T. S. Turner. Electronic structure of coo, li-doped coo, and licoo2. *Phys. Rev. B*, 44:6090, 1991.
- [135] W. S. Yoon, K. B. Kim, M. G. Kim, M. K. Lee, H. J. Shin, J. M. Lee, J. S. Lee, and C. H. Yo. Oxygen contribution on li-ion intercalation-deintercalation in licoo2 investigated by o k-edge and co l-edge x-ray absorption spectroscopy. *J. Phys. Chem.B*, 106:2526, 2002.
- [136] M. G. Kim, H. J. Shin, J. H. Kim, S. H. Park, and Y. K. Sun. Xas investigation of inhomogeneous metal-oxygen bond covalency in bulk and surface for charge compensation in li-ion battery cathode  $li[ni_{1/3}co_{1/3}mn_{1/3}]o_2$  material. *J. Electrochem. Soc.*, 152:A1320, 2005.
- [137] G. van der Laan K.T. Moore. Nature of the 5f states in actinide metals. *Review of Modern Physics*, 81(1):235–291, Jul 2009.
- [138] F. M. F. de Groot, Z.W. Hu, M.F. Lopez, G. Kaindl, F. Guillot, and M. Tronc. Difference between  $l_3$  and  $l_2$  x-ray absorption spectra of transition metal compounds. *J. Chem. Phys*, 101:15, 1994.



- [139] D.A. Muller. Simple model for relating eels and xas spectra of metals to changes in cohesive energy. *Phy. Rev. B*, 58:5989 – 5995, 1998.
- [140] A. Van der and Ven G. Ceder. *The Role of Electronic Properties in the Electrochemical Behavior of Intercalation Compounds from a First Principle Vantage Point*, pages 42–80. Kluwer Academic Publishers, Massachusetts, 2004.
- [141] O. Le Bacq, A. Pasturel, and O. Bengone. Impact on electronic correlations on the structural stability, magnetism, and voltage of  $\text{LiCoPO}_4$  battery. *Phys. Rev. B*, 69:245107, 200.
- [142] Karsten Tillmann and Wolfgang Jäger. Quantitative hrtem analysis of semiconductor quantum dots. *Journal of Electron Microscopy*, page 245, 2000.
- [143] E. Guerrero, P. Galindo, T. Ben A. Yanez, and S. I. Molina. Error quantification in strain mapping methods. *Microsc. Microanal.*, page 320, 2007.



# Acknowledgments

I would like to thank Prof. Ute Kaiser for giving me the chance to work on this topic. I wish to thank Dr Margret Wohlfart-Mehrens, and Dr Peter Axmann who have guided me in the vast and complex field of lithium ion battery materials. Special thanks also go to Dr Andrey Chuvilin who taught me a lot in electron microscopy.

I also want to thank Dr Florent Boucher and Dr. Phillippe Moreau for giving me a chance to stay at the Institute for Materials, University of Nantes. Special thanks and appreciations go to Dr. Boucher for his patience and guidance in the field of electronic structure calculations.

I would also like to thank my colleagues Oliver, Ute, Phillip, Jens, Zhongbo, Gerardo, Jannik, Johannes, and Simon at of the Electron Microscopy group of material science for a great working atmosphere. In particular, I would like to thank Sören Selve and Sabine Grözinger for their help with the sample preparation, Brigitte Kast for her help with all administrative issues and Hans Wiringer for his help with the computers.

I cannot forget Dr. Bernd Heisse and Frau Monika Pahwa for their support during my studies in Ulm.

I also recognize that this research would not have been possible without the financial support from the German Federal Ministry of Education and Research (Bundesministerium für Forschung und Bildung, BMBF) and German Research Foundation (Deutsche Forschungsgemeinschaft, DFG) and I express my thanks for it.

My parents, brother and sisters deserve special thanks for their unwavering moral and spiritual support. I especially would like to thank my Father for showing me that nothing is impossible. You are an inspiration to me this thesis is dedicated to you. I am also grateful for the special lady in my life, my wife, my Mushu. I thank her for her love and support during the good and hard times.



# Publications and Conference proceedings

## Journal articles

1. M. K. Kinyanjui, A. Chuvilin, P. Axmann, M. Wohlfahrt-Mehrens, P. Moreau, F. Boucher, U. Kaiser, *Origin of valence and core excitations in  $\text{LiFePO}_4$  and  $\text{FePO}_4$* , Journal of Physics: Condensed Matter, 22 (2010) 275501

## Conference proceedings

### Oral presentation

1. M. K. Kinyanjui, A. Chuvilin, P. Axmann, M. Wohlfahrt-Mehrens, P. Moreau, F. Boucher, U. Kaiser. *Valence and core excitations in  $\text{Li}_{(1-x)}\text{FePO}_4$* . DPG Frühjahrstagung, Regensburg, Germany. 24.03.2010
2. M. Kinyanjui, A. Chuvilin, U. Kaiser, S. Stroebele, P. Axmann, C. Stinner, M. Wohlfahrt-Mehrens. *Energy Filtered and High Resolution TEM investigation of Electrochemically Delithiated  $\text{LiFePO}_4$* . Conference talk, Euroconference on Science and Technology of Ionics, September 9-15, 2007 Batz-sur-Mer, France.

### Poster presentations

1. M. Kinyanjui, A. Chuvilin, U. Kaiser, P. Axmann, M. Wohlfahrt-Mehrens. *Investigating Charge compensation in  $\text{LiFePO}_4$* . Poster presentation at 9th Multinational Conference on Microscopy 2009, Graz, Austria, 20 Aug-4 Sept 2009.
2. M. Kinyanjui, U. Kaiser, M. Wohlfahrt-Mehrens, J. Li, D. Vainkin. *Low loss Electron Energy Spectroscopy on  $\text{LiFePO}_4$  for Lithium ion battery Applications*. Poster presentation at 14th European Microscopy Conference, Aachen, Germany, 1-5 Sept 2008.
3. M. Kinyanjui, U. Kaiser, M. Wohlfahrt-Mehrens, J. Li, D. Vainkin. *Domain formation in delithiated  $\text{LiFePO}_4$ ; A cathode material for Lithium ion batteries*. Poster presentation at 14th European Microscopy Conference, Aachen, Germany, 1-5 Sept 2008.

4. M. Kinyanjui, A. Chuvilin, U. Kaiser, S. Mohanan, U. Herr. *Investigating the oxide barrier layer in TaCoCuCo/oxide/CoNiMn Spin valves structures*. Poster presentation Microscopy conference, Saarbrücken, Germany.
5. A. Gupta, S. Mohanan, U. Herr, M. Kinyanjui, Z. Zhang, U. Kaiser. *Influence of nano-oxide layer on magnetotransport properties of NiMn based giant magnetoresistive sensors*. 3rd Seeheim Conference on Magnetism, Frankfurt, Germany, Aug. 26 – 30, 2007.

# Curriculum vitae

## Michael Kiarie Kinyanjui

Date of Birth: 18/5/1977

Place of Birth: Karuri, Kenya

Nationality: Kenyan

### EDUCATION

**Ph.d Studies**, Mar. 2006 - Aug. 2009

University of Ulm, Ulm, Germany

**Doctoral research:**

Electronic and structural properties of Lithium Iron Phosphate(dissertation work).

**M.Sc. in Advanced Materials Science**, Sept. 2004- Mar. 2006

University of Ulm, Ulm, Germany

**B.Sc.** May 1996 - Jul.2000

University of Eastern Africa, Baraton, Kenya

**High School 1991 - 1994**

Muhoho boys High School, Gatundu, Kenya

**Primary School**, 1983-1990

Karuri Primary School, Karuri, Kenya

